

# NOTE TO USERS

This reproduction is the best copy available.

**UMI**<sup>®</sup>



# **Feasibility Study and Design of an Actively Controlled Tip for Helicopter Rotor Blades**

by

**Matthew Yong-Jin Cha**

B.Eng

A thesis submitted to  
the Faculty of Graduate Studies and Research  
in partial fulfillment of  
the requirements for the degree of  
Master of Applied Science

*Ottawa-Carleton Institute*

*For Mechanical and Aerospace Engineering*

Department of Mechanical and Aerospace Engineering  
Carleton University  
Ottawa, Ontario  
August 2007

© Copyright

Matthew Yong-Jin Cha

2007



Library and  
Archives Canada

Bibliothèque et  
Archives Canada

Published Heritage  
Branch

Direction du  
Patrimoine de l'édition

395 Wellington Street  
Ottawa ON K1A 0N4  
Canada

395, rue Wellington  
Ottawa ON K1A 0N4  
Canada

*Your file* *Votre référence*

*ISBN: 978-0-494-36818-3*

*Our file* *Notre référence*

*ISBN: 978-0-494-36818-3*

#### NOTICE:

The author has granted a non-exclusive license allowing Library and Archives Canada to reproduce, publish, archive, preserve, conserve, communicate to the public by telecommunication or on the Internet, loan, distribute and sell theses worldwide, for commercial or non-commercial purposes, in microform, paper, electronic and/or any other formats.

The author retains copyright ownership and moral rights in this thesis. Neither the thesis nor substantial extracts from it may be printed or otherwise reproduced without the author's permission.

#### AVIS:

L'auteur a accordé une licence non exclusive permettant à la Bibliothèque et Archives Canada de reproduire, publier, archiver, sauvegarder, conserver, transmettre au public par télécommunication ou par l'Internet, prêter, distribuer et vendre des thèses partout dans le monde, à des fins commerciales ou autres, sur support microforme, papier, électronique et/ou autres formats.

L'auteur conserve la propriété du droit d'auteur et des droits moraux qui protègent cette thèse. Ni la thèse ni des extraits substantiels de celle-ci ne doivent être imprimés ou autrement reproduits sans son autorisation.

---

In compliance with the Canadian Privacy Act some supporting forms may have been removed from this thesis.

Conformément à la loi canadienne sur la protection de la vie privée, quelques formulaires secondaires ont été enlevés de cette thèse.

While these forms may be included in the document page count, their removal does not represent any loss of content from the thesis.

Bien que ces formulaires aient inclus dans la pagination, il n'y aura aucun contenu manquant.

  
**Canada**

The undersigned recommend to  
the Faculty of Graduate Studies and Research  
acceptance of the thesis

**Feasibility Study and Design of an Actively Controlled Tip  
for Helicopter Rotor Blades**

submitted by

**Matthew Yong-Jin Cha**

B.Eng

in partial fulfillment of the requirements for  
the degree of Master of Applied Science

---

&

Thesis Supervisors

---

Chair, Department of Mechanical and Aerospace Engineering

Carleton University

August 2007

## **ABSTRACT**

The Actively Controlled Tip (ACT) is a mechanism which is designed to displace the blade tip vortex and by this, to reduce rotor Blade Vortex Interaction (BVI) noise. In order to achieve this objective, the centrifugal loads and the aerodynamic loads are numerically calculated and designed reversely to find the compulsory torque needed to deflect the blade tip from zero degree to 20 degrees. The novelty of the ACT is the counter-weight concept using a screw-jack mechanism. The key idea of the counter-weight concept is to allow the blade tip to rotate freely without any load from zero degree to 10 degrees, beyond which point, the actuator power will help to complete the blade tip motion down to 20 degrees. The ACT demonstrator was fabricated and tested on the whirl tower in DLR (German Aerospace Centre). The ACT demonstrator was successfully tested and it deflected full 20 degrees in about one minute at 400 RPM but it failed at 700 RPM. An extensive analysis of the cause of the ACT failure is presented and recommendations are given to improve the design. Furthermore, the self-locking system was designed in order to test the feasibility of having the ACT on the rotor blade tip.

## ACKNOWLEDGEMENT

I would like to thank for those who supported, inspired, guided, helped and encouraged me during past two years of my Master's degree.

I am very grateful to study and research under two co-supervisors, Professor Daniel Feszty and Professor Fred Nitzsche for their financial support and endless guidance for past two years. Professor Feszty has been more than a professor; like a close friend. When I am having a hard time understanding rotorcraft dynamics, he has showed, helped, and explained kindly what and how rotorcraft worked. Thankful to him, now my rotorcraft knowledge is an intermediate. Professor Nitzsche has been pushing me to not slack off during my two years. Even though he did not personally tell me that I was not doing so well, his presence during the SHARCS meeting had been a wakeup call for me.

I would also like to thank my colleagues in the SHARCS research group. I have been working very closely with them for past two years and it had been an awesome experience just knowing them and working with them. I would like to express special thanks to Brian Lynch for working together to develop new ideas and for his inspiration, Andrei Mander for his help on finding motor characteristic experiment, and Greg Oxely for Smartrotor tutorials and providing me with SHARCS simulation data. Furthermore, I would like to thank machinists at Science & Technology Centre in Carleton for their expertise and guidance on machining and fabricating the Actively Controlled Tip.

Finally, I would like to express my thanks to my parents. They have showed and taught me endless love and believing in me when I wanted to let go of everything and felt that I was not a Master material. I also would like to thank Peter and Kelly for praying for me and for their love and support. Thank you all.

# TABLE OF CONTENTS

Abstract.....	i
Acknowledgement.....	ii
Table of Contents.....	iii
List of Figures.....	v
List of Tables.....	viii
<b>1. Introduction.....</b>	<b>1</b>
1.1 Vibration and Noise on Helicopters.....	1
1.1.1 Effects of Vibration.....	2
1.1.2 Effects of Noise.....	3
1.1.3 The Coupling of Vibration and Noise.....	4
1.2 Types of Noise.....	5
1.2.1 Rotor Blade Slap.....	7
1.2.2 Blade-Vortex Interaction Noise.....	9
1.2.3 Rotational Noise.....	11
1.2.4 Thickness Noise.....	12
1.2.5 Tail Rotor Noise.....	13
1.3 Noise Reduction Methods.....	14
1.3.1 Five Bladed Rotors.....	15
1.3.2 Blade Tip Shape Optimization.....	16
1.3.3 Airfoil Thickness Reduction.....	19
1.3.4 Quiet Tail Rotor Design.....	19
1.3.5 Actively Controlled Systems.....	21
1.4 The SHARCS Concept.....	23
1.5 Research Objectives.....	25
<b>2. Actively Controlled Tip Design.....</b>	<b>27</b>
2.1 Operational Conditions.....	27
2.1.1 Scaling Factors and Similarity Parameters.....	28
2.1.2 Scaling Factors.....	29
2.1.3 Similarity Parameters.....	30
2.1.4 Actuation Requirements.....	32
2.2 Loads Acting on ACT.....	33
2.2.1 Centrifugal Loads.....	33
2.2.2 Aerodynamic Loads.....	35
2.2.3 Resultant Loads.....	42
2.3 Design Concept.....	43
2.3.1 Design Requirements of the ACT.....	44

2.3.2	Actuator Concept.....	46
2.3.3	The Counter-Weight Concept.....	47
2.3.4	Screw-Jack Mechanism.....	48
2.4	Scaled Model Design.....	49
2.4.1	The Counter-Weight Sizing.....	50
2.4.2	Motor Requirements.....	55
2.4.3	Motor Selection.....	59
2.4.4	Overall Assembly.....	63
2.4.5	Manual Setup Version.....	65
2.5	Full-Scale Feasibility Study.....	69
2.5.1	The Counter-Weight Sizing.....	70
2.5.2	Motor Requirements.....	73
2.5.3	Motor Selection.....	75
2.5.4	Overall Assembly.....	77
<b>3.</b>	<b>Position Accuracy Control.....</b>	<b>79</b>
3.1	System Equations of Electric Motor.....	79
3.1.1	MatLAB Simulation of Motor Position.....	83
3.1.2	Electric Motor Controller.....	85
3.2	System Equations of Gearhead Mechanism.....	91
3.3	System Equations of ACT.....	93
3.4	MatLAB Simulation of the Position Control.....	94
3.5	Torque Rod Angle of Twist.....	102
<b>4.</b>	<b>Whirl Tower Testing.....</b>	<b>105</b>
4.1	Rationale.....	105
4.2	Test Model.....	107
4.2.1	The Counter-Weight Sizing.....	107
4.2.2	Motor Characteristics.....	110
4.2.3	Overall Assembly.....	115
4.3	Results.....	119
4.4	Failure Analysis.....	121
4.5	Static Test of ACT.....	124
4.6	Recommendations.....	129
<b>5.</b>	<b>Conclusions and Recommendations.....</b>	<b>133</b>
	References.....	136
	Appendixes.....	142

## LIST OF FIGURES

Figure 1: Aeroacoustic noise sources for a rotorcraft.....	5
Figure 2: Sound pressure level spectrum of the rotational noise sources for a rotorcraft.....	6
Figure 3: Definition of the rotor disk plane coordinate axes and the observer position .....	8
Figure 4: Creation of the blade vortex interaction noise.....	10
Figure 5: Eurocopter EC-155 featuring a five-bladed rotor.....	16
Figure 6: Advanced blade tip designs featured on a) AgustaWestland EH-101, with the BERP blade tip, and b)NH Industry NH-90 with swept, tapered, and anhedral blade tip.....	17
Figure 7: Mitsubishi heavy industries SH-60K.....	18
Figure 8: Fenestron tail rotor on Eurocopter EC 135 helicopter.....	20
Figure 9: NOTAR on MD600N helicopter.....	21
Figure 10: CIRA's smart rotor system.....	22
Figure 11: The SHARCS hybrid concept with three individual feedback systems....	24
Figure 12: SHARCS rotor twist distribution, relative to the twist angle at 75% radius.....	30
Figure 13: Schematic diagram of the blade tip and its CG location.....	34
Figure 14: Distribution of flow field: a) hovering flight, b) forward flight.....	36
Figure 15: Discretized blade element.....	37
Figure 16: Flow chart of the BEMT calculations.....	40
Figure 17: Aerodynamic load distribution for SHARCS.....	41
Figure 18: Effective angle of attack for various thrust coefficients.....	42
Figure 19: Schematic diagram of total hinge moment from both aerodynamic and centrifugal load.....	42
Figure 20: Hinge moment with/without counter-weight for centrifugal load.....	48
Figure 21: Schematic diagram of counter-weight concept.....	48
Figure 22: Location of ACT and its actuator in SHARCS blade.....	49
Figure 23: ACT's components part name.....	50
Figure 24: ACT's components centre of gravity location.....	51
Figure 25: Free body diagram for the actuator mechanism components.....	52
Figure 26: Resultant acting on the screw-jack mechanism.....	55

Figure 27: Schematic diagram of power screw.....	56
Figure 28: Schematic diagram of typical thrust collar.....	57
Figure 29: Required motor torque variation with deflection angle.....	58
Figure 30: SHARCS scaled blade with ACT actuator in perpendicular direction.....	63
Figure 31: Close up view of the root transition.....	64
Figure 32: Location of self-lock mechanism's components.....	66
Figure 33: Pivot component's geometry.....	66
Figure 34: Force required to deflect the blade tip.....	69
Figure 35: Full scale blade tip sketch.....	71
Figure 36: Aerodynamic loads distribution for full-scale study.....	72
Figure 37: Effective angle of attack for full-scale study.....	72
Figure 38: Torque versus angle of deflection for full-scale ACT.....	75
Figure 39: Electric circuit diagram of electric motor.....	79
Figure 40: Block diagram of electric motor.....	82
Figure 41: Step response of electric motor for open-loop system.....	84
Figure 42: Motor response to a step input of $K_p = 1.5$ for closed-loop system.....	85
Figure 43: Motor response to a step disturbance of $K_p = 1.5$ for closed-loop system .....	86
Figure 44: Motor response to a step input of $K_p = 1.5$ and $K_I = 13$ for closed-loop system.....	87
Figure 45: Motor response to a step disturbance of $K_p = 1.5$ and $K_I = 13$ for closed -loop system.....	87
Figure 46: Closed-loop response of step input with $K_p = 15$ and $K_I = 130$ .....	88
Figure 47: Closed-loop response of step disturbance with $K_p = 15$ and $K_I = 130$ .....	88
Figure 48: Closed-loop response of step input with $K_p = 15$ , $K_I = 130$ and $K_d = 0.1$ .....	89
Figure 49: Closed-loop response of step disturbance with $K_p = 15$ , $K_I = 130$ and $K_d = 0.1$ .....	89
Figure 50: Closed-loop response of step input with $K_p = 15$ , $K_I = 200$ and $K_d = 0.25$ .....	90
Figure 51: Closed-loop response of step disturbance with $K_p = 15$ , $K_I = 200$ and $K_d = 0.25$ .....	91

Figure 52: Schematic diagram of the gearhead.....	92
Figure 53: Schematic diagram of motor with a gearhead.....	92
Figure 54: Step response of electric motor and gearhead for open-loop system.....	95
Figure 55: Closed-loop response of step input with $K_p = 2,000$ .....	96
Figure 56: Closed-loop response of step disturbance with $K_p = 2,000$ .....	96
Figure 57: Closed-loop response of step input with $K_p = 2,000$ and $K_I = 1,000$ .....	97
Figure 58: Closed-loop response of step disturbance with $K_p = 2,000$ and $K_I = 1,000$ .....	98
Figure 59: Closed-loop response of step input with $K_p = 20,000$ and $K_I = 1,000$ .....	98
Figure 60: Closed-loop response of step disturbance with $K_p = 20,000$ and $K_I = 1,000$ .....	99
Figure 61: Closed-loop response of step input with $K_p = 20,000$ , $K_I = 1,000$ and $K_d = 300$ .....	100
Figure 62: Closed-loop response of step disturbance with $K_p = 20,000$ , $K_I = 1,000$ and $K_d = 300$ .....	100
Figure 63: Closed-loop response of step input with $K_p = 80,000$ , $K_I = 900,000$ and $K_d = 900$ .....	101
Figure 64: Closed-loop response of step disturbance with $K_p = 80,000$ , $K_I = 900,000$ , and $K_d = 900$ .....	101
Figure 65: Schematic diagram of DLR's whirl tower test rig.....	106
Figure 66: Resultant torque required to deflect the blade tip for whirl tower test....	110
Figure 67: Motor with aluminum pulley.....	111
Figure 68: Experimental set up to measure the motor torque.....	112
Figure 69: Relationship of motor speeds required to lift different loads at different voltages.....	114
Figure 70: Relationship of current required to lift different loads at different voltages .....	114
Figure 71: Hall effect transducer sensor locations on the blade tip.....	116
Figure 72: Hall effect transducer sensor locations on the gearhead shaft.....	116
Figure 73: Prototype Active Controlled Tip design.....	117
Figure 74: Aluminum welds on ACT whirl tower prototype.....	118
Figure 75: ACT on DLR's whirl tower test rig.....	119
Figure 76: Wireless transmitter for the whirl tower test rig.....	120

Figure 77: Off-position of counter-weight on ball screw.....	121
Figure 78: Graupner's gearhead.....	122
Figure 79: Static test set up.....	124
Figure 80: Location of moment arm for ACT prototype.....	125
Figure 81: Static test at 20 degree deflection as hanging mass increases.....	127
Figure 82: Brass bushing inside the horseshoe.....	128
Figure 83: Bent steel plate cover.....	128
Figure 84: Bent brass bushing.....	129
Figure 85: New motor and gearhead arrangement.....	131

## LIST OF TABLES

Table 1: BO-105 rotor parameters.....	28
Table 2: Rotor geometry parameters.....	29
Table 3: Natural frequencies of mode shape for SHARCS.....	31
Table 4: Variation of the ACT component's CG with blade tip deflection.....	52
Table 5: Centrifugal and reaction forces on anedral and tip .....	54
Table 6: Centrifugal and reaction forces on link and counter-weight .....	54
Table 7: Torque required for ACT to overcome resultant loads.....	58
Table 8: Summary of the actuator motor search; a)DC motor, b)stepper motor, c) hydraulic actuator, and linear actuator.....	60
Table 9: Maxon RE 30 DC motor additional characteristics .....	62
Table 10: Maxon GP 32C gearhead additional characteristics.....	63
Table 11: Final mass of ACT components.....	65
Table 12: Variation of the ACT manual setup version components' CG with blade tip deflection.....	67
Table 13: Centrifugal and reaction forces on ACT manual setup version on anedral and tip .....	68
Table 14: Centrifugal and reaction forces on ACT manual setup version on link and counter-weight .....	68
Table 15: BO-105 rotor blade characteristics for the SHARCS full scale study.....	70
Table 16: Centrifugal and reaction forces on full scale ACT on anedral and tip.....	73
Table 17: Centrifugal and reaction forces on full scale ACT on link and counter- weight.....	74
Table 18: Torque required for the full ACT to overcome resultant loads.....	74
Table 19: Maxon RE 75 DC motor additional characteristics.....	76
Table 20: Maxon GP 81 gearhead additional characteristics.....	76
Table 21: Final mass of full-scaled ACT system.....	77
Table 22: Comparison between full-scaled and small-scale ACT system.....	78
Table 23: Variation of the whirl tower test components' CG with blade tip deflection .....	108
Table 24: Centrifugal and reaction forces on whirl tower testing component on anedral and tip.....	108

Table 25: Centrifugal and reaction forces on whirl tower testing component on link and counter-weight.....	109
Table 26: Torque required for ACT to overcome centrifugal acceleration.....	109
Table 27: Characteristics of Graupner 33G 6V motor.....	111
Table 28: Motor speed and current at different loads on the motor.....	113
Table 29: Acceleration and gravity forces at different RPM for a mass of 1 gram .....	130

# **1. INTRODUCTION**

The present chapter describes how vibration and noise are generated on helicopters, the various types and sources of, as well as the solutions used to reduce the acoustic footprint of helicopters. It will be shown that reducing noise typically leads to the increase of vibration and vice versa and that very little research has been done on reducing both phenomena simultaneously (Feszty, 2007). This will lead to the motivation behind the new control concept called SHARCS - Smart Hybrid Active Rotor Control System, which aims to reduce vibration and noise simultaneously and of which this research work is an integral part of.

## **1.1 Vibration and Noise on Helicopters**

Helicopters are unique because of their vertical take-off and landing capability and serve as invaluable resource for a wide range of civil and military missions such as air ambulance, search and rescue, fire fighting, police surveillance, oil rig transport, logging, etc. Although helicopters are widely used, the understanding of the aerodynamic phenomena arising over the rotor and the technologies to improve the helicopter ride quality are not as mature as for fixed-wing aircraft (Johnson, 1980). A major complexity of helicopters is the associated excessive vibration and noise, which have received

increased attention in the recent years throughout the industry (Leishman, 2000). Vibration and noise limits the efficiency of the helicopter, deteriorates the ride quality, creates excessive noise pollution to both passengers and the environment, as well as increases the operational costs via increased maintenance requirements (Johnson, 1980).

### **1.1.1 Effects of Vibration**

Vibration is the major source of fatigue on helicopters, which increases maintenance costs, and decreases the aircraft life cycle (Hawkyard, 1999). It also has implications on health monitoring since if fatigue is not detected early, fractures could lead to serious flight accidents (Liguore, 1995). Another effect of vibration is the poor ride quality which is uncomfortable for passengers and endangers the health of the pilot. It has been shown that pilots exposed to vibrations for longer periods could develop serious spinal injury (Reichert, 1981). This is especially critical for military helicopter pilots who are usually flying more hours than their civil counterparts. Other impacts on health include fatigue on tendons, increased heart rate and blood pressure depending on a person, numbness, and teeth chatter (Reichert, 1981). Vibration has a major effect on the helicopter performance too since it limits the maximum forward flight speed by developing excessive loads in the pitch links (Anderson, 1997). Thus, unlike for fixed-

wing aircraft, the maximum flight speed of a helicopter is limited not by the maximum thrust (power) provided by the propulsion unit but by the occurrence of excessive vibration as a result of the rotary-wing aerodynamics. Finally, minimizing vibration is vital for military applications since vibration could limit the weapon pointing accuracy, which is not desirable in combat situations (Khanh, 1994).

### **1.1.2 Effects of Noise**

Beside vibration, noise is another major concern of helicopter operators. Due to the loud noise that helicopters produce, the usage of helicopters over congested areas is not welcomed (Silver, 1996). Since there are no altitude limits set for helicopters, some groups are protesting for establishing a minimum altitude of one thousand feet over congested areas for helicopters (Silver, 1996). By this, helicopter noise could be spread more towards the sky and less directly under the helicopter operating areas. For military operations, the stealth capability could be improved by reducing noise.

Furthermore, reducing noise from helicopters is important for pilot and passenger health and comfort. It is important for helicopter pilots to hear radio communication correctly during flight. To enable this, pilots often increase the speech levels in the headset to compensate for the high noise levels caused by the helicopter (Johansson,

1997). This can lead to hearing damage and in the long term, even for the loss of hearing (Johansson, 1997). Finally, one major obstacle to introducing vertical takeoff and landing (VTOL) aircraft on short-haul regional routes is the lack of “jet-smooth ride” in comparison to fixed-wing aircraft.

### **1.1.3 The Coupling of Vibration and Noise**

The occurrence of vibration and noise is interconnected on helicopters. Many researchers have shown that these two phenomena cannot be reduced at the same time (Feszty, 2007). This is likely due to the phenomenon called blade-vortex interaction (BVI) which is the source of both vibration and noise (Feszty, 2007). There have been many attempts trying to reduce only the vibration using active methods such as active twist control (Shin, 2002) or active flap control (Straub, 2004), but usually at the expense of noise. This individual reduction of vibration and/or noise is one of the most active research areas in the field of helicopters nowadays. The most active research groups include those at Eurocopter (Kloppel, 2000), the University of Michigan (Friedmann, 2002), the University of Maryland (Chopra, 2006), and some other too like Georgia Institute of Technology (Ford, 1997), Deutsches Zentrum für Luft- und Raumfahrt e.V. (DLR) in Germany, Office National d’Etude et de Recherche Aérospatiale (ONERA) in

France (Hofinger, 2004), and Centro Italiano Ricerca Aerospaziali S.C.p.A in Italy (CIRA) (Concilio, 2006). AgustaWestland in Italy and Carleton University in Canada are also one of the most active research groups in this field with their research project called SHARCS - Smart Hybrid Active Rotor Control System. The main objective of SHARCS is to design and build a Mach and aeroelastically scaled helicopter rotor for demonstrating the simultaneous reduction of vibration and noise. The unique features of the SHARCS concept is the presence of three actively controlled sub-systems, an Active Pitch Link (APL), an Actively Controlled Flap (ACF), and the Actively Controlled Tip (ACT), whose development is the topic of the present thesis. For a complete overview of the SHARCS design concept (see Feszty, 2007).

## **1.2 Types of Noise**

Excessive noise is an undesired effect, which is inherently associated with helicopter operation. As well, it is the primary form of interaction between the helicopter and a large part of society (Johnson, 1980).

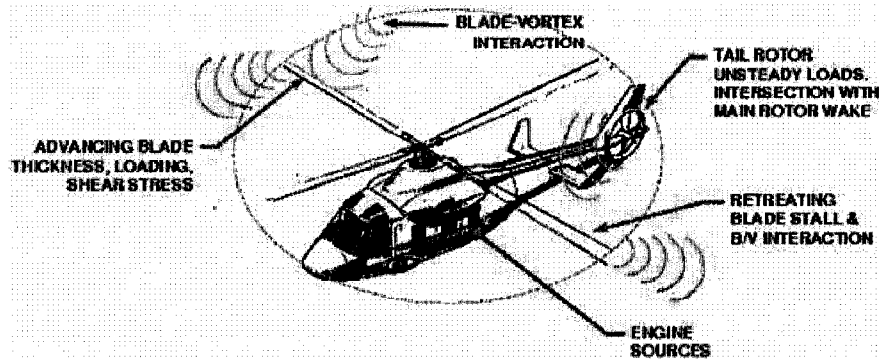


Figure 1: Aeroacoustic noise sources for a rotorcraft (Edwards, 2002).

The noise generated by a helicopter can be distinguished as near-field noise and far-field noise. The near-field noise is produced by the helicopter's internal gearboxes and the engine whereas the far field noise is produced by the main and tail rotors. Figure 1 illustrates the main sources of noise on a helicopter (Johnson, 1980).

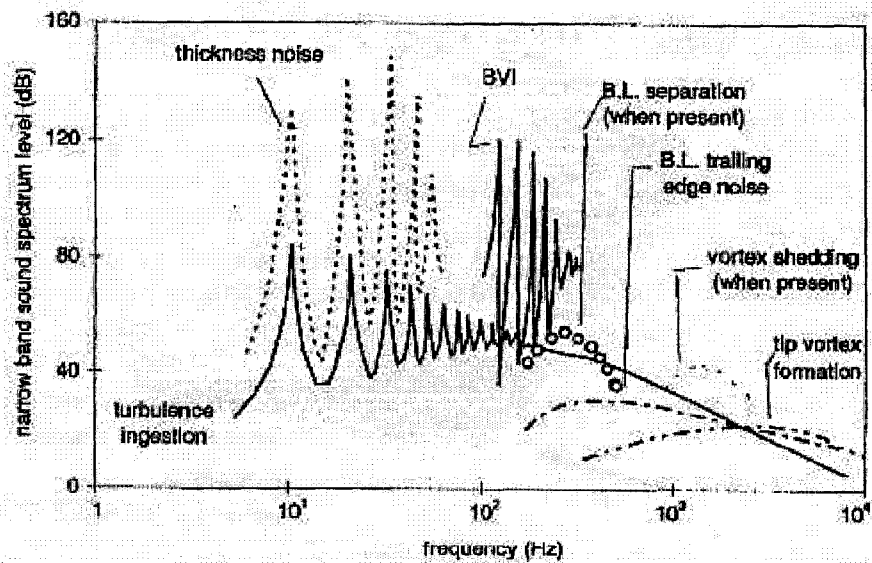


Figure 2: Sound pressure level spectrum of the rotational noise sources for a rotorcraft (Leverton, 1989).

The sound pressure level spectrum versus frequency graph shows where each

noise is occurring during rotorcraft flight (Fig. 2).

There are five different types of noise produced by helicopters and all these add up to one massive single noise. These are rotor blade slap, blade-vortex interaction noise (BVI), rotational noise, thickness noise, and tail rotor noise (Johnson, 1980). Note that it is the Blade-Vortex Interaction (BVI) noise which is one of the most dominant components of the overall helicopter noise. Although the rotor blades produce the most noise, tail rotors also produce the most noticeable and disturbing noise (Johnson, 1980). Each noise type will be examined in detail in the following sections.

### **1.2.1 Rotor Blade Slap**

Rotor Blade slap, an extreme case of rotational noise, is the most dominant far-field noise source on helicopters (Johnson, 1980). Rotor blade slap occurs in every flight regime and so the understanding of blade slap phenomenon is very important for noise reduction (Leverton, 1968). After piston engines have been replaced by quieter turbine engines, the rotor blade slap became even more noticeable during helicopter approach (Leverton, 1968). It covers a range of 20 to 1,000 Hz for the main rotor (Johnson, 1980).

Rotor blade slap is a direct result of BVI and airfoil thickness of the blade flying at high Mach number (Johnson, 1980). As the name explains, rotor blade slap is the

sound of the blade slapping the air, or a sharp crack, banging or slapping sound (Leverton, 1968). Blade slap occurs mostly during maneuvers such as flare to landing, shallow descents, decelerating steep turns, or at high forward speeds (Johnson, 1980).

For calculating the noise from blade slap, the rotor is treated as a thin rigid plate (Lighthill, 1961). The noise generated by blade slap can then be calculated as follows, considering the coordinate system in Figure 3.

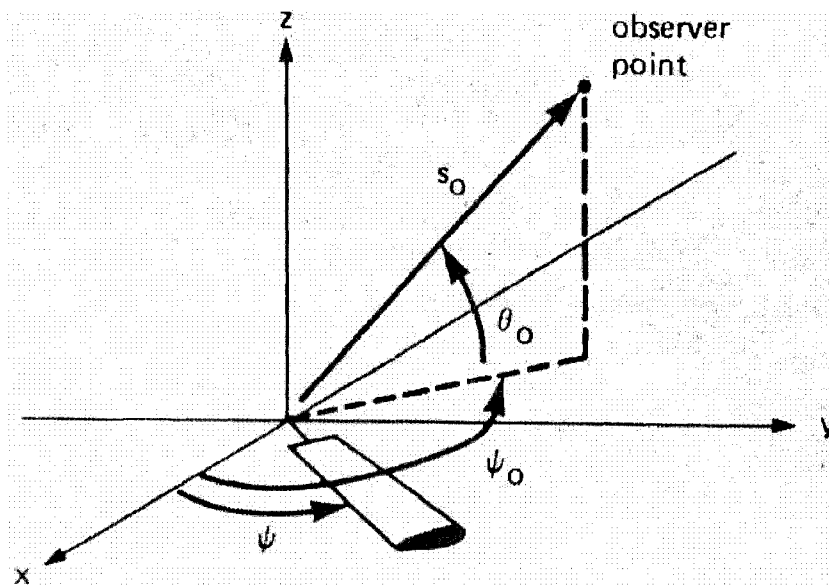


Figure 3: Definition of the rotor disk plane coordinate axes and the observer position (Johnson, 1980).

If  $s_o$  is the distance of an observer from the origin,  $\psi$  is the azimuth angle measuring the position of the blade,  $\psi_o$  is the azimuth angle measuring the position of the observer and  $\theta_o$  is the elevation angle of the observer, then the pressure at a point,

where the position of the observer is relative to the point dipole co-ordinates, where  $i = x, y, z$  (Figure 3) will be,

$$p - p_o = \frac{i}{4\pi s^2} \left[ \frac{1}{c_o} \cdot \frac{\partial F_i}{\partial t} \left( t - \frac{s}{c_o} \right) + \frac{1}{s} \cdot F_i \left( t - \frac{s}{c_o} \right) \right] \quad (1)$$

Here  $F_i$  is the fluctuating force on the blade,  $t$  is the time,  $c_o$  is the speed of sound,  $i$  is the coordinate of any point,  $s$  is the distance of the observation point from the origin, and  $p$  and  $p_o$  are the acoustic pressures. The first term is the far-field noise and the second term is the near-field noise. However, since the rotor blade slap is a far field noise, and if  $s$  becomes infinitely large, the second term of Equation 1 becomes zero, the equation becomes,

$$p - p_o = \frac{i}{4\pi s^2} \cdot \frac{1}{c_o} \cdot \frac{\partial F_i}{\partial t} \left( t - \frac{s}{c_o} \right) \quad (2)$$

Assuming the load is acting as a point dipole, Eq. 2 becomes the following with  $L_s$  being the loading per unit span.

$$p - p_o = \frac{i}{4\pi s^2} \cdot \frac{1}{c_o} \cdot \frac{\partial L_s}{\partial t} \left( t - \frac{s}{c_o} \right) dx \quad (3)$$

Thus, the final equation for the total radiated rotor blade slap noise is,

$$p - p_o = \int_{span} \frac{1}{4\pi s} \cdot \frac{i}{s} \cdot \frac{1}{c_o} \cdot \frac{\partial L_s}{\partial t} \left( t - \frac{s}{c_o} \right) dx \quad (4)$$

### 1.2.2 Blade-Vortex Interaction Noise

Blade vortex interaction (BVI) noise, which is a high frequency sound, is a random sound created as a result of random fluctuations of the forces on the blades (Johnson, 1980). The source of the random fluctuations is the operation of the blade in the turbulent wake of the preceding blades, especially the loads induced by the blade tip vortices (Johnson, 1980). Fig. 4 illustrates how BVI is created in real time.

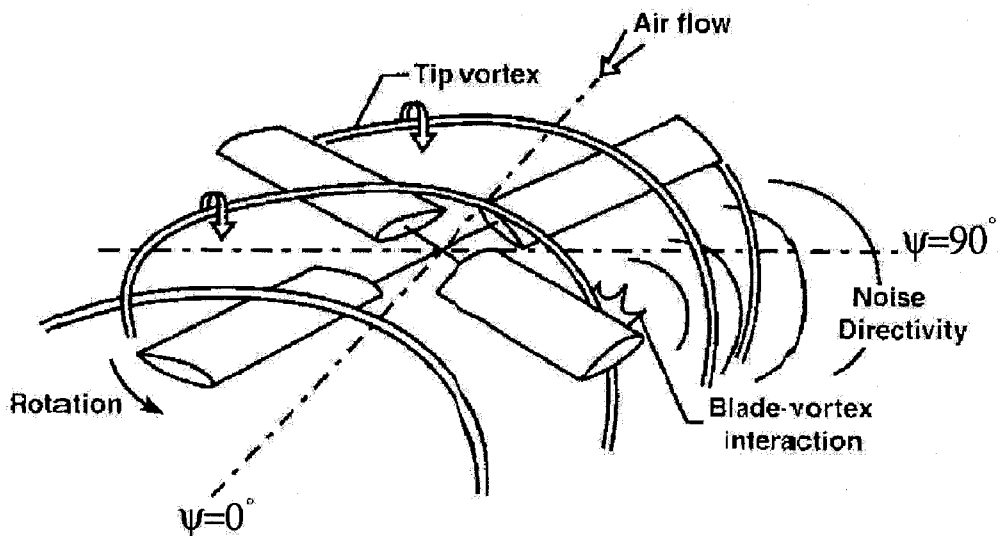


Figure 4: Creation of the blade vortex interaction noise (Brentner, 2003).

As can be seen, BVI can take place on both the main and tail rotor of helicopter, and it can be either of parallel or orthogonal type based on the relative position of the vortex core and blade leading edge (Booth, 1990). Parallel BVI is related with the main rotor, whereas orthogonal BVI to the tail rotor. The main rotor spectrum is about 150 to

1,000 Hz, with a peak around 300 to 400 Hz. The BVI noise is found as to be the following.

$$p^2 = S \cdot \frac{\rho^2}{c_s^2} \cdot \left( \frac{\sin \theta_o}{s_o} \right)^2 \cdot A_b \cdot (\Omega R)^6 \cdot (C_T / \sigma)^2 \quad (5)$$

Here,  $s_o$  is the distance from the rotor hub to the observer,  $\theta_o$  is the angle above the rotor disk plane,  $C_T / \sigma$  is the blade loading,  $\Omega R$  is the tip speed,  $A_b$  is the total blade area,  $c_s$  is the speed of sound,  $\rho$  is the air density, and  $S = \frac{\omega d}{2\pi V}$  is the Strouhal number, where  $d$  is the characteristic dimension of the section, assumed to be constant in Eq. (5) (Johnson, 1980). This equation implies that the rotor vortex noise and also BVI, are proportional to the tip speed to the sixth power.

Since BVI is very complex to predict due to the unsteady loading on the blade, the prediction of this phenomenon is still subject of research nowadays (Johnson, 1980). It has been found that BVI noise is directly proportional to the tip vortex strength and the “miss distance” between the rotor blade and the tip vortex (Morvant, 2004). Several researchers have shown that by controlling these parameters using active control methods, BVI noise could be reduced by up to 7 dB (Jacklin, 1995).

### 1.2.3 Rotational Noise

Rotational noise is another type of far-field noise, which is created by the periodic forces acting on the blade such as lift and drag (Johnson, 1980). These forces are exerted by the blade on the air while the helicopter is operating. Rotational noise is described more like a thumping sound occurring during a helicopter operation. The thumping sound is created when the force acting on the air is unsteady and as the frequency increases, the thump sound sharpens into bangs, eventually becoming a blade slap.

Rotational noise typically ranges from the low frequency non-audible noise to about 150 Hz, which is audible, with the fundamental frequency typically being around 10 to 20 Hz for a main rotor (Johnson, 1980). For propellers or the tail rotor, however, the fundamental frequency is much higher, typically around 100 Hz, which indicates that the rotational noise becomes a dominant noise source for tail rotors (Johnson, 1980). There are many equations regarding forward flight with steady and unsteady loadings but in this Chapter, only the sound pressure for hovering rotors with steady loading equation will be taken into consideration (Johnson, 1980).

$$p = -\frac{1}{4\pi} \left[ \frac{\partial}{\partial x} \frac{F_x(t-s/c_s)}{s} + \frac{\partial}{\partial y} \frac{F_y(t-s/c_s)}{s} + \frac{\partial}{\partial z} \frac{F_z(t-s/c_s)}{s} \right] \quad (6)$$

Here,  $F_x, F_y, F_z$  are the concentrated force components,  $s$  is the distance from the rotor hub to the observer,  $c_s$  is the speed of sound, and  $t$  is the time. Therefore,  $t - s/c_s$  accounts for the finite time,  $s/c_s$  required for a sound wave emitted at the source to travel to the observer.

#### 1.2.4 Thickness Noise

Thickness noise, which is due to the blade thickness depends only on the shape and motion of the blade. It is produced by periodically pushing the air aside (Johnson, 1980). The blade thickness is linearly related to the sound pressure. It produces a normal velocity component on the blade section, first upward and then downward as the blade rotates. For simplicity, the thickness noise equation below is shown before integration (Johnson, 1980).

$$p = \frac{\rho}{2\pi s} \cdot \frac{\partial}{\partial t} \cdot v \cdot (t - s/c_s) dA \quad (7)$$

Here,  $s$  is the distance from the rotor hub to the observer, and again  $t - s/c_s$  is the time which accounts for a sound wave emitted at the source to travel to the observer. Finally,  $v$  is the normal velocity over the disk,  $A$  is the area of the rotor disk,  $t$  is the time,  $c_s$  is the speed of sound, and  $\rho$  is the air density.

### 1.2.5 Tail Rotor Noise

The tail rotor is the source of the most noticeable and disturbing noise next to blade slap (Johnson, 1980). While the main rotor produces a parallel BVI, the tail rotor produces an orthogonal BVI. The tail rotor has same noise mechanisms as the main rotor but it has a higher fundamental frequency, typically around 40 to 120 Hz (Johnson, 1980). Therefore, the tail rotor noise cannot be ignored.

The problem with the tail rotor noise is that in forward flight, the tail rotor is in centre of the main rotor wake and, so it will periodically cut and “chop” the transverse vortex segments (Coton, 2004). The flow around the tail rotor is not only due to the main rotor wake, but it is the sum of the interaction flows produced by the fuselage, rotor hub, engine exhaust and empennage (Yin, 1999). Since measuring or calculating the tail noise is not straightforward, various experimental and numerical techniques were attempted to predict this noise (Coton, 2004). Although proper understanding of orthogonal BVI and the noise generated is still lacking, initial results show that the noise generated is proportional to the axial velocity measured at the main rotor tip vortex core (Coton, 2004).

### **1.3 Noise Reduction Methods**

The most important parameter influencing the noise level of a rotor is the tip speed (Johnson, 1980). Therefore, all of the noise introduced during a helicopter operation can be significantly reduced by lowering the tip speed. However, lowering the tip speed severely compromises the rotor blade aerodynamics.

There are a number of other ways to reduce the noise caused by helicopter rotors. The following list shows the most prominent methods of achieving reduced noise pollution (Johnson, 1980).

1. Increasing the number of main rotor blades to increase the fundamental frequency. Usually, increasing the number of blades on the rotor hub helps to reduce vibration, although some researches show that five blades are also better in terms of noise reduction than four (Clark, 1996).
2. Employing special blade tip planform. Depending on the shape of blade tip, this can alter the tip aerodynamic loads and the structure of the trailing tip vortex.
3. Employing different airfoil thicknesses along the blade. This can reduce the rotational noise and blade slap too. This is because the noise is directly related to the thickness of airfoils and compressibility effects are linked with

high Mach numbers (Johnson, 1980).

4. Employing a quieter tail rotor is a trivial criterion since tail rotor noise is the highest next to blade slap. There are various designs to reduce the tail rotor noise as will be discussed in the next section.

In the following sections, the above noise reduction methods will be discussed in detail.

### **1.3.1 Five Bladed Rotors**

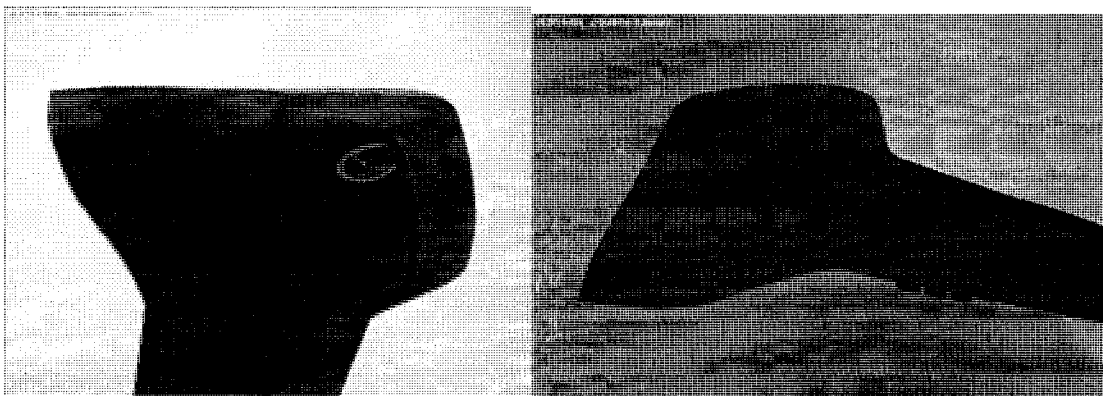
Recently, many manufacturers introduced five bladed rotors, which apparently are optimal for reducing vibration and noise on helicopters (Clark, 1996). A five bladed system is quieter because it distributes the weight of the helicopter across more blades which in turn are related to noise (Eq. 7) (Clark, 1998). This means that the loads on the blades are lower, so they cut through air with a lower pitch angle and the lower angle reduces the noise level (Clark, 1998). Examples of five bladed helicopters include the AgustaWestland EH-101 Kormorant, the Sikorsky S-55 or the Eurocopter EC-155 (Fig. 5).



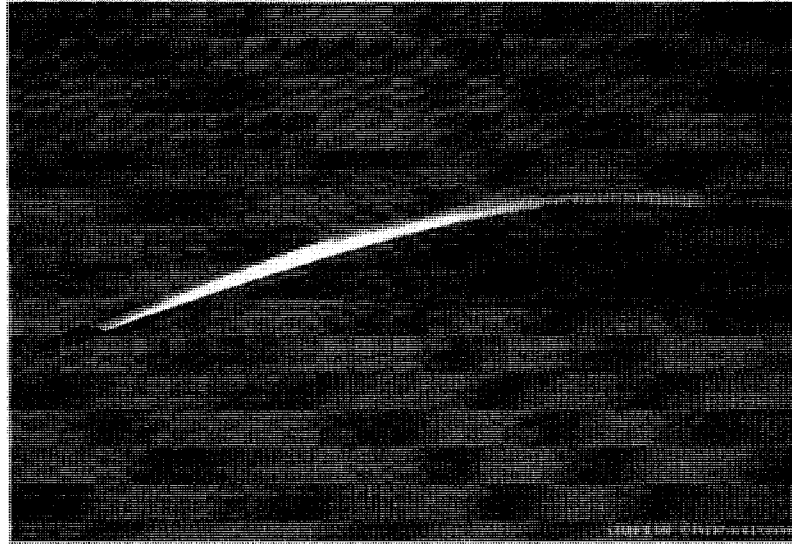
Figure 5: Eurocopter EC-155 featuring a five-bladed rotor  
(American Eurocopter, 2004).

### 1.3.2 Blade Tip Shape Optimization

Advanced blade tip geometries, which include swept tip, tapered tip, anhedral tip, and BERP tip instead of rectangular one, can reduce rotor blade noise significantly (Gandhi, 2000). Fig. 6 shows AgustaWestland's BERP blade tip and NH Industry's (AgustaWestland, Eurocopter, and Stork Fokker) combined blade tip.



a)



b)

Figure 6: Advanced blade tip designs featured on:

a) AgustaWestland EH-101 with BERP blade tip

b) NH Industry NH-90 with swept, tapered, and anhedral blade tip

(Domke, 2004).

The researches show that having a blade tip swept or anhedral resulted in significant reductions in torsional moments and yielded better aerodynamic performance for hover than having a rectangular tip (Weller, 1979). From experiments, it was found that aft sweep of the blade tips decreased oscillatory beamwise and chordwise bending moments on the blade, while anhedral tip increased the beamwise bending moments (Weller, 1979). Also, anhedral blade tip yielded the better aerodynamic performance for hover than rectangular tip (Weller, 1979).

Mitsubishi Heavy Industries designed and built the helicopter SH-60K. SH-60K's main rotor blade has a unique blade tip shape with dihedral and anhedral angle and swept

back angles, which provide excellent aerodynamic characteristics during hovering flight (Takayuki, 2005). Having this unique blade tip design, Mitsubishi was able to increase the maximum gross weight from 21,884 lbs to 24,000 lbs without increasing the rotor diameter (Takayuki, 2005). Fig. 7 depicts the unique blade tip designed by Mitsubishi Heavy Industries.

Besides all these aerodynamic advantages, an anhedral tip appears to favorably affect noise by altering the tip vortex strength, as well as BVI miss distance by “displacing” the main rotor tip vortex.

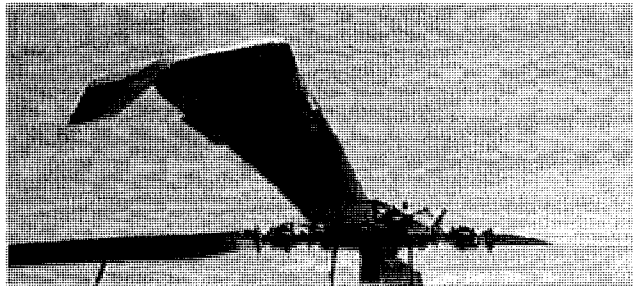


Figure 7: Mitsubishi heavy industries SH-60K (Takayuki, 2005).

Even though having different blade tip geometries are somewhat effective and successful in reducing vibration and noise, the penalty of having a fixed geometry, especially for anhedral tip shape, is severe because it decreases the maximum flight speed by increasing the drag (Weller, 1979). Thus, there have been efforts recently to have a controllable blade tip so that the anhedral angle is only set during certain flight regimes,

such as low speed descent, where BVI noise is most critical. So far, there has been little research completed on why anhedral tip decreases the maximum flight speed. Intensive computational fluid dynamic (CFD) analysis shows that increasing the miss-distance of the BVI is the most effective approach in reducing noise, whereas decreasing the vortex strength is most effective in reducing vibration (Malovrh, 2001).

### **1.3.3 Airfoil Thickness Reduction**

The characteristics of sound radiated from lift is a fundamental aeroacoustics problem (Atassi, 1990). Research has shown that a thicker airfoil produces less noise than a thin airfoil at high Mach numbers (Olsen, 1982). But the problem of having a thick airfoil is that the thicker airfoil will generate more drag.

The airfoil thickness does not have any significant effect on the acoustic pressure at low Mach numbers. But at higher Mach numbers it is found that the airfoil thickness tends to have a direct relationship with the acoustic pressure (Atassi, 1990).

### **1.3.4 Quiet Tail Rotor Design**

The purpose of the tail rotor is to counteract the torque caused by the main rotor and to provide yaw control (Johnson, 1980). In the absence of the tail rotor, a single rotor

helicopter would circle around in the air when it operates. As mentioned earlier, the tail rotor cuts the main rotor tip vortices perpendicularly, generating the characteristic tail rotor BVI noise. However, there are various tail rotor designs to mitigate the orthogonal BVI effect.

One of them, is a design developed by Eurocopter France. It is called the fan-in-fin tail rotor, also known as Fenestron (Fig. 8). The Fenestron tail was first applied on the Eurocopter EC 135 helicopter and is a registered trademark of Eurocopter France (Arnaud, 1996).

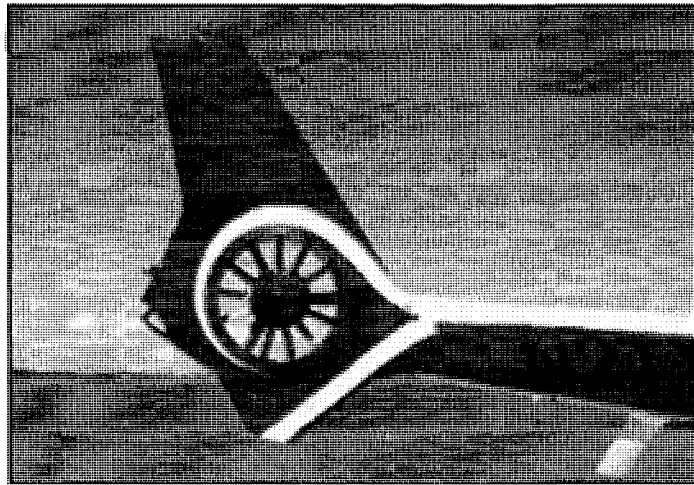


Figure 8: Fenestron tail rotor on Eurocopter EC 135 helicopter (Wiki Books, 2006).

The concept of Fenestron offers maximum performance and acoustic advantages compared to conventional tail rotors (Arnaud, 1996). The performance is increased because the ducted fan can provide the same thrust at as much as 50% of the power

required by conventional tail rotors (Arnaud, 1996). At the same time, the tail rotor noise is reduced by preventing the tail rotor blades to directly interact with the main rotor wake. Also, the ducted fan can spread the noise to a wider angle on the ground (Arnaud, 1996). This new concept of tail rotor has shown to reduce the noise on the EC 135 by more than 4 dB. The noise certification was obtained with a margin of 7 dB for the EC 135T (Arnaud, 1996).

Another tail rotor design to reduce the noise is the NOTAR, which stands for NO-Tail-Rotor, which is a registered trademark of the Boeing Company (Fig. 9) (MD Helicopters, 2006). The NOTAR is a revolutionary anti-torque system with no tail rotors. One of the major advantages of the NOTAR is that it eliminates the operational danger of the tail rotors both in flight and on the ground and also the noise produced by the tail as well (MD Helicopters, 2006).

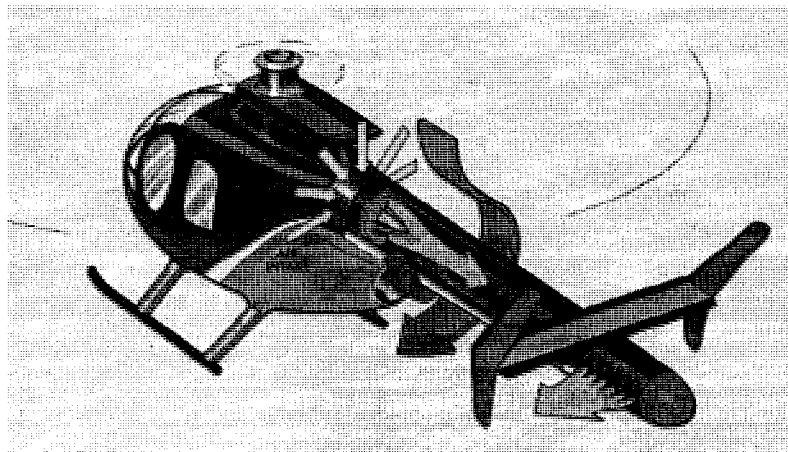


Figure 9: NOTAR on MD600N helicopter (MD Helicopters, 2006).

This NOTAR system makes the MD600N helicopter the quietest helicopter in the world with the noise levels about 50 percent lower than for the competition (MD Helicopters, 2006).

### 1.3.5 Actively Controlled Systems

Active control of the main rotor blades has been pioneered recently by many researchers since this promises to reduce vibration and noise from the helicopters significantly (Straub, 2004). CIRA, the Italian Aerospace Research Centre, has investigated the possibility of active noise control using shape memory alloy (SMA) and magneto-rheological fluid (MRF) device to deflect the blade tip (Testa, 2006).

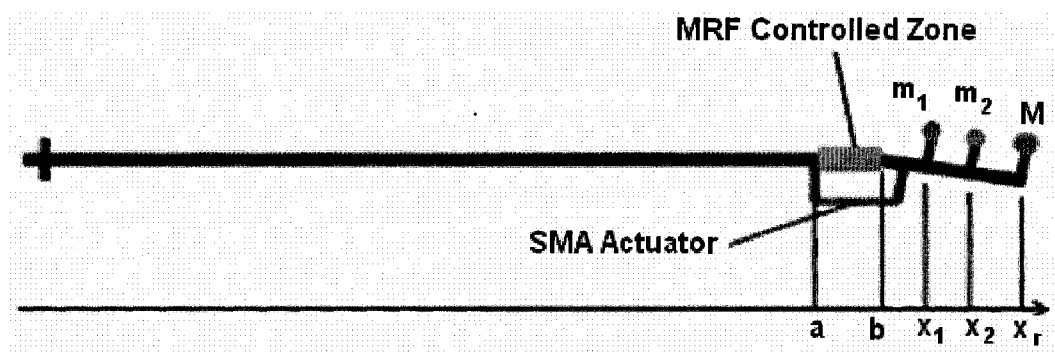


Figure 10: CIRA's smart rotor system.

CIRA has integrated MRF and SMA together to achieve an active control of the blade tip (Fig. 10). The MRF was used to provide a spanwise local control of the bending

stiffness and the SMA was used to bend the structure (Testa, 2006). CIRA took the advantage of having concentrated mass along the blade which helps to deflect the blade tip. But the experiments from CIRA showed that the SMA could not provide enough hinge moment to overcome the aerodynamic and centrifugal loads acting on the blade tip. Similar conclusions were reached by Lynch et al. during a systematic feasibility study of SMA actuated ACT for the SHARCS project (Lynch, 2007).

Despite all these difficulties, there is a major interest in the industry to employ actively controllable anhedral tip on rotor blades. This would be extremely attractive since it would allow to deflect the tip only during the flight regimes where the noise is critical, eg. forward descending flight. Thus, the forward flight speed can be kept high when the ACT is disengaged.

#### **1.4 The SHARCS Concept**

SHARCS is an international project involving a major industrial player, AgustaWestland of Italy, and a number of partner universities. Carleton University is both the leader and the integrator of the SHARCS project. The unique feature of SHARCS is that it aims to reduce vibration and noise simultaneously. For this, three independent feedback systems are used; two flow control techniques to reduce vibration and noise,

and one structural control technique to reduce vibration (Feszty, 2007).

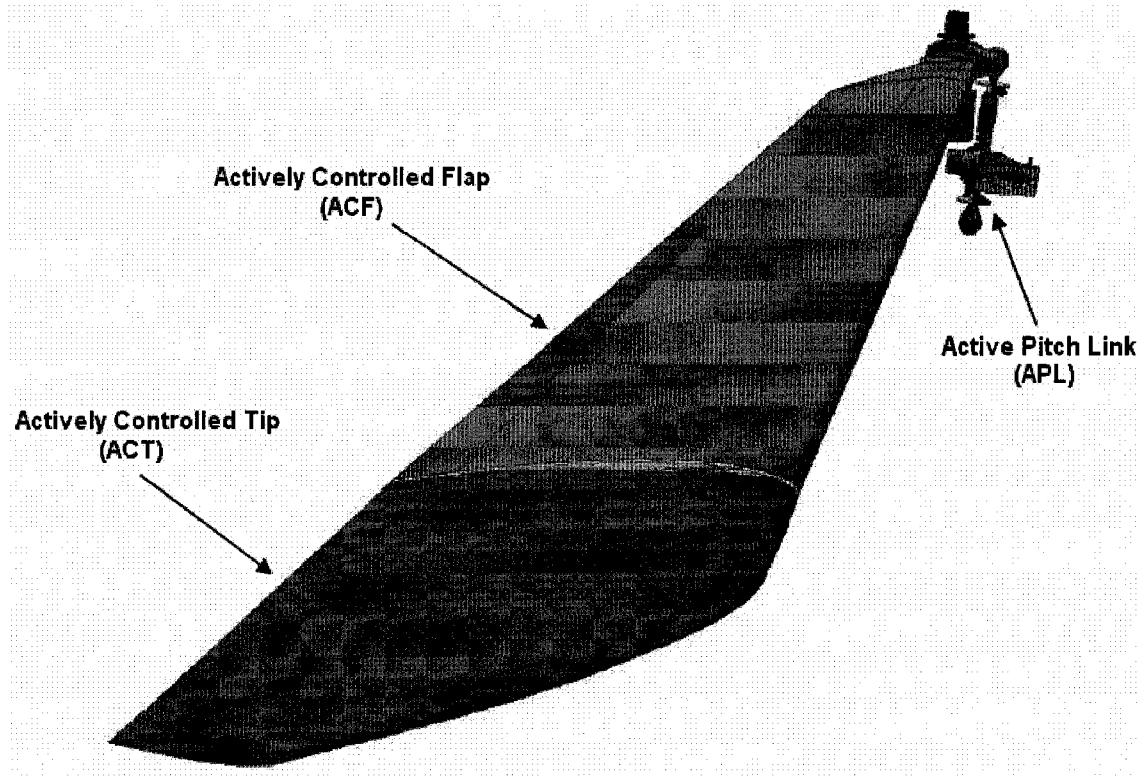


Figure 11: The SHARCS hybrid concept with three individual feedback systems.

A flow control technique includes an Actively Controlled Flap (ACF), and an Actively Controlled Tip (ACT). The ACF is a servo tab, used to twist the blade actively by deflecting the flap, thus reducing vibration and/or noise while the ACT is used to displace the blade tip vortex by creating a blade tip anhedral angle and hence reducing the BVI effect and the associated noise. The structural control involves the Active Pitch Link (APL), which utilizes a smart spring concept to reduce the vibration transmitted to the rotor hub (Lynch, 2007).

Since most noise is generated during forward descent flight, where the helicopter is flying through its own wake (Feszty, 2007), the ACT is an open-loop control system switched on by the pilot when the helicopter is in this flight conditions. When activated, the ACT will displace the tip vortex and alter its strength and structure. The former leads to an increase in the BVI miss-distance, a crucial parameter for BVI noise. However, decreasing the noise, an increase the vibration may be expected, which is then compensated by the ACF and APL systems designed to reduce the vibration. A scaled demonstrator is to be built for SHARCS and tested in AgustaWestland's wind-tunnel in early 2008 in Italy.

## **1.5 Research Objectives**

Although helicopters have been used extensively in aviation in the past five decades, the understanding and control of vibration and noise phenomena characteristic of rotorcraft is still a matter of research. The advancement of new prediction methods, such as Computational Fluid Dynamics (CFD), and novel technologies, such as smart materials, caused an increased activity worldwide to develop actively controlled helicopter rotor blades. However, experiments have indicated that by reducing one phenomenon (vibration), usually leads to the increase of the other (noise) and vice versa.

It is timely and appropriate to develop “smart” rotors with multiple independent control systems to reduce noise and vibration simultaneously. This is the aim of the SHARCS project. The present thesis aims to develop a subsystem for reducing the noise within this concept. More concretely, the research objectives for this thesis are:

- To develop an actively controlled system for reducing BVI noise via an Actively Controlled Tip (ACT) concept
- To identify suitable actuators for full scale and small scale applications
- To design and develop the ACT system in a way so that it fits the scaled SHARCS blade while leaving enough space for the other subsystems, i.e. the Actively Controlled Flap (ACF) and the Active Pitch Link (APL) systems
- To verify the concept via whirl tower tests so that the system will be ready for wind tunnel testing

## **2. ACTIVELY CONTROLLED TIP DESIGN**

In this Chapter, the design of the prototype of an Actively Controlled Tip (ACT) is described. A key feature of the ACT prototype is a counter weight which utilizes the extreme centrifugal load at the blade tip to reduce the actuation power requirement. The ACT system employs a miniature motor at the blade root connected to the ACT system via a torque rod.

The ACT was designed using PRO/ENGINEER Wildfire 2.0 and 3.0. PRO/MECHANICA was used for Finite Element Analysis (FEA) and evaluation of the elastic motion of the various parts. The ACT system was fabricated at the Science Technology Centre of Carleton University.

### **2.1 Operational Conditions**

The SHARCS rotor for wind tunnel testing is a scaled equivalent of a typical helicopter rotor. It is mostly based on the BO-105 rotor, which features the following key parameters (Munsky, 2002):

Table 1: BO-105 rotor parameters

<b>Parameters</b>	<b>Values</b>
Rotor radius	4.91 m
Rotor solidity	0.07
Rotor chord	0.27 m
Airfoil	NACA23012
Twist distribution	-8 degree linear twist
Tip Mach number	0.64

### 2.1.1 Scaling Factors and Similarity Parameters

The requirements for rotor scaling were set by the main industrial partner in the SHARCS project, AgustaWestland. The scaling factors were dictated by the requirement to test the SHARCS rotor in the Politecnico di Milano's 4 m x 4 m, 55 m/s wind-tunnel in Italy, whereas the similarities factors, by the need to reproduce equivalent vibration and noise levels. The choice of the scaling and similarity factors was dictated by the following requirements:

- a) Size: scaled rotor needs to fit into a wind tunnel test section
- b) Geometric similarity: scaled rotor should have similar blade planform, airfoil, rotor solidity, and twist distribution as the full-scale rotor
- c) Aeroacoustic similarity: scaled rotor should have similar noise levels generated as on the full-scale rotor
- d) Aeroelastic similarity: scaled rotor blades should have similar structural response as the full-scale blades

- e) Lock number similarity: scaled rotor blades should have the same ratio of aerodynamic and inertial forces as on the full-scale rotor blades

### 2.1.2 Scaling Factors

The sub-scaled rotor geometry selection has been dictated by the requirement to test the SHARCS rotor in a wind tunnel of 4 m x 4 m test section. Tab. 2 shows the SHARCS rotor geometry parameters.

Table 2: Rotor geometry parameters

Parameters	Values
Number of Blades	4
Rotor Radius	1.096 m
Chord Length	80 mm
Rotor Airfoil	NACA0015
Airfoil Thickness	12 mm
Rotor Solidity	0.093
Tip Speed	162.85 m/s $\approx$ 0.55M at 15 °C
Nominal Frequency	1555 RPM
Percent of Tip Hinge	10%

Initially a NACA23012 airfoil was chosen for the SHARCS rotor blade to match the BO-105 design. However, this airfoil did not provide enough inside space to allow all three sub-systems, ACF, ACT, and APL to be integrated. Hence, the symmetric, NACA0015, a thicker airfoil still with minimum transonic effects, yet maximizing space for the actuators, has been selected for the SHARCS rotor blade

(Ghorashi, 2005). From 90% to 100% radius, the blade gradually tapers off to a NACA0009 airfoil. Fig. 12 illustrates the SHARCS rotor blade twist distribution.

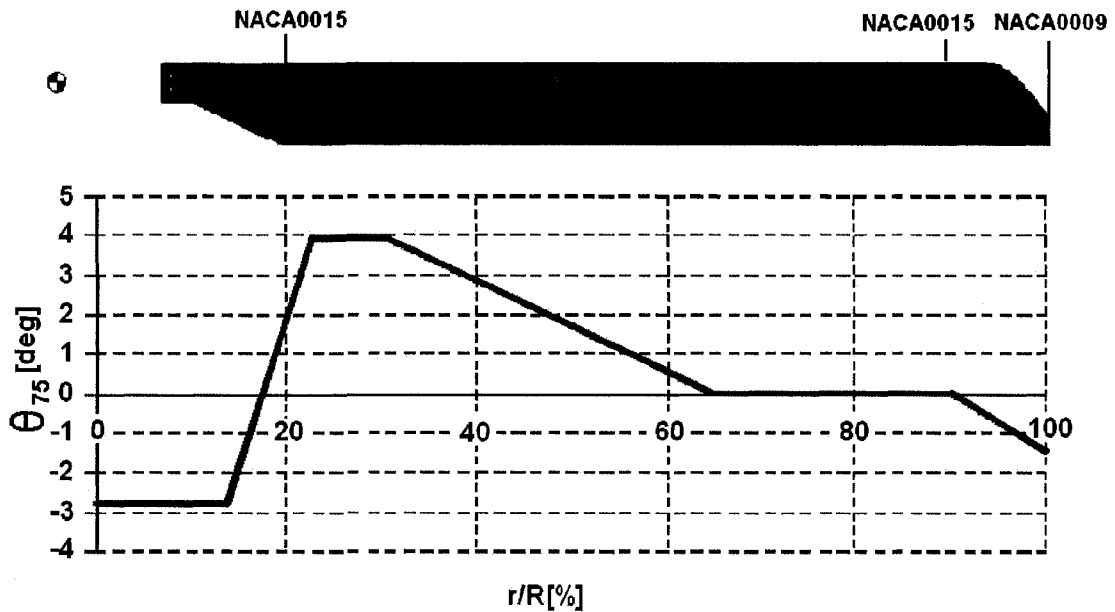


Figure 12: SHARCS rotor twist distribution, relative to the twist angle at 75% radius.

Note, from the previous figure that there is no twist between 65% to 90%, where the flap (ACF) is located. This was established to keep the flap axis a straight line.

### 2.1.3 Similarity Parameters

Acoustic similarity means that the noise generated by the sub-scale rotor should be in the range of the full-scale one. Since noise on helicopters is dictated primarily by the tip speed, this requirement essentially means maintaining the same tip Mach number. The tip Mach number for the sub-scaled rotor for SHARCS was set

to Mach 0.55. Although this was somewhat less than the Mach 0.65 characteristic of the full-scale BO-105, it provided the right compromise between the need for high tip speed still avoiding transonic effects and exceeding the maximum radial force limits applied on the rotor hub due to increased blade mass added by the actuators.

Aeroelastic similarity on the other hand, means that the structural response of the scaled blades, such as the natural frequencies in flapping, lead-lag and torsion should be similar to the full-scale blades. The first six elastic modes and corresponding natural frequencies were provided by AgustaWestland and these were used as the basis for setting the aeroelastic similarity requirements for the SHARCS blade (Ghorashi, 2005). Tab. 3 presents these data.

Table 3: Natural frequencies of mode shape for SHARCS

<b>Mode Shape</b>	<b>Frequency (/rev)</b>
1 <sup>st</sup> rigid lead-lag	0.2 ~ 0.3
1 <sup>st</sup> rigid flapping	1.02 ~ 1.04
1 <sup>st</sup> elastic beam bending	2.5 ~ 2.8
2 <sup>nd</sup> elastic beam bending	4.2 ~ 4.7
1 <sup>st</sup> elastic chord bending	4.5 ~ 5.5
1 <sup>st</sup> elastic torsion	5.5 ~ 6.0

Lock number, defined as the ratio of the blade aerodynamic forces to the blade inertial forces, is important for the prediction of rotor loads, performance and stability (Singleton, 2000). Typical Lock numbers of full-scale rotors are around 5 to 6 (Leishman, 2000). However, with three sub-systems (APL, ACF, and ACT) added

to the SHARCS rotor blade, the Lock number was increased to about 8. The Lock number similarity ensures that the excitation forces imposed on the model blade correspond in scale to those on the full-scale rotor (Ghorashi, 2005). Therefore, the similarity requirement is only partially satisfied in the SHARCS design.

#### **2.1.4 Actuation Requirements**

Recall that the role of the Actively Controlled Tip (ACT) is to displace the blade tip vortex, and thereby to reduce rotor BVI (blade slap) noise. Thus, the actuation requirement for the ACT is to be able to deflect the blade tip from 0 degrees to 20 degrees downward (Aoyama, 1996). This was thought to be sufficient to demonstrate the ACT concept. Since the ACT is of a static controller type, the maximum deflection can be achieved over several rotor revolutions. Based on this, the actuation time requirement was set to about one minute. This would correspond to about 200 to 230 rotor revolutions on a typical full-size helicopter, and to 1555 rotor revolutions on the scaled SHARCS model.

Obviously, another important criterion is that whatever actuation is selected, it has to be able to overcome the loads acting on the tip and it has to be small enough to fit inside the blade so that no extra drag (and rotor power) is generated by the system. Lastly, the actuator should be able to self-lock (staying in position) at desired

blade tip deflection.

## 2.2 Loads Acting on ACT

There are two major loads acting on the ACT; centrifugal and aerodynamic loads. This section will describe the evaluation of the centrifugal loads and how important their effect is. Then, the aerodynamic loads will be predicted by using Blade Element Momentum Theory and CFD.

### 2.2.1 Centrifugal Loads

A simple calculation of centrifugal acceleration shows how critical centrifugal loads are.

$$a_C = r_R \omega^2 \quad (8)$$

Here,  $a_C$  is the centrifugal acceleration at the tip,  $r_R$  is the rotor radius of the blade (1.096 m), and  $\omega$  is the blade tip speed, (162.8 rad/s) corresponding to the nominal 1555 RPM of the scaled rotor. This would give a centrifugal acceleration in terms of “g’s” of about 2,961 g for the last 10% of the rotor blade span. This is tremendous load acting on the blade tip that will indeed drive the selection of the type of actuator mechanism and its location. Note that under this acceleration, an actuator mechanism mass of 100 gram at the blade tip would be exposed to 296.1 kg in radial at the blade

tip.

Since the blade tip mass is given as 30 grams, a simple calculation of the centrifugal loads acting on the blade tip can be found as following (see Fig. 13).

$$F_C = m_{BT} a_C = m_{BT} r_R \omega^2 \quad (9)$$

Here  $F_C$  is the centrifugal load at the blade tip, and  $m_{BT}$  is the blade tip mass (30 grams). Thus, the centrifugal load acting on the blade tip is 871 N which is equivalent to mass of 87.1 kg “hanging” from the tip.

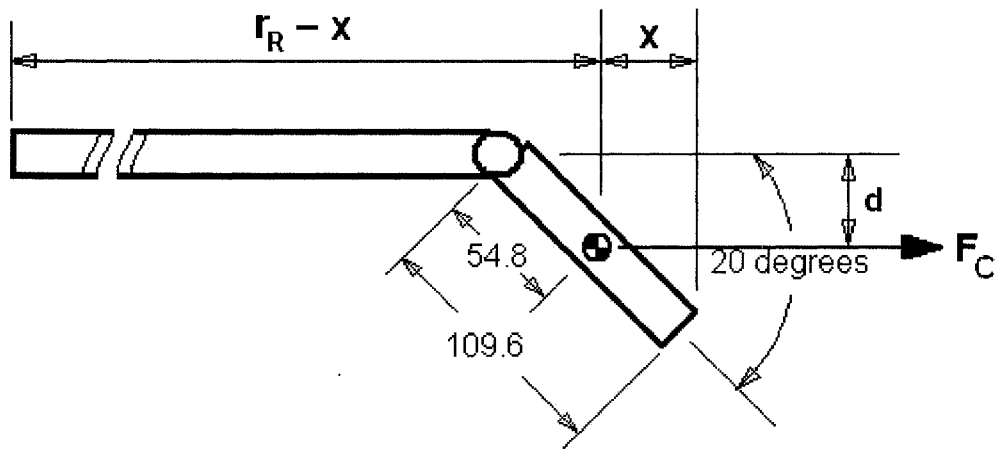


Figure 13: Schematic diagram of the blade tip and its CG location.

Fig. 13 illustrates schematic diagram of the blade tip and its CG location where the units shown are in millimeters. Note, that the hinge moment arm,  $d_{20deg}$ , is about 18.7 mm at 20 degrees deflection.

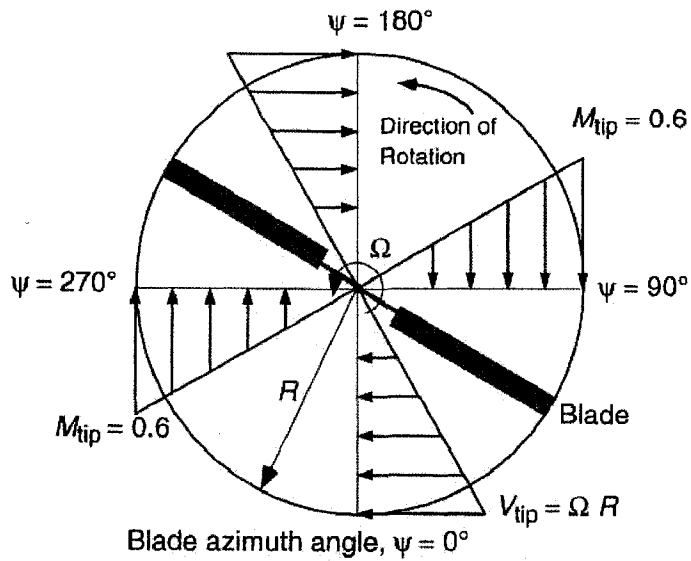
Thus, the hinge moment due to the centrifugal load at maximum blade tip speed can be evaluated as follows;

$$M_C = F_C \cdot d_{20\text{deg}} = [m_{BT} (r_R - x) \omega^2] d_{20\text{deg}} \quad (10)$$

Here,  $M_C$  is the hinge moment from the centrifugal load at the blade tip,  $x$  is the horizontal projection of length of half of the blade tip ( $54.8\cos 20^\circ$  mm), and  $d_{20\text{deg}}$  is the hinge moment arm (18.7 mm). Therefore, the hinge moment from the centrifugal load due to the blade tip deflection is estimated at 15.5 Nm.

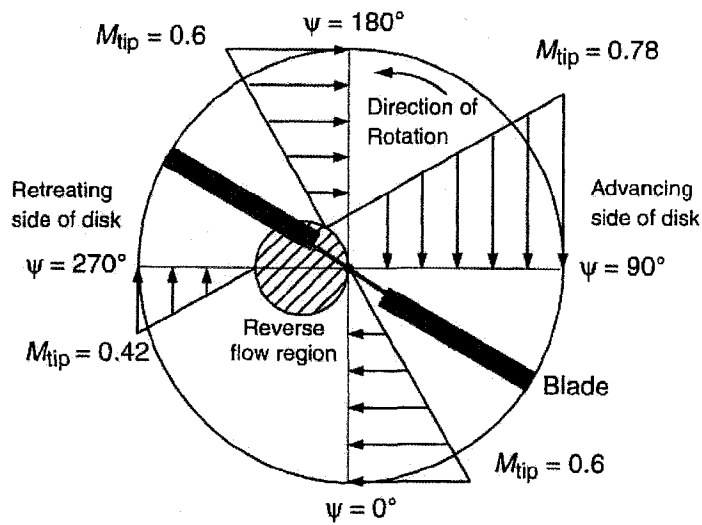
### 2.2.2 Aerodynamic Loads

For assessing the aerodynamic loads, calculations using the Blade Element Momentum Theory (BEMT) for hover were performed. BEMT is a standard numerical technique for analyzing rotor blade aerodynamics (Leishman, 2000). The hybrid BEMT method allows to predict non-uniform inflow distribution along the blade for hover and axial flight. For forward flight, empirical data based on flight tests have to be employed and, therefore, they will be omitted in a conceptual design phase. Fig. 14 presents the velocity distribution over the rotor during hover and forward flight.



a)

$V_{\infty} = 0.3 \Omega R$



b)

Figure 14: Distribution of flowfield: a) hovering flight, b) forward flight (Leishman, 2000).

For hover, the flowfield is unique and symmetric. However, to account for the increased resultant tip speed on the advancing side in forward flight, a representative (or equivalent) hover case will be considered. For this, the resultant tip speed,  $V_{RESULT}$  is determined as the sum of the speed of the rotor tip (178.4 m/s) and the speed of the

wind-tunnel test section (55 m/s). This procedure should be sufficient for first order estimates of the aerodynamic loads.

Following is a detailed description of the BEMT numerical method based on Leishman (2000).

BEMT is an iterative method, in which the root pitch angle is varied to find the desired thrust coefficient. The following steps show the iterative step by step process.

1. Discretize the blade into a series of small elements of span,  $\Delta r$  as shown in Fig. 15. Typically, a minimum of 20 elements and no more than 100 elements are recommended.

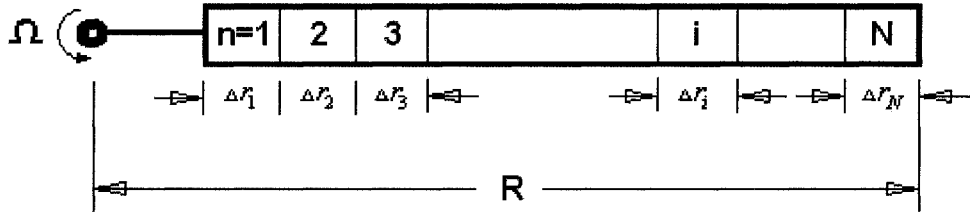


Figure 15: Discretized blade element.

2. Select the required thrust coefficient,  $C_{T,REQ}$ . This typically varies between 0.001 and 0.020 for scaled rotors.
3. The initial root pitch angle can be found by using the following equation:

$$\theta_o^0 = \frac{6C_{T,REQ}}{\sigma C_{L,\alpha}} - \frac{3}{4}\theta_{TW} + \frac{3\sqrt{2}}{4}\sqrt{C_{T,REQ}} \quad (11)$$

where  $\theta_{TW}$  is the blade twist and the initial root pitch angle becomes a

function of  $C_{T,REQ}$ .

4. Determine the pitch angle distribution,  $\theta(r)$  over the blade from the known root pitch angle,  $\theta_o$
5. The inflow ratio is now obtained using the discretized equation:

$$\lambda(r_n) = \frac{\sigma C_{L,\alpha}}{16F} \left[ \sqrt{1 + \frac{32F}{\sigma C_{L,\alpha}} \theta(r_n) r_n} - 1 \right] \quad (12)$$

Here,  $\sigma$  is the rotor solidity,  $C_{L,\alpha}$  is the slope of coefficient of lift curve of the airfoil,  $r_N$  is the non-dimensional radial position along the span of the blade,  $\theta(r_N)$  is the pitch angle at the  $N^{\text{th}}$  element, and  $\lambda(r_N)$  is the inflow ratio distribution along the span. The rotor solidity is defined as:

$$\sigma = \frac{N_b c}{\pi R} \quad (13)$$

where  $R$  is the rotor radius,  $c$  as the chord length of the blade and  $N_b$  as the number of blades.

6. For a realistic prediction, the Prandtl's Tip Loss Function must be included, which is a shape function describing the distribution of the lift along the blade. The following equation presents the Prandtl's Tip Loss Function expressed in terms of an induced velocity correction factor computed at the  $j^{\text{th}}$  element:

$$F^j(r) = \left( \frac{2}{\pi} \right) \cos^{-1} \left[ \exp - \left( \frac{N}{2} \right) \left( \frac{1-r}{r\phi} \right) \right] \quad (14)$$

where  $\phi$  is the induced angle function of the inflow ratio distribution,

$\lambda(r)$  and the radial position of the blade element:

$$\phi = \frac{\lambda(r)}{r} \quad (15)$$

In the present analysis, the shape function is found using an inflow ratio computed at Step 5.

7. Now, the tip-loss effect can be incorporated into the BEMT using the blade pitch angle from Step 3. If  $\lambda(r)^{(j+1)} \cong \lambda(r)$  from Step 5, then the shape function  $F^j(r)$  and a new inflow ratio  $\lambda^j(r)$  are finalized. Otherwise, proceed to Step 8 until convergence is achieved.

8. Once the inflow ratio at each element along the blade span is determined, the incremental thrust at each blade segment can be found using the following equation:

$$\Delta C_{T_n} = \frac{\sigma C_{L,\alpha}}{2} [\theta(r_n)r_n^2 - \lambda(r_n)r_n] \Delta r_n \quad (16)$$

9. The total thrust can then be obtained by numerical integration over the blade:

$$C_T = \sum_{n=1}^N \Delta C_{T_n} \quad (17)$$

This value is compared to  $C_{T,REQ}$ . If the two values are approximately equal, the load distribution has been found and the iteration stops. Otherwise, proceed to Step 10.

10. Determine a new blade pitch angle as:

$$\theta_o^{(j+1)} = \theta_o^{(j)} + \left[ \frac{6(C_{T,REQ} - C_\tau^{(j)})}{\sigma C_{L,\alpha}} + \frac{3\sqrt{2}}{4} \left( \sqrt{C_{T,REQ}} - \sqrt{C_\tau^{(j)}} \right) \right] \quad (18)$$

11. Go back to Step 4 and iterate.

The BEMT calculation steps can also be represented as a simple flow chart (Fig. 16).

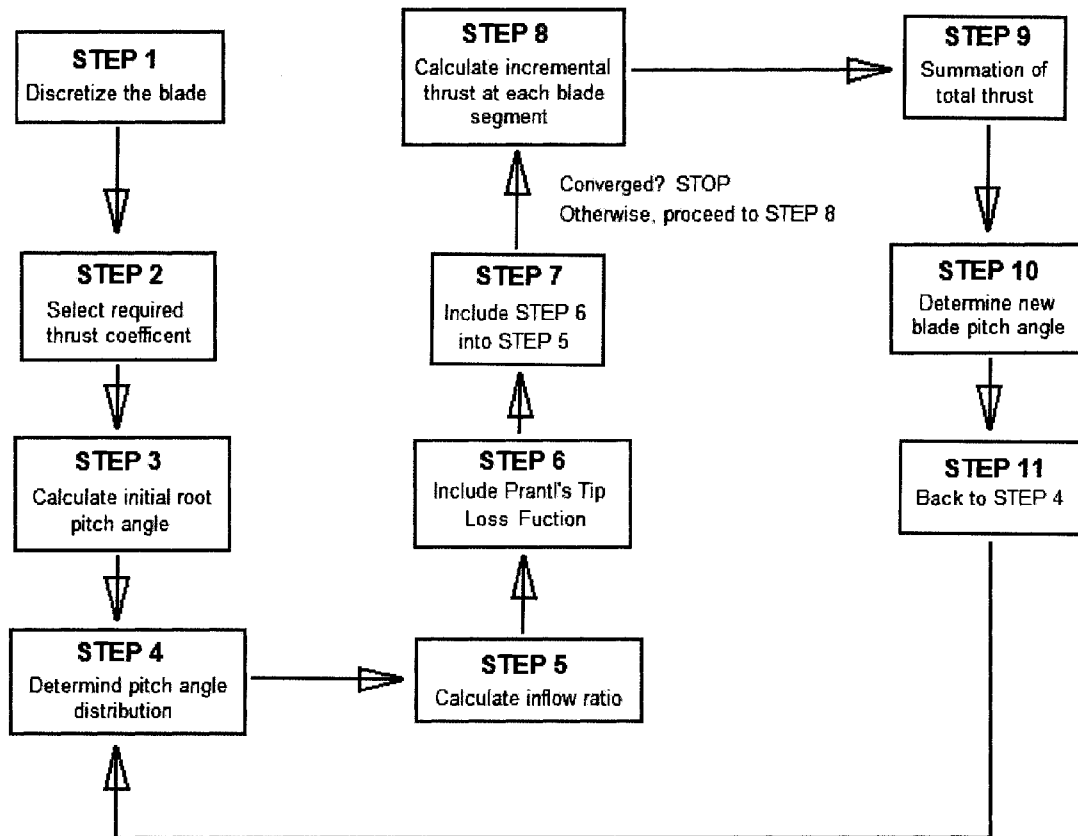


Figure 16: Flow chart of the BEMT calculations.

Using the explained numerical approach, the aerodynamic load distribution was determined for the SHARCS rotor blade for 3 different thrust coefficients (Fig. 17).

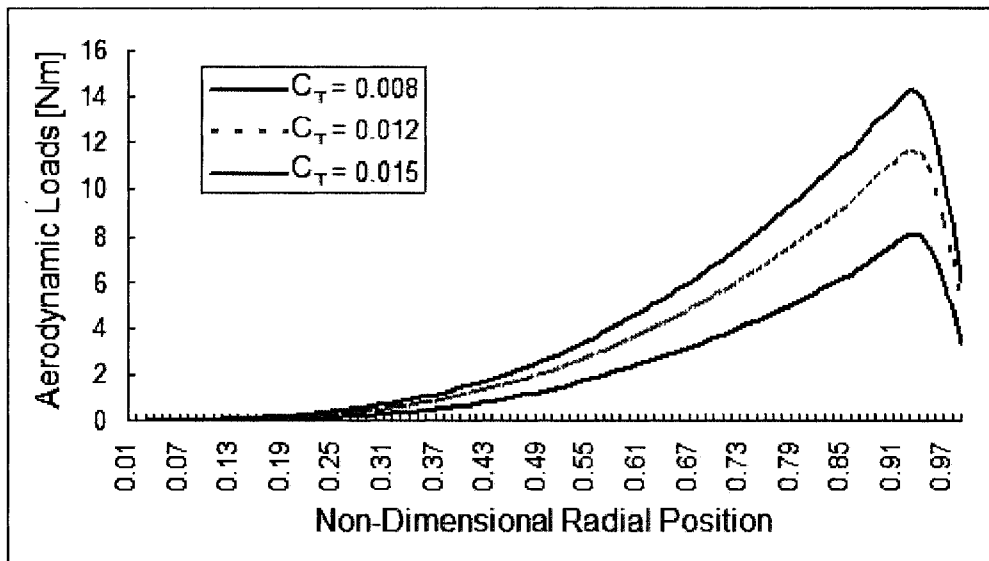


Figure 17: Aerodynamic load distribution for SHARCS.

The above figure demonstrates how different thrust coefficient could affect the final aerodynamic load on the rotor. In SHARCS, the thrust coefficient is 0.008 (Feszty, 2007). Hence, the aerodynamic load at 90% rotor blade gives from the Fig. 17, 7.37 Nm, which is not negligible and, therefore, must be considered when selecting the ACT actuator.

Fig. 18 shows the effective angle of attack for different thrust coefficient values. Since the stall occurs when the effective angle of attack goes beyond the 15 degrees limit, the ultimate thrust coefficient, representing the forward flight equivalent hover test, can be chosen from the same graph. Since the advancing blades at maximum forward flight speed will never exceed the stall angle of attack, in fact, they will stay well below it. It was decided to select the thrust coefficient of 0.008 as the ultimate thrust coefficient, representative of forward flight conditions. The

aerodynamic load at the tip was evaluated at this thrust coefficient.

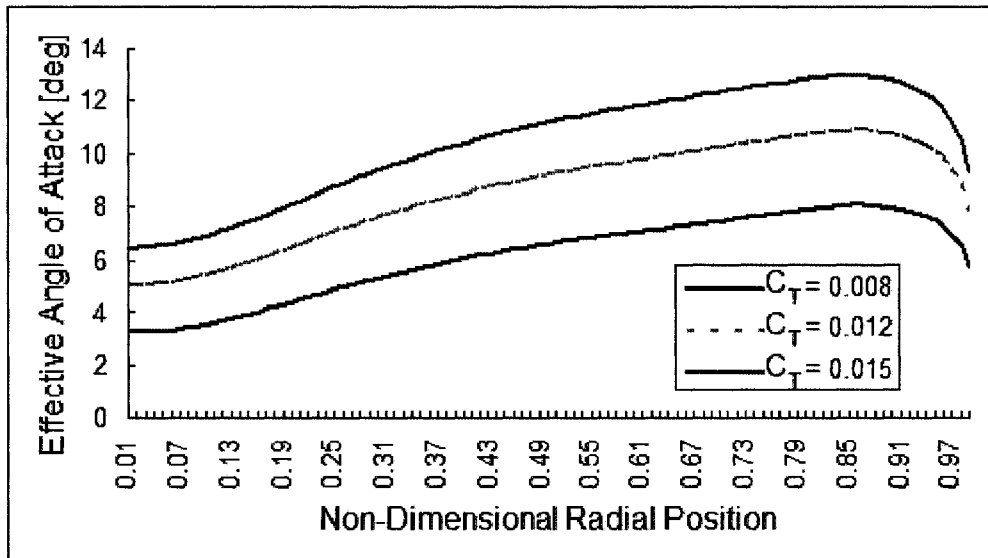


Figure 18: Effective angle of attack for various thrust coefficients.

### 2.2.3 Resultant Loads

The resultant load acting on the blade tip will be an upward hinge moment from the combined effect of the aerodynamic and centrifugal loads.

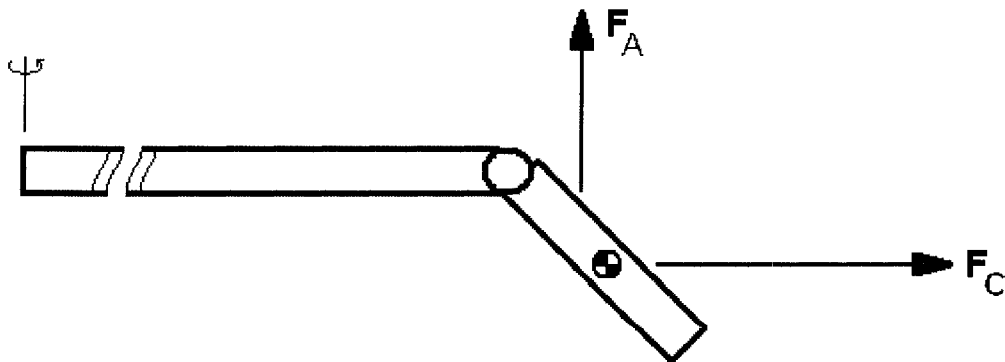


Figure 19: Schematic diagram of total hinge moment from both aerodynamic and centrifugal load.

Here,  $F_C$  is the centrifugal load and  $F_A$  is the aerodynamic load. The total

resultant load is found to be 22.9 Nm. Note that this is a high load. It corresponds to hanging a 425 kg mass to the end of the 1096 mm long SHARCS blade and trying to overcome it with a miniature actuator.

## **2.3 Design Concept**

From the previous section, it becomes obvious that the major challenge of the ACT system is the high resultant hinge moment to be overcome. A strong actuator with high torque yet small in size, fitting inside the blade, is required to be designed.

Firstly, Shape Memory Alloy (SMA) wires were considered for the ACT actuator. SMA is a “smart” material that after having submitted to a deformation returns to its original “memorized” shape when heat is applied. A feasibility study on employing SMA wires for the ACT actuation has shown that SMA wires could not provide enough torque to overcome the resultant hinge moment at the tip because each SMA wire could theoretically produce only a torque of 0.16 Nm (Lynch, 2007). The main reason is the small moment arm available inside the blade, which is limited by the blade thickness (about 8 mm for the SHARCS blade). In addition, the maximum hinge moment produced by the SMA experimental setup was only half of a theoretical value, 0.08 Nm (Lynch, 2007). As explained in a previous section, the Italian aerospace research centre, CIRA have also tried to use SMA wires to actively control

the blade tip but had no success in a sub-scaled demonstrator rotor (Testa, 2006). Both experiments have concluded that a small and light actuator, yet with large enough torque, was impossible to find.

However, not only SMA wires were considered for a suitable ACT actuator but also an inchworm actuator was considered. An inchworm actuator, also known as a piezo-walker was studied. The inchworm is a relatively new technology among smart materials. The technical specs for the inchworm obtained from EXPO Life Sciences and Industrial Division stated that the push/pull force it can generate is about 10 N. Given the extremely small moment arm available, this option again had to be discarded for the ACT.

Clearly, a major challenge is the high resultant hinge moment at the blade tip and the limited space available inside the scaled blade. An original idea conceived within the SHARCS design team was, therefore, to minimize the hinge moment by employing a counter-weight mechanism, which attempts to take advantage of the high centrifugal loads acting at the blade tip. This will be described next after reviewing the design requirements of the ACT.

### **2.3.1 Design Requirements of the ACT**

Before discussing the proposed novel actuator design, let us summarize the

contradicting design requirements for the ACT.

1. It has to be able to overcome the resultant hinge moment of 22.9 Nm. This hinge moment is the sum of the centrifugal loads and the aerodynamic loads acting on the rotor blade from 90% to 100% radius.
2. It has to be housed in the blade in a way so that the aerodynamic drag is not compromised. The ideal would be to have the actuator INSIDE the blade. However, space is very limited (70 mm x 10 mm cross-section).
3. It has to be light. Heavier components at the blade tip mean more centrifugal load and larger resultant hinge moment to overcome by the ACT actuator.
4. It has to be able to deflect from zero to 20 degrees in about one minute. If the operational time is too long, the actuator is not suitable. The ACT will only be activated by the pilot before a specific maneuver/flight regime, such as the forward flight descent, etc.
5. It has to operate in a potential field dominated by extreme centrifugal loads (2,961 g's) with the ACT mechanism located at 90% of the rotor radius of the blade.

All these challenges put extreme requirements on the design of the ACT system. This could be the main reason why no research or production helicopters feature such control mechanism.

### **2.3.2 Actuator Concept**

It has been shown in the previous section that so far, only two different actuator concepts have been considered for the Actively Controlled Tip, namely: Shape Memory Alloys (Lynch, 2007) and inchworm actuator from EXPO Life Sciences and Industrial Division. Neither of them proved to be feasible because of the low actuator force/stroke combination that smart materials can offer at this level of the development of the technology.

This thesis focus at a third type of actuation, (electromechanical) which, although a little more conservative, seems to be more feasible. It is based on using a miniature electrical motor, driving a screw-jack like mechanism to deflect the blade tip.

A major novelty of this concept is, however, the separation of the actuator itself from the actuator mechanism by placing the actuator at the blade root and the actuator mechanism at the blade tip. This concept brings two advantages:

1. The actuator can be placed at the root where the centrifugal loads are significantly smaller (593 g's at 20% of the radius). The electrical motor can operate in a more "liveable" environment; at the blade root than at the blade tip. Also, the motor can possibly be placed outside the blade airfoil, where the

drag effect is small in comparison to that at the blade tip. Note that the bulky nature of the rotor hub already creates considerable drag at the blade root. The power of the motor is proportional to the diameter of the motor. Thus, locating a powerful motor at the blade tip would create drag which can be compromised.

2. The actuation mechanism can be placed at the blade tip. Obviously, this mechanism has to be designed small enough to fit inside the blade. Also, it is exposed to extreme centrifugal loads, which is normally undesired. However, with a clever design, one can also make use of the centrifugal loads to alleviate the actuation force requirement.

### **2.3.3 The Counter-Weight Concept**

The key idea of the counter-weight concept is to make use of the extreme centrifugal loads, and to allow the blade tip to rotate freely without any actuation from 0 degree to 10 degrees. Beyond this point, the actuator power will be used to complete the blade tip motion down to 20 degrees (see Fig. 20). The same applies for the blade tip deflecting upward in the opposite way, i.e. no actuation is required from 20 degrees to 10 degrees, and the actuator is powered from 10 degrees to 0 degrees. With this design, the hinge moment requirement on the actuator can essentially be halved.

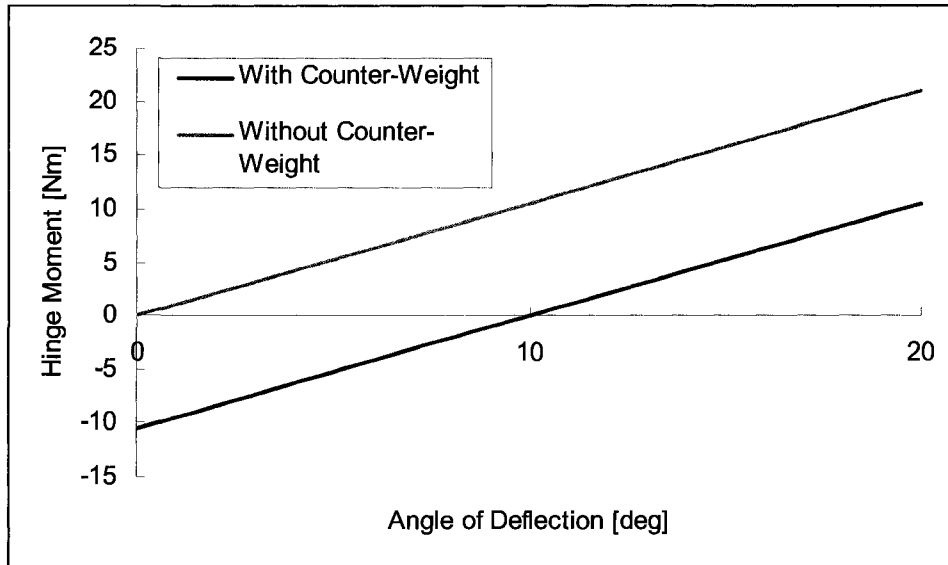


Figure 20: Hinge moment with/without counter-weight for centrifugal load.

This is the novelty of this concept. Obviously, the counter-weight has to be sized so that the zero moment point occurs at 10 degree deflection instead of 0 degree as illustrated in Fig. 21.

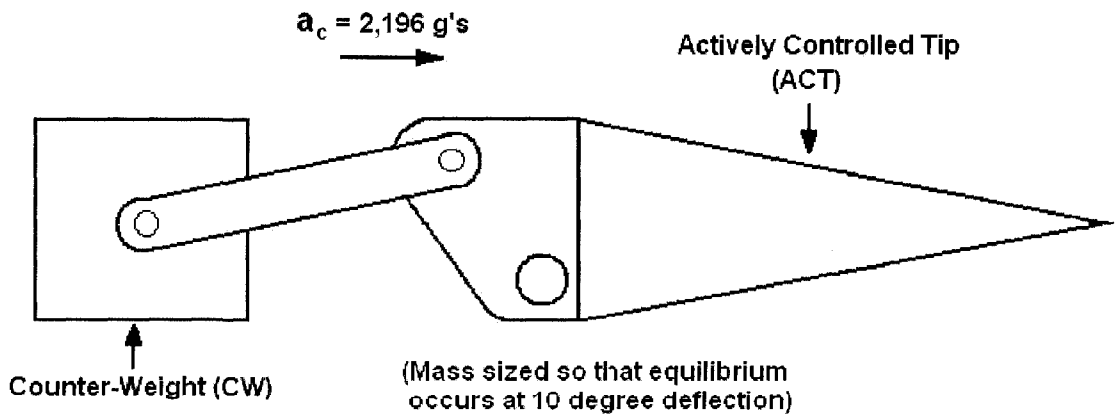


Figure 21: Schematic diagram of counter-weight concept.

### 2.3.4 Screw-Jack Mechanism

Instead of generating the hinge moment from translational motions such as for the inchworm and SMA concepts, torque will be generated by rotational motion by an electric motor located at the blade root and translated to the tip via a torque rod running along the blade (Fig. 22).



Figure 22: Location of ACT and its actuator in SHARCS Blade.

Few mechanisms are needed to transfer rotary motion into a linear motion so that the blade tip could pivot to deflect downward. As Fig. 22 illustrates, the two components (Actuator and Actuator Mechanism) are connected using a composite tube to reduce the weight of the ACT blade system.

### 2.4 Scaled Model Design

The sizing of the ACT mechanism components is critical since the SHARCS blade must be light in order to minimize the centrifugal loads. The counter-weight mechanism has 4 major components: the counter-weight (CW), the link (LINK), the part housing the hinge (TIP) and the composite anhedral tip itself (ANH) as shown in

Fig. 23. Since the LINK connects the CW and the TIP, as the CW moves radially outward the TIP rotates in clockwise direction to deflect the blade tip down.

#### 2.4.1 The Counter-Weight Sizing

As it was mentioned previously, the basic idea behind the ACT CW concept is to achieve zero hinge moment at 10 degree deflection, i.e. at the midway point of the total stroke. The blade geometry was given in Tab. 2 while the maximum resultant hinge moment to be overcome was found to be 22.9 Nm without the CW concept and 11.45 Nm (half of the latter value) with the CW concept.

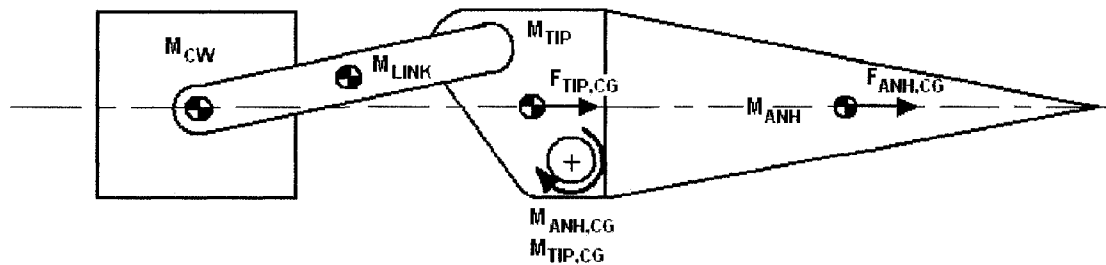


Figure 23: ACT's components part name.

Using the resultant hinge moment, the mass for the CW was estimated. The design process is iterative since nothing was given except for the mass of the composite blade tip (30 grams) and the angular velocity of the rotor blade (162.8 rad/s). Fig. 24 shows the geometry of the system. From this figure, the equations of motion were obtained to solve the hinge moment arising at the hinge location "A".

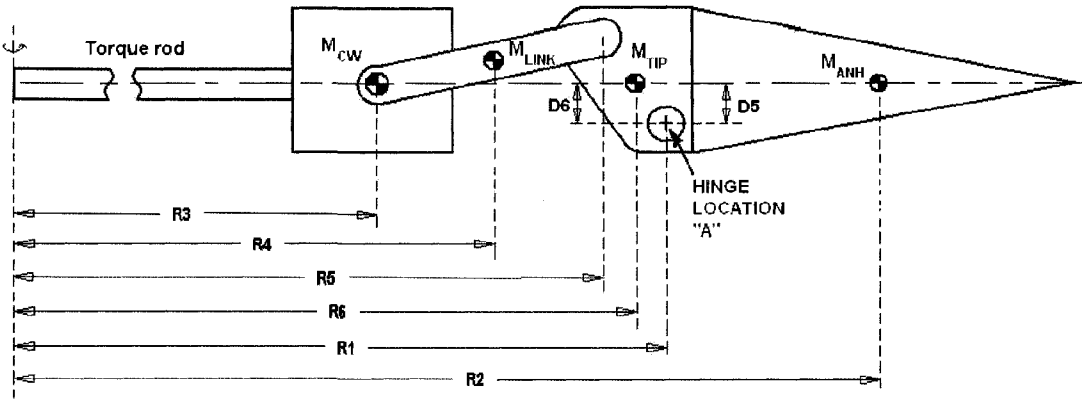


Figure 24: ACT's components centre of gravity location.

First, the kinematics of the system has to be determined. Tab. 4 shows the variation of the centre of gravity (CG) location with increasing tip deflection. Obviously, the CG location of each component is changing as the blade tip is deflected down, except for the hinge location, "A". Since we will evaluate the centrifugal loads acting on each component, the radial locations were derived:

$$R_1 = 0.9864 \quad (19)$$

$$R_2 = 0.9864 + 0.054846 \cos(2.35^\circ - \delta) = 0.9864 + D_1 \quad (20)$$

$$R_3 = 0.9864 - 0.01 \cos \phi - 0.0057 \cos(52.125^\circ + \delta) = 0.9864 - D_3 - D_4 \quad (21)$$

$$R_4 = 0.9864 - \frac{0.01 \cos \phi}{2} - 0.0057 \cos(52.125^\circ + \delta) = 0.9864 - D_3 - \frac{D_4}{2} \quad (22)$$

$$R_5 = 0.9864 - 0.0057 \cos(52.125^\circ + \delta) = 0.9864 - D_3 \quad (23)$$

$$R_6 = 0.9864 - 0.00285 \cos(52.125^\circ + \delta) = 0.9864 - D_2 \quad (24)$$

Table 4: Variation of the ACT components' CG with blade tip deflection

$\delta$ [deg]	$R1$ [mm]	$R2$ [mm]	$R3$ [mm]	$R4$ [mm]	$R5$ [mm]	$R6$ [mm]
0	0.9864	1.0412	0.9732	0.9780	0.9829	0.9847
2	0.9864	1.0412	0.9733	0.9782	0.9831	0.9847
4	0.9864	1.0412	0.9735	0.9784	0.9832	0.9848
6	0.9864	1.0411	0.9737	0.9785	0.9834	0.9849
8	0.9864	1.0410	0.9738	0.9787	0.9836	0.9850
10	0.9864	1.0408	0.9740	0.9789	0.9837	0.9851
12	0.9864	1.0405	0.9742	0.9790	0.9839	0.9852
14	0.9864	1.0401	0.9744	0.9792	0.9841	0.9852
16	0.9864	1.0397	0.9745	0.9794	0.9843	0.9853
18	0.9864	1.0392	0.9747	0.9796	0.9845	0.9854
20	0.9864	1.0387	0.9749	0.9798	0.9847	0.9855

Fig. 25 shows the free-body diagram for each component, depicting the centrifugal forces, reaction forces and moments on the ACT. On the basis of these, the following equations of motion were derived:

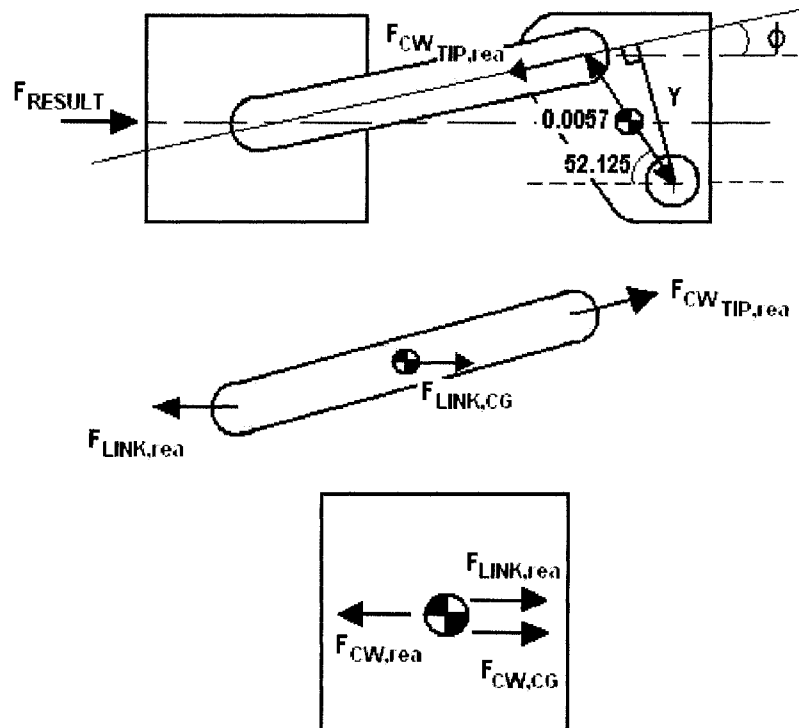


Figure 25: Free body diagram for the actuator mechanism components.

$$F_{ANH,CG} = m_{ANH} R_2 \omega^2 = m_{ANH} [0.9864 + 0.054846 \cos(2.35^\circ - \delta)] \omega^2 \quad (25)$$

$$M_{ANH,CG} = F_{ANH,CG} D_5 = m_{ANH} R_2 \omega^2 [0.054846 \sin(2.35^\circ - \delta)] \quad (26)$$

$$F_{TIP,CG} = m_{TIP} R_6 \omega^2 = m_{TIP} [0.9864 - 0.00285 \cos(52.125^\circ + \delta)] \omega^2 \quad (27)$$

$$M_{TIP,CG} = F_{TIP,CG} D_6 = m_{TIP} R_6 \omega^2 [0.00285 \sin(52.125^\circ + \delta)] \quad (28)$$

$$F_{TIP,reaction} = \frac{M_{ANH,CG} + M_{TIP,CG}}{Y} = \frac{M_{ANH,CG} + M_{TIP,CG}}{0.0057 \sin(\phi + 52.125 + \delta)} \quad (29)$$

$$\begin{aligned} F_{LINK,CG} &= 2 [m_{LINK} R_4 \omega^2] \\ &= 2 \left[ m_{LINK} \left\{ 0.9864 - \frac{0.01 \cos \phi}{2} - 0.0057 \cos(52.125 + \delta) \right\} \omega^2 \right] \end{aligned} \quad (30)$$

$$F_{LINK,reaction} = F_{TIP,reaction} \cos \phi + F_{LINK,CG} \quad (31)$$

$$\begin{aligned} F_{CW,CG} &= m_{CW} R_3 \omega^2 \\ &= m_{CW} [0.9864 - 0.01 \cos \phi - 0.0057 \cos(52.125 + \delta)] \omega^2 \end{aligned} \quad (32)$$

$$F_{CW,reaction} = F_{LINK,reaction} + F_{CW,CG} = F_{RESULT} \quad (33)$$

Tab. 5 and 6 present the centrifugal force and ACT components reaction forces due to the centrifugal acceleration from 0 degree deflection to 20 degree deflection.

Table 5: Centrifugal and reaction forces on anhedral and tip

$\delta[\text{deg}]$	$F_{ANH,CG}[N]$	$M_{ANH,CG}[Nm]$	$F_{TIP,CG}[N]$	$M_{TIP,CG}[Nm]$	$F_{TIP,rea}[N]$
0	828.38	1.86	438.70	0.99	551.10
2	828.42	0.28	438.73	1.01	245.14
4	828.40	-1.31	438.77	1.04	-50.57
6	828.33	-2.89	438.81	1.06	-338.58
8	828.21	-4.47	438.85	1.08	-619.84
10	828.03	-6.05	438.89	1.11	-895.18
12	827.80	-7.61	438.92	1.13	-1165.38
14	827.52	-9.16	438.96	1.14	-1431.16
16	827.19	-10.71	439.01	1.16	-1652.21
18	826.80	-12.23	439.05	1.18	-1952.21
20	826.37	-13.74	439.09	1.19	-2208.74

Table 6: Centrifugal and reaction forces on link and counter-weight

$\delta[\text{deg}]$	$F_{LINK,CG}[N]$	$F_{LINK,rea}[N]$	$F_{CW,CG}[N]$	$F_{CW,rea}[N]$	$F_{RESULT}[N]$
0	36.31	573.29	771.20	1344.49	1344.49
2	36.32	274.84	771.34	1046.18	1046.18
4	36.32	-12.88	771.47	758.59	758.59
6	36.33	-293.07	771.60	478.53	478.53
8	36.34	-566.70	771.74	205.04	205.04
10	36.34	-834.56	771.88	-62.69	-62.69
12	36.35	-1097.43	772.02	-325.42	-325.42
14	36.36	-1356.01	772.16	-583.85	-583.85
16	36.36	-1610.96	772.31	-838.65	-838.65
18	36.37	-1862.91	772.45	-1090.46	-1090.46
20	36.38	-2112.48	772.60	-1339.88	-1339.88

Note that for component sizing purpose, the most important column in Tab. 6 is the last one, i.e. the resultant force ( $F_{RESULT}$ ) to be applied on the counter-weight. At zero degree deflection, the resultant force is +1344.49 N and at 20 degree deflection, the resultant force is -1339.88 N (see Fig. 26).



Figure 26: Resultant acting on the screw-jack mechanism.

The latter is the force that the actuation mechanism will have to be able to exert in order to deflect the blade tip 20 degrees downward. But, as it was stated previously, this force has to be applied in the range between 10 degree and 20 degree deflection only.

#### 2.4.2 Motor Requirements

The torque required for the motor is found using power-screw equations (Shigley, 1956). The final torque is evaluated by considering a safety factor of 1.5. On a screw, the torque,  $T$  required to overcome the thread friction and raise the load,  $F$  through the threads can be found as:

$$T = \frac{Fd_m}{2} \times \frac{(L + f\pi d_m)}{\pi d_m - fL} \quad (34)$$

Here,  $d_m$  is the mean thread diameter of the screw,  $L$  is the vertical length of the

lead and  $f$  is the coefficient of dynamic thread friction (see Fig. 27).

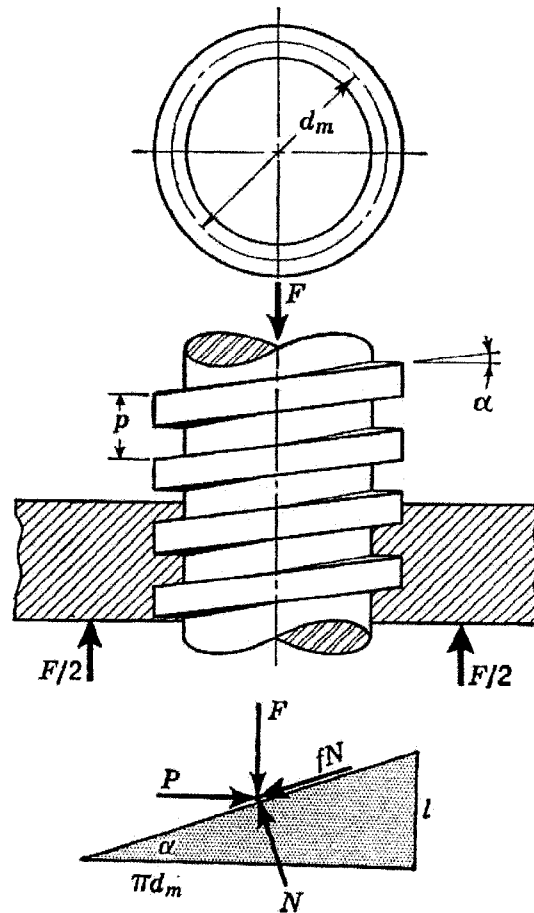


Figure 27: Schematic diagram of power screw (Shigley, 1956).

Note that in the Fig. 27,  $p$  is the screw pitch,  $\alpha$  is a helix angle,  $fN$  is the friction force, and  $P$  is the necessary force to overcome the friction force and push the load up on the inclined plane.

In addition, more torque is required to overcome the collar bearing friction:

$$T_C = \frac{F f_c d_c}{2} \quad (35)$$

Here,  $T_C$  is the torque required to overcome the collar bearing friction,  $f_c$  is the coefficient of collar friction,  $d_c$  is the mean collar diameter and  $F$  is the force



Table 7: Torque required for ACT to overcome resultant loads

$\delta$ [deg]	$T$ [Nm]	$T_C$ [Nm]	$T_{RESULT}$ [Nm]	$T_{SF}$ [Nm]
0	1.14	0.66	1.80	2.70
2	0.89	0.51	1.40	2.10
4	0.64	0.37	1.01	1.52
6	0.41	0.23	0.64	0.96
8	0.17	0.10	0.27	0.41
10	-0.05	-0.03	-0.08	-0.13
12	-0.28	-0.16	-0.44	-0.65
14	-0.50	-0.28	-0.78	-1.17
16	-0.71	-0.41	-1.12	-1.68
18	-0.93	-0.53	-1.46	-2.19
20	-1.14	-0.65	-1.79	-2.69



Figure 29: Required motor torque variation with deflection angle.

Fig. 29 shows that the torque is not balanced exactly at 10 degrees deflection but at 9.5 degrees. The reason is due to round-off errors in the calculations. As explained before, the motor only needs to apply torque from 10 degrees to 20 degrees

when deflecting the blade tip down. When the tip is returned to its original position (i.e. moving upward), it only needs to apply torque from 10 degrees to zero degree. Because of the screw-jack mechanism, the motor obviously has to be rotated outside these ranges, but it has to provide only minimal power to overcome friction between threads. The most important conclusion is that the electric motor for the ACT actuator has to provide a torque of 2.70 Nm.

### **2.4.3 Motor Selection**

Instead of considering a DC motor with a rotary actuation system alone, other actuation systems such as hydraulic, stepper motor, and linear actuation system were carefully evaluated. There were several priorities when searching for new actuation systems; being powerful enough, being compact in size, and finally requiring reasonable power supplies. Tab. 8 presents the summary of the actuator motor search for both DC, stepper, hydraulic and linear actuators.

Table 8: Summary of the actuator motor search:

a) DC motor, b) Stepper motor, c) Hydraulic actuator, d) Linear actuator

<b>DC Motor</b> <b>Category</b>	<b>RE30-268214</b> <b>(Maxon Motor)</b>	<b>16BHS-3C-E</b> <b>(Portescap, Danaher)</b>	<b>1628-T-012B</b> <b>(Faulhaber)</b>
<b>Power (W)</b>	60	4.4	10
<b>Continuous Torque (Nm)</b>	0.085	0.0042	0.011
<b>Axial Load (N)</b>	5.6	2	10
<b>Radial Load (N)</b>	28	5	17
<b>Diameter (mm)</b>	30	16	16
<b>Length (mm)</b>	68	Not Known	28
<b>Mass (kg)</b>	0.238	0.033	0.031

a)

<b>Stepper Motor</b> <b>Category</b>	<b>LH1112-09</b> <b>(EAD Motors)</b>	<b>TSM15-180-12-5V-050A-PINS</b> <b>(Anaheim Automation)</b>	<b>CRK513PAP, 5-Phase Micro-stepping, (Oriental Motor)</b>
<b>Power (W)</b>	2.55	2.5	16.8
<b>Continuous Torque (Nm)</b>	0.067	0.19	0.023
<b>Axial Load (N)</b>	Not Known	0.08	10
<b>Radial Load (N)</b>	Not Known	0.06	5
<b>Diameter (mm)</b>	27.9	15	20
<b>Length (mm)</b>	31.5	22	28
<b>Mass (kg)</b>	0.1134	Not Known	0.05

b)

<b>Hydraulic Rotary Actuator</b> <b>Category</b>	<b>CLQB 40 (SMC)</b>	<b>HRN10S (Parker)</b>	<b>L10-1.7" (Helac)</b>
<b>Max. Operating Pressure (MPa)</b>	1	7	Not Known
<b>Min. Operating Pressure (MPa)</b>	0.2	1	Not Known
<b>Travel Distance (mm)</b>	20	Not Known	Not Known
<b>Output Torque (Nm)</b>	Not Known	2	190
<b>Thrust Load (N)</b>	Not Known	4.9	907 kg
<b>Radial Load (N)</b>	Not Known	9.8	907 kg
<b>Diameter (mm)</b>	52	58	100
<b>Length (mm)</b>	70.5	95	140
<b>Holding Force (N)</b>	629	Not Known	Not Known
<b>Mass (kg)</b>	0.56	1	6

c)

<b>Linear Actuator</b> <b>Category</b>	<b>FA-05-12-06 (Firgella Automations)</b>	<b>CRES200-130-12-E (CRES, Rod Actuator)</b>	<b>WZ60 (Wiesel Vario Line)</b>
<b>Stroke Length (mm)</b>	152.4	50	400
<b>Thrust Force (N)</b>	666	200	2800
<b>Pulling Force (N)</b>	666	Not Known	Not Known
<b>Holding Force (N)</b>	666	Not Known	Not Known
<b>Height/Diameter (mm)</b>	44.96	75	88
<b>Width (mm)</b>	44.96	47	60
<b>Length (mm)</b>	368.3	272	430

d)

Unfortunately, some information was not made available from the manufacturers. However, it is still evident that most of the non-DC type actuators are too large to fit inside the 12 mm available thickness of the NACA0015 airfoil. The large size actuator is usually associated with excessive mass too, often in the order of

the total blade mass (around 600 grams), which would not be acceptable. As stated earlier, the size of the ACT actuator system is, therefore, very crucial.

The final decision was made to use a DC motor as the ACT actuator because the DC motor was the most compact compared to the other actuation systems while providing reasonable torque. Thus, the Maxon RE 30 motor (Tab. 9) with a Maxon GP 32C gearhead (Tab. 10) were chosen; this system provides 6 Nm torque, and is only 32 mm x 68 mm in size, weighing 0.496 kg. Although the motor is larger than the blade cross section in size, a novel design could solve this problem (see next section). Tab. 9 and 10 present the additional characteristics of the motor and gearhead system to be used for the control analysis.

Table 9: Maxon RE 30 DC motor additional characteristics

Parameters	Values
Moment of Inertia, $J_m$ ( $Kg \cdot m^2 / sec^2$ )	$3.45 \times 10^{-6}$
Damping Constant, $b_m$ ( $Nm \cdot sec / rad$ )	$1.15 \times 10^{-3}$
Torque Constant, $K_t$ ( $Nm / A$ )	0.0538
Back emf Constant, $K_e$ ( $V / RPM$ )	$5.62 \times 10^{-3}$
Electric Resistance, $R$ ( $\Omega$ )	2.52
Electric Inductance, $L$ ( $H$ )	$5.13 \times 10^{-4}$
Supply Voltage ( $V$ )	48

Table 10: Maxon GP 32C gearhead additional characteristics

Parameters	Values
Reduction Ratio	103:1
Max. Continuous Torque ( $Nm$ )	6
Efficiency (%)	70
Moment of Inertia of the Load, $J_L$ ( $Kg \cdot m^2 / sec^2$ )	$7 \times 10^{-8}$
Size, Length x Diameter, (mm)	56.4 x 32
Mass (grams)	258

#### 2.4.4 Overall Assembly

Fig. 30 presents the final SHARCS scaled blade assembly incorporating the ACT actuation system. Note that the actuator is located at the root and turned 90 degrees relative to the radial direction. This is to avoid excessive axial loads acting on the motor and gearhead, which is better at withstanding radial than axial loads.

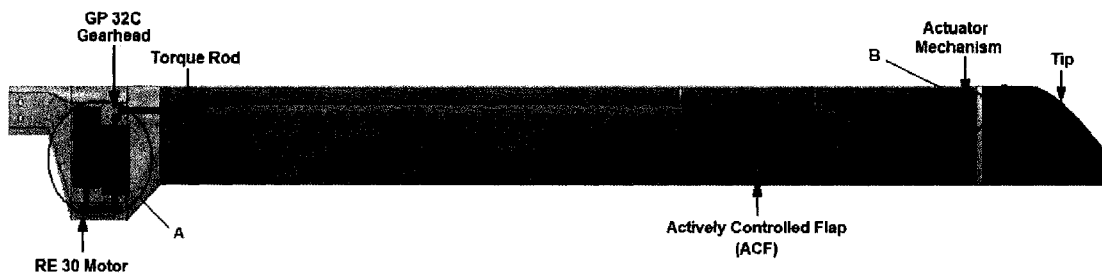


Figure 30: SHARCS scaled blade with ACT actuator in perpendicular direction.

The ACT actuator is located inside the blade, however, in order to facilitate this assembly, a special root transition to housing the new actuator has been introduced. “A” is the motor with the gearhead assembly (turned 90 degrees) located at the blade root. The output shaft of the gearhead is connected through a torque rod

to the actuator mechanism located at the blade tip. The gearhead is needed to magnify the output torque from the motor and also to decrease the motor speed. The torque rod is an off-the-shelf component. It is located at the leading edge of the blade to reduce the leading edge balance mass. The torque rod transfers the motion from the motor and the gearhead to the actuator mechanism. “B” is the counter-weight mechanism. All actuator components are sized to minimize the resultant loads. Most of ACT components are fabricated out of titanium to reduce the total mass of the ACT system and to increase the strength of each component. Fig. 31 shows the close up view of the root transition.

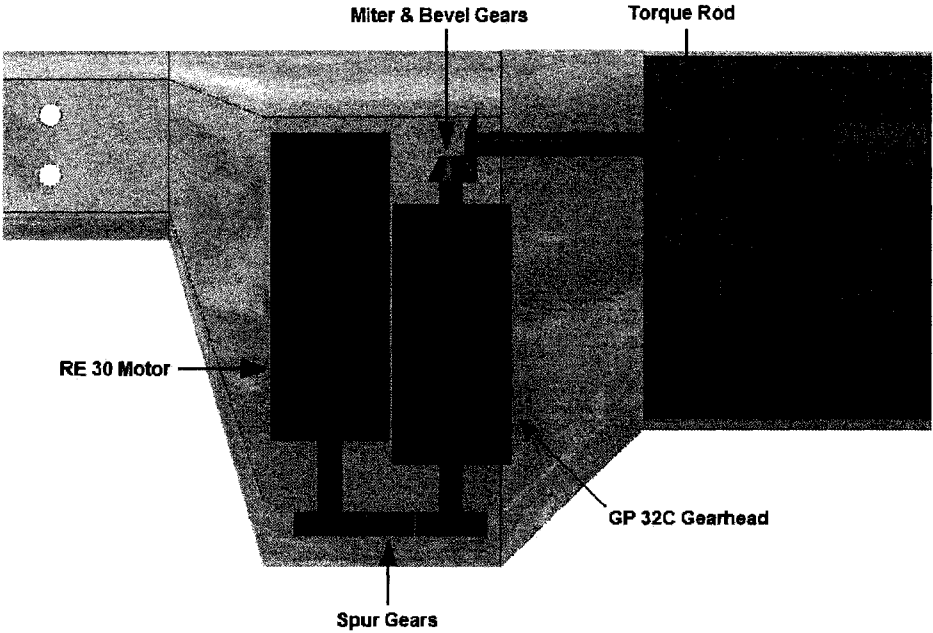


Figure 31: Close up view of the root transition.

The final mass of the ACT components was optimized; the results shown in Tab. 11 and the final design is shown in Appendix A.

Table 11: Final mass of ACT components

<b>Part Name</b>	<b>Mass (grams)</b>	<b>Material</b>
m_CW	30	Lead
m_TIP	16.8	Titanium
m_LINK	0.7	Titanium
Horseshoe	8.14	Titanium
m_ANH	30	Composite

#### 2.4.5 Manual Setup Version

The SHARCS proof-of-concept wind tunnel campaign to be conducted at AgustaWestland in early 2008, to prove the noise reduction effect of the ACT required the design of a manual setup alternative of the ACT actuator mechanism. This should allow the ACT to be deflected manually in each test scenario. If successful, the moving ACT will be incorporated into the 2<sup>nd</sup> phase of tests. Fig. 32 and 33 show the geometry of a self-locking system designed for the proof-of-concept tests. Since the LINK is pinned with the NUT and the PIVOT, as the operator turns the screw using a screw driver, the NUT will move upward. As it rises, the PIVOT will turn clockwise to deflect the blade tip. This is based on the same concept as the CW mechanism.

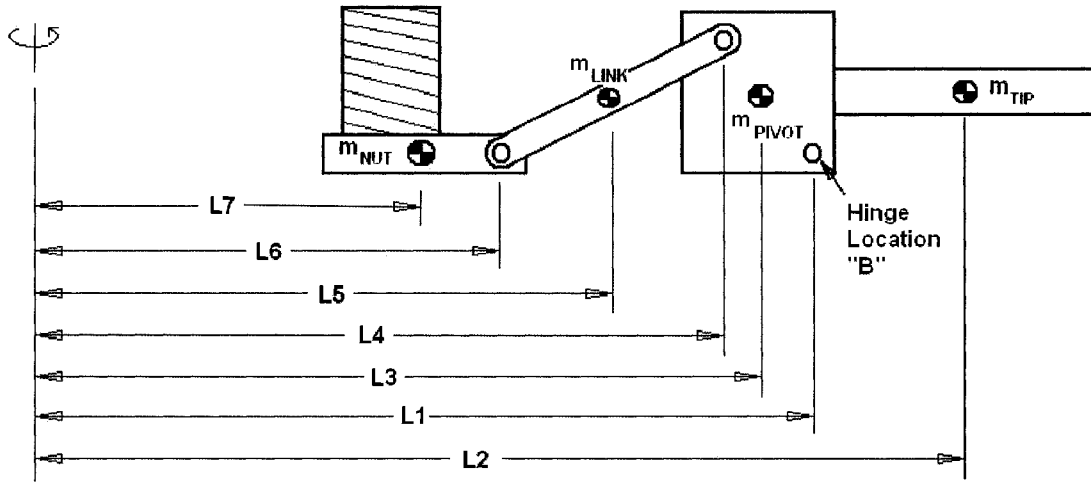


Figure 32: Location of self-lock mechanism's components.

$$L1 = 0.9864 \quad (36)$$

$$L2 = 0.9864 + 0.05486 \cos(2.61^\circ - \delta) \quad (37)$$

$$L3 = 0.9864 - 0.00269 \cos(68.2^\circ + \delta) \quad (38)$$

$$L4 = 0.9864 - 0.005385 \cos(68.2^\circ + \delta) \quad (39)$$

$$L5 = 0.9864 - \frac{0.008}{2} \cos(38.7^\circ - \delta) - 0.005385 \cos(68.2^\circ + \delta) \quad (40)$$

$$L6 = 0.9864 - 0.008 \cos(38.7^\circ - \delta) - 0.005385 \cos(68.2^\circ + \delta) \quad (41)$$

$$L7 = 0.9864 - (0.002 + 0.002 + 0.008 \cos 38.7^\circ) \quad (42)$$

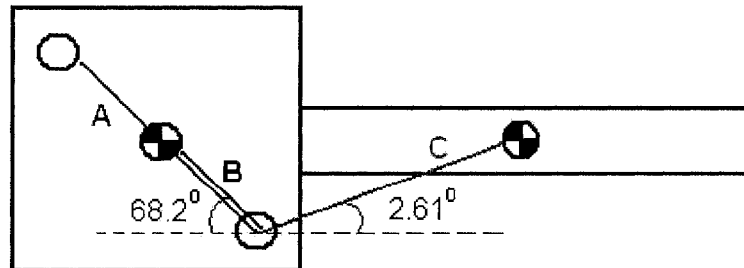


Figure 33: Pivot component's geometry.

Here,  $A = 0.005385$ ,  $B = 0.00269$ ,  $C = 0.05486$ , the length of the link

chosen to be 8 mm, and  $\delta$  is the deflection from zero to 20 degrees. Also, using the same methods as described earlier by Eqs. (25) to (33), the force, and moments on the self-locking mechanism can be calculated from zero to 20 degrees deflection (see Tab.

12). The reason for designing this feature is to ensure the “self-locking” of the blade tip at desired deflection angle.

Table 12: Variation of the ACT manual setup version components’  
CG with blade tip deflection

$\delta$ [deg]	$L1$ [mm]	$L2$ [mm]	$L3$ [mm]	$L4$ [mm]	$L5$ [mm]	$L6$ [mm]
0	0.9864	1.0412	0.9854	0.9844	0.9822	0.9801
2	0.9864	1.0413	0.9855	0.9846	0.9824	0.9803
4	0.9864	1.0412	0.9856	0.9848	0.9826	0.9804
6	0.9864	1.0412	0.9857	0.9849	0.9828	0.9806
8	0.9864	1.0410	0.9858	0.9851	0.9830	0.9808
10	0.9864	1.0408	0.9858	0.9853	0.9831	0.9810
12	0.9864	1.0405	0.9859	0.9855	0.9833	0.9812
14	0.9864	1.0402	0.9860	0.9857	0.9835	0.9813
16	0.9864	1.0398	0.9861	0.9859	0.9837	0.9815
18	0.9864	1.0393	0.9862	0.9860	0.9839	0.9817
20	0.9864	1.0388	0.9863	0.9862	0.9841	0.9819

Note that, the CG location of L7 is kept constant since the NUT is only moving up and down. The corresponding reaction forces and moments can be calculated using Eqs. (25) to (33) in a similar manner, shown Tab. 13 and 14.

Table 13: Centrifugal and reaction forces on ACT manual setup version on anhedral and tip

$\delta$ [deg]	$F_{ANH,CG}$ [N]	$M_{ANH,CG}$ [Nm]	$F_{TIP,CG}$ [N]	$M_{TIP,CG}$ [Nm]	$F_{TIP,rea}$ [N]
0	418.29	1.04	163.23	0.41	270.65
2	418.29	0.24	163.24	0.41	122.96
4	418.29	-0.56	163.26	0.42	-26.00
6	418.29	-1.36	163.27	0.42	-176.61
8	418.29	-2.15	163.29	0.43	-329.26
10	418.29	-2.95	163.30	0.43	-484.38
12	418.29	-3.74	163.32	0.43	-642.42
14	418.29	-4.53	163.34	0.44	-803.86
16	418.29	-5.31	163.35	0.44	-969.21
18	418.29	-6.09	163.37	0.44	-1139.04
20	418.29	-6.86	163.38	0.44	-1313.97

Table 14: Centrifugal and reaction forces on ACT manual setup version on link and counter-weight

$\delta$ [deg]	$F_{LINK,CG}$ [N]	$F_{LINK,rea}$ [N]	$F_{CW,CG}$ [N]	$F_{CW,rea}$ [N]	$F_{RESULT}$ [N]
0	24.47	235.76	80.27	316.02	316.02
2	24.48	120.46	80.28	200.74	200.74
4	24.48	4.18	80.29	84.48	84.48
6	24.48	-113.38	80.31	-33.07	-33.07
8	24.49	-232.55	80.32	-152.22	-152.22
10	24.49	-353.64	80.34	-273.30	-273.30
12	24.50	-477.01	80.35	-396.65	-396.65
14	24.50	-603.03	80.37	-522.66	-522.66
16	24.51	-732.10	80.38	-651.72	-651.72
18	24.51	-864.68	80.40	-784.28	-784.28
20	24.52	-1001.22	80.42	-920.81	-920.81

Here, the torque required to turn the screw in order to deflect the blade tip is not needed since an operator will manually control the deflection. Fig. 34 shows the resultant axial force acting on the screw with angle of deflection.

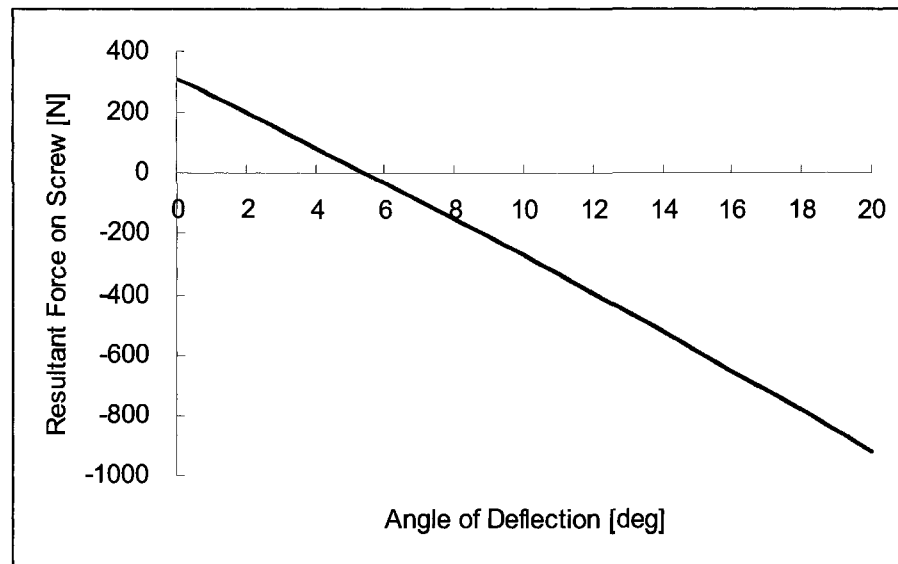


Figure 34: Force required to deflect the blade tip.

## 2.5 Full-Scale Feasibility Study

SHARCS currently concerns a small-scaled rotor with three actively controlled sub-systems integrated into one single blade. However, a full scale feasibility study has been performed for the BO-105 rotor blade. Many researchers like NASA, US Army, and Eurocopter used BO-105 rotor blade characteristics for their experiments. Tab. 15 presents the characteristics of the BO-105 rotor blade applied for the SHARCS full-scale study. The BO-105 rotor blade has similar aeroelastic, aeroacoustic, and Lock number characteristics of the small-scaled SHARCS blade.

Table 15: BO-105 rotor blade characteristic for the SHARCS full scale study (Yu, 2002)

<b>Parameters</b>	<b>Values</b>
Rotor Radius	4 m
Rotor Solidity	0.093
Chord Length	0.300 m
Airfoil	NACA23012
Mach Number	0.55
Blade Tip Speed	182.30 m/s
Angular Velocity, $\omega$	44.6 m/s
RPM	426
Mass of 4 meter Blade	10.16 Kg

It was assumed that the BO-105 rotor blade is made of composite materials, with a density of  $1750 \text{ kg/m}^3$ . To minimize the complexity of the problem, the blade was assumed to have a rectangular planform with the mass uniformly distributed along the span. Therefore, the mass of the blade tip (last 10% of the blade), is calculated at 1.2 kg. However, since the rotor blade becomes more tapered towards the tip, the final blade tip mass is assumed to be only half of the above mass at 600 grams.

The blade features a NACA23012 airfoil (thickness is 12%). Hence the thickness of the full scale blade is found to be 36 mm.

### **2.5.1 The Counter-Weight Sizing**

The hinge moment from the full scale blade tip can be calculated in a similar manner to the small scaled blade. Using Fig. 13, but with the blade tip length of 400

mm and the centre of gravity in the middle of the tip section, Fig. 35 is drawn:

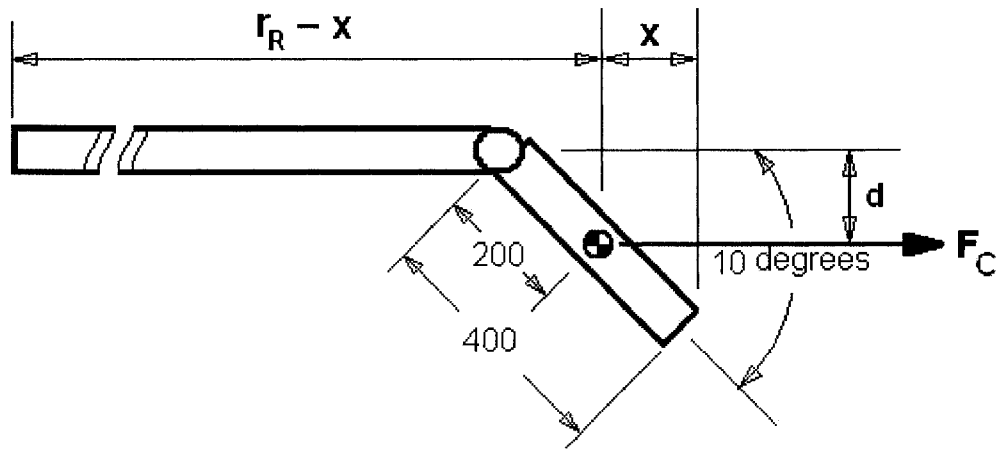


Figure 35: Full-scale blade tip sketch.

The hinge moment can be calculated in the same manner as in Tab. 15. This gives the centrifugal load acting on the blade tip of 4985 N. Furthermore, a hinge moment from the centrifugal load at its maximum tip velocity at 10 degree deflection is evaluated at 173.13 Nm. Compared to the small-scaled system, the centrifugal hinge moment is about 41 times larger for the full-scale than for the small-scaled. But since the full scale rotor blade thickness is larger than the sub-scaled system, there is more space available to fit a larger ACT actuator system. Therefore, the hinge moment may be resolved in a similar manner as for the small-scaled SHARCS system.

For the aerodynamic loads, the same procedures were followed from the small scaled SHARCS design. Since the full-scale should have the same similarities, the blade tip speed was kept the same (178.47 m/s). So the RPM for the full-scale study is found to be 426 RPM. Fig. 36 and 37 present the full-scale aerodynamic

distribution and effective angle of attack for various thrust coefficients. If the effective angle goes beyond 15 degrees, stall will occur. So, the blade designer must choose a thrust coefficient value which will satisfy this condition.

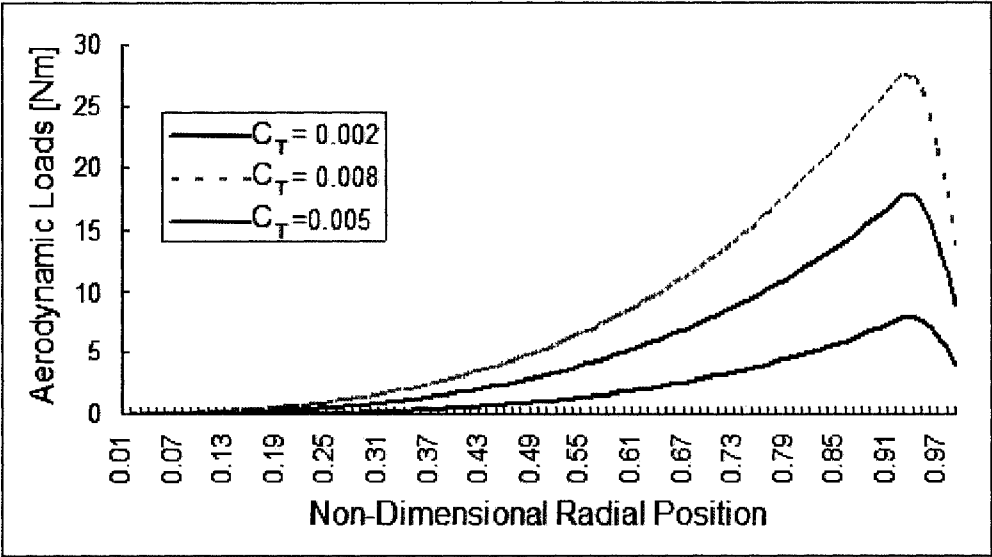


Figure 36: Aerodynamic loads distribution for full-scale study.

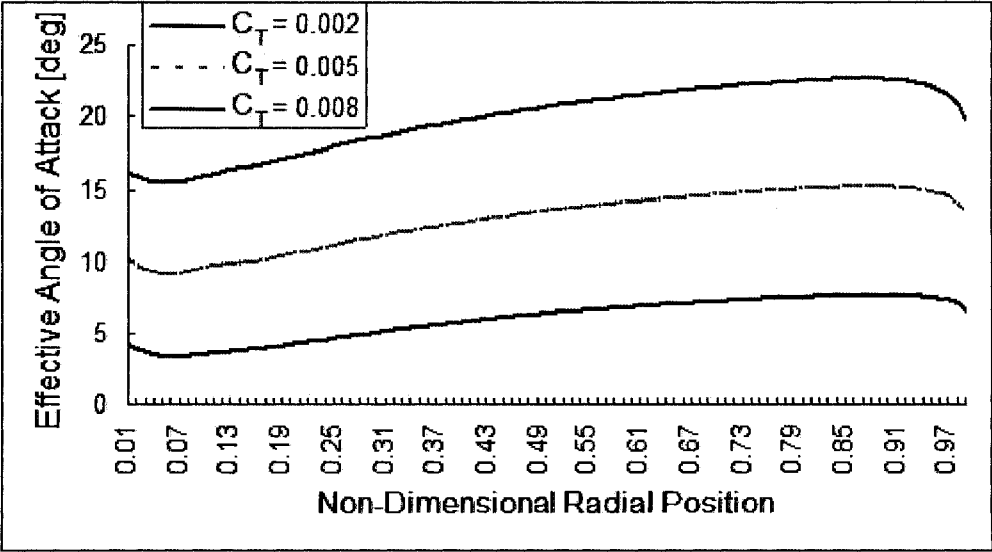


Figure 37: Effective angle of attack for full-scale study.

The aerodynamic load at 90% radius is found to be 16.1 Nm using a thrust coefficient of 0.005. This is about 2.2 times greater than the small-scale SHARCS

blade. The reason is because the RPM of the rotor is much lower for the full-scale than the small-scale.

## 2.5.2 Motor Requirements

The full scale ACT system has been designed again to minimize the torque required to deflect the blade tip. The masses and sizes of the ACT components were carefully optimized and the final torque was found using the same equations (Eqs. (25) to (33) from section 2.4.1) as for the small-scaled model. Tab. 16, 17, and 18 present the centrifugal forces, reaction forces, and moments on ACT components due to the centrifugal acceleration and the final torque required for the full scale ACT to overcome the resultant loads with a safety factor of 1.5.

Table 16: Centrifugal and reaction forces on full scale ACT on anhedral and tip

$\delta$ [deg]	$F_{ANH,CG}$ [N]	$M_{ANH,CG}$ [Nm]	$F_{TIP,CG}$ [N]	$M_{TIP,CG}$ [Nm]	$F_{TIP,red}$ [N]
0	18942.27	283.39	3246.42	57.87	7665.73
2	18942.97	151.38	3246.67	62.89	4573.30
4	18942.46	19.18	3246.93	67.83	1770.96
6	18940.73	-113.04	3247.21	72.69	-785.76
8	18937.78	-245.08	3247.51	77.47	-3132.76
10	18933.63	-376.75	3247.82	82.15	-5299.36
12	18928.28	-507.88	3248.15	86.73	-7309.75
14	18921.73	-638.27	3248.49	91.21	-9184.07
16	18913.99	-767.75	3248.85	95.58	-10939.25
18	18905.07	-896.13	3249.22	99.83	-12589.62
20	18894.98	-1023.23	3249.60	103.97	-14147.44

Table 17: Centrifugal and reaction forces on full scale ACT on link and counter-weight

$\delta$ [deg]	$F_{LINK,CG}[N]$	$F_{LINK,rea}[N]$	$F_{CW,CG}[N]$	$F_{CW,rea}[N]$	$F_{RESULT}[N]$
0	1485.71	9151.44	1755.24	10906.67	10906.67
2	1485.94	6059.23	1755.51	7814.75	7814.75
4	1486.19	3257.14	1755.81	5012.95	5012.95
6	1486.45	700.68	1756.12	2456.80	2456.80
8	1486.72	-1646.04	1756.45	110.41	110.41
10	1487.01	-3812.35	1756.80	-2055.55	-2055.55
12	1487.32	-5822.43	1757.16	-4065.27	-4065.27
14	1487.64	-7696.43	1757.54	-5938.89	-5938.89
16	1487.97	-9451.28	1757.94	-7693.34	-7693.34
18	1488.31	-11101.31	1758.35	-9342.97	-9342.97
20	1488.67	-12658.77	1757.78	-10900.00	-10900.00

Table 18: Torque required for the full scale ACT to overcome resultant loads

$\delta$ [deg]	$T[Nm]$	$T_C[Nm]$	$T_{RESULT}[Nm]$	$T_{SF}[Nm]$
0	27.61	14.18	41.79	62.68
2	19.78	10.16	29.94	44.91
4	12.69	6.52	19.21	28.81
6	6.22	3.19	9.41	14.12
8	0.28	0.14	0.42	0.63
10	-5.20	-2.67	-7.88	-11.81
12	-10.29	-5.28	-15.58	-23.36
14	-15.03	-7.72	-22.75	-34.13
16	-19.47	-10.00	-29.48	-44.21
18	-23.65	-12.25	-35.80	-53.69
20	-27.59	-14.17	-41.76	-62.64

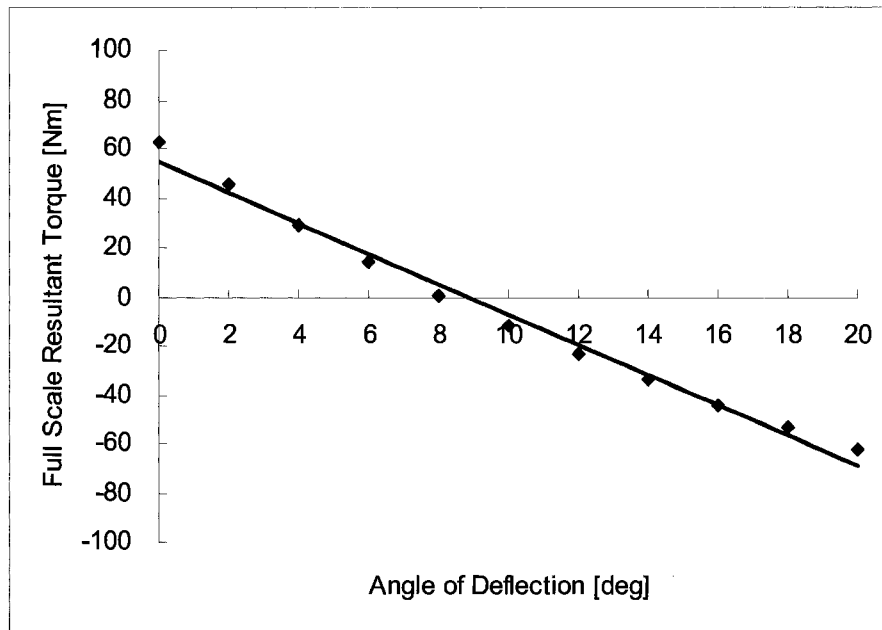


Figure 38: Torque versus angle of deflection for full-scale ACT.

As in the case of the full-scaled ACT, the torque is not balanced exactly at 10 degree deflection but around at 8 degrees. The full scale ACT actuator system would have to provide a torque of 55 Nm at 0 degree and -55 Nm at 20 degrees deflection.

### 2.5.3 Motor Selection

Intensive research was done to find a suitable actuator for the full-scale ACT system. The size of the motor is dictated by the required torque (Ritchie, 2003). Just like the small-scaled ACT system, it was not a simple task to find a motor which would fit inside an airfoil thickness of 36 mm. Hence, the design solution adopted for the small-scaled blade must be adopted, i.e. applying a motor and gearhead at the root, positioned perpendicular to the radial direction. The motor and the gearhead were

chosen from Applied Motion for the full scale ACT system. Tab. 19 and 20 show the characteristics of the motor and the gearhead.

Table 19: Maxon RE 75 DC motor additional characteristics

<b>Category</b>	<b>Model</b>	<b>RE 75 DC Motor 118822</b>
Power (W)		250
Continuous Torque (mNm)		718
Max Axial Load (N)		70
Max Radial Load (N)		350
Diameter (mm)		75
Length (mm)		210.5
Weight (kg)		2.8

Table 20: Maxon GP 81 gearhead additional characteristics

<b>Category</b>	<b>Model</b>	<b>Maxon Motor GP 81 Gearhead 110411</b>
Gear Reduction Ratio		51:1
Max Continuous Torque (Nm)		120
Max Efficiency (%)		70
Max Axial Load (N)		200
Max Radial Load (N)		1000
Diameter (mm)		81
Length (mm)		127.3
Weight (kg)		3

Other possible actuation concepts such as hydraulic rotary motors, and pneumatic systems were also searched but just like for the small-scaled system, the sizes of the actuators were too large to fit into the full scale rotor blade. The output torque from the gearhead, 120 Nm, could handle the required torque. The tip would deflect from 0 to 20 degrees in about 6 seconds. The total mass of the ACT system

(motor and gearhead) would be about 5.8 kg, which is about 60% of the original blade mass. However, the length is this time shorter than the chord length so the alteration of the root transition is not substantial as for the small-scale one.

**2.5.4 Overall Assembly**

The ACT for the full-scale rotor blade will be designed in a similar manner of the small-scaled. Tab. 21 presents the mass of the full-scale ACT system and the materials employed.

Table 21: Final mass of full-scaled ACT system

<b>Part Name</b>	<b>Mass (grams)</b>	<b>Material</b>
m_CW	60.5	Titanium
m_TIP	109	Titanium
m_LINK	25.3	Titanium
Horseshoe	577.7	Titanium
m_ANH	600	Composite

The ACT components are all made from titanium to minimize the weight of the ACT system. Also from Tab. 22 which compares the full-scale and the small-scale ACT system, shows that the full-scale ACT is much more feasible than the small-scale.

Table 22: Comparison between full-scaled and small-scale ACT system

<b>Category \ Model</b>	<b>Full-scale</b>	<b>Small-scale</b>
Output Torque (Nm)	120	6
Diameter (mm)	81	32
Airfoil Thickness (mm)	36	12
Blade Mass (kg)	22	0.446
Actuator and Motor Mass (kg)	5.8	0.496

As can be seen, the weight penalty of the ACT is only 26% of the blade mass for the full-scale configuration, whereas it is 111% for the small-scale one. Thus, the proposed design concept seems to be more feasible in full-scale than small-scale.

### **3. POSITION ACCURACY CONTROL**

Since the ACT mechanism system uses an electric motor and gears combined with a long torque rod, it is necessary to review the system dynamics of the entire assembly. The torque rod connecting the blade root to the blade tip, will cause large twist on the rod which may cause a time delay in the system. Also, since the ACT actuator mechanism located at the tip is operating under high centrifugal acceleration, the control of the ACT system requires a better understanding of the principles of the ACT system dynamics. The analysis of the position accuracy control is made for the small-scale blade only and it is not an active control. This is a static control simulation only since the ACT will only be activated in certain flight regimes by the pilot; it will be set to deflection angle and stay there until switched off.

#### **3.1 System Equations of Electric Motor**

The electric motor can be represented as an electric circuit (see Fig. 39). From the electric circuit diagram of the electric motor, equations of system dynamics can be found using Newton's Law and Kirchoff's Law (Eq. 43 and 44).

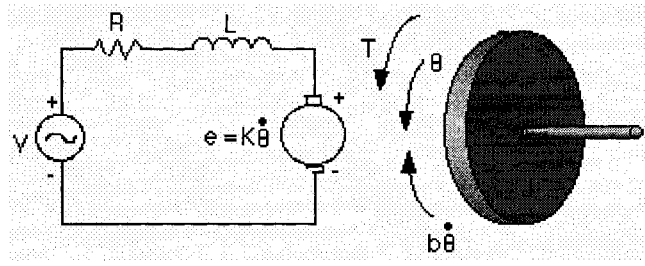


Figure 39: Electric circuit diagram of electric motor  
(Carnegie Mellon University, 2007).

$$J_m \frac{d^2 \theta_m}{dt^2} + b_m \frac{d\theta_m}{dt} = T_m \quad (43)$$

$$L \frac{di}{dt} + Ri = V - e \quad (44)$$

Here  $J_m$  is the moment of inertia of the rotor,  $b_m$  is the damping constant of the mechanical system,  $T_m$  is the motor torque,  $\theta_m$  is the position of the motorshaft,  $L$  is the electric inductance,  $R$  is the electric resistance,  $V$  is the input supply voltage,  $e$  is the back electromotive force (EMF) of the motor,  $i$  is the current, and  $t$  is the time. For simplicity, the rotor, rotorshaft and motorshaft are assumed to be rigid. The motor torque,  $T_m$  and the back EMF,  $e$  equations are given as follows.

$$T_m = K_t i \quad (45)$$

$$e = K_e \dot{\theta}_m \quad (46)$$

where  $K_t$  is the torque constant and  $K_e$  is the back EMF constant. Substituting Eqs.

(45) and (46) into (43) and (44) gives:

$$J_m \frac{d^2 \theta_m}{dt^2} + b_m \frac{d\theta_m}{dt} = K_t i \quad (47)$$

$$L \frac{di}{dt} + Ri = V - K_e \dot{\theta}_m \quad (48)$$

Laplace transformation is performed to simplify the analysis and to minimize

mathematical complexities. Thus, taking the Laplace transformations of Eqs. (47) and (48) gives the following:

$$s(J_m s + b_m)\theta_m(s) = K_t I(s) \quad (49)$$

$$(Ls + R)I(s) = V(s) - K_e s\theta_m(s) \quad (50)$$

where “ $s$ ” represents the function in the frequency domain. Substituting  $I(s)$  from Eqs. (50) to (49) gives:

$$s(J_m s + b_m)\theta_m(s) = K_t \left[ \frac{V(s) - K_e s\theta_m(s)}{Ls + R} \right] \quad (51)$$

Simplifying Eq. (51) further, a transfer function from the input voltage to the resulting angular position change output is obtained:

$$G(s) = \frac{\theta_m(s)}{V(s)} = \frac{K_t}{s\{(J_m s + b_m)(Ls + R) + K_t K_e\}} \quad (52)$$

Also, the transfer function from the input voltage to the resulting speed change output can be found as the following.

$$G(s) = \frac{\dot{\theta}_m(s)}{V(s)} = \frac{\omega_m(s)}{V(s)} = \frac{K_t}{(J_m s + b_m)(Ls + R) + K_t K_e} \quad (53)$$

Where  $\omega_m(s)$  is the angular velocity in the frequency domain. In the above transfer function, the energy dissipation elements are the electric resistance,  $R$  the damping constant of the mechanical system,  $b_m$ , while the energy storage elements are the moment of inertia of rotor,  $J_m$ , the electric inductance,  $L$  and the magnetic coupling,  $K_t$  and  $K_e$  in this system equation for the electric motor. For the

concrete case of the SHARCS small-scale model, the RE 30 motor characteristics from Maxon Motor Company were shown in Tab. 9 in section 2.4.

Rewriting the system equation of the electric motor, Eq. (53), allows one to construct a block diagram of a typical feedback control system:

$$G(s) = \frac{H(s)}{1 + K_e H(s)} \quad (54)$$

Here,  $H(s) = \left(\frac{1}{Ls + R}\right) K_t \left(\frac{1}{J_m s + b_m}\right)$ . Therefore the block diagram of the electric

motor can be illustrated as:

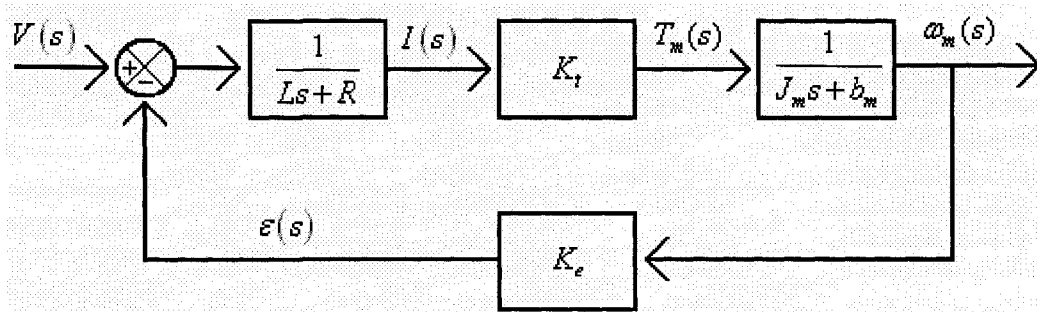


Figure 40: Block Diagram of Electric Motor.

This block diagram explains how the electric motor is working step-by-step. When a voltage,  $V(s)$  is applied to the electric motor, it is converted into current,  $I(s)$ . However, unless the inductance,  $L$  is equal to zero, there will be no immediate rise in the current due to the magnetic inertia of the coil which means that the initial rise time delay is dominated by the inductance. As the current builds up inside the electric motor, the current converts into a torque,  $T_m(s)$  due to the moving charges,

which surround the coil inside the motor (Miu, 1992). Similarly, unless mechanical inertia of the rotor,  $J_m$  is equal to zero, there will not be an immediate response in velocity,  $\omega_m(s)$ . The back emf,  $\varepsilon(s)$  will be generated by the magnetic field to counteract the reduction in magnetic flux as the velocity increases (Miu, 1992).

### 3.1.1 MatLAB Simulation of Motor Position

For the position control of the electric motor, few design requirements were set to guide the MatLAB simulation

- 1 rad/s with step reference.
- Settling time less than 0.2 seconds
- Overshoot less than 10%
- No steady-state error
- No steady-state error due to disturbance

The above design criterions are common in control systems. Most of the time the designer requirements depend on the control system process. So, the requirements here were chosen based on the SHARCS operation.

Using MatLAB, a transfer function of Eq. (53) was coded. The open-loop response was first examined to check whether or not the system was stable and if the system would fit into the design criteria. Fig. 41 shows the open-loop response of the

motor's transfer function.

With the values given using Tab. 8, the following transfer function was found:

which is the closed-loop transfer function of the motor's angular velocity.

$$\frac{\dot{\theta}(s)}{V(s)} = \frac{0.0538}{1.77 \times 10^{-8} s^2 + 8.753 \times 10^{-5} s + 3.2 \times 10^{-3}} \quad (55)$$

Therefore, to get an angular position of the system, a step input has been applied to Eq.

(55) to obtain Fig. 41.

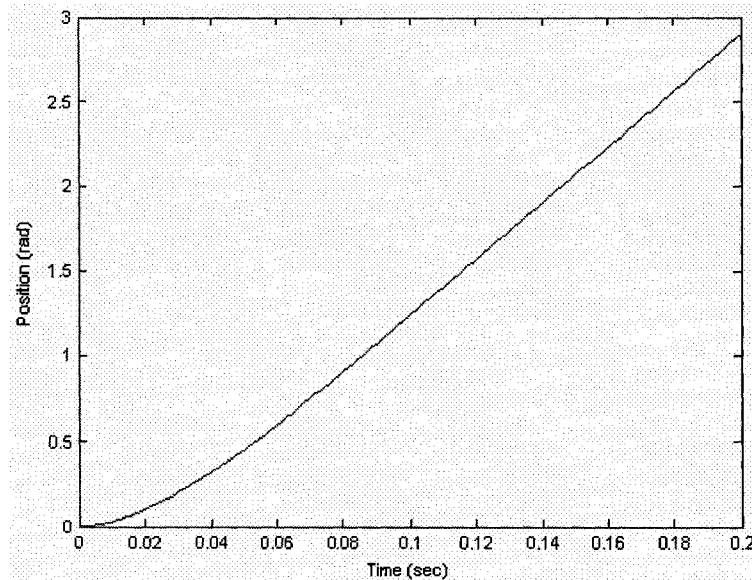


Figure 41: Step response of electric motor for the open-loop system.

From the plot of an open-loop system, if 1 Volt is applied to the system, the motor's angular position would change about 2.8 rad. This is 2.8 times greater than the desired angular position since the requirement set previously was to turn the motor only 1 rad per 1 Volt step input to the system. Therefore, the original motor's characteristic transfer function needs a position controller.

### 3.1.2 Electric Motor Controller

Controllers of proportional, integral, and derivative (PID) type are studied next. The transfer function of the PID controller is given as,

$$K_p + \frac{K_I}{s} + K_D s = \frac{K_D s^2 + K_p s + K_I}{s} \quad (56)$$

Instead of applying all PID values simultaneously, the proportional controller was first chosen. The proportional controller was found by trial-and-error in a closed-loop system of the electric motor transfer function. Fig 42 and 43 show the motor response to a step input and a step disturbance of  $K_p = 1.5$  for a closed-loop system. The step input is the actual response of the motor and the step disturbance allows to assess the steady-state error of the motor with a disturbance signal.

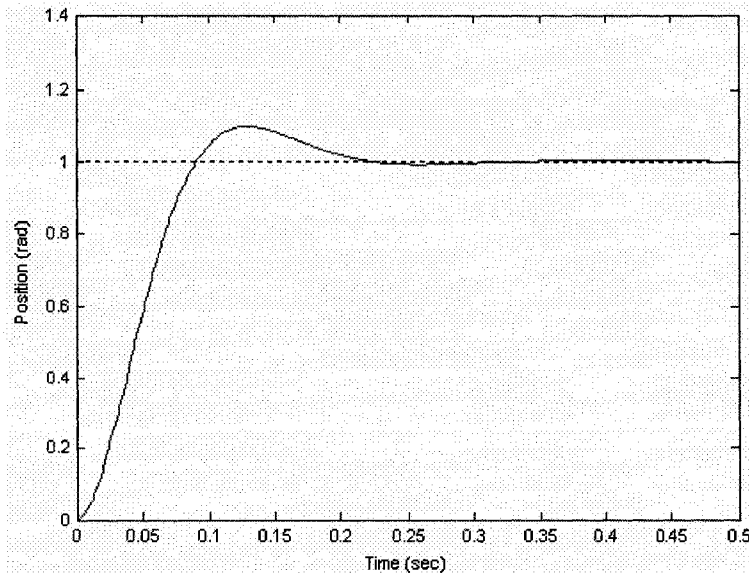


Figure 42: Motor response to a step input of  $K_p = 1.5$  for a closed-loop system.

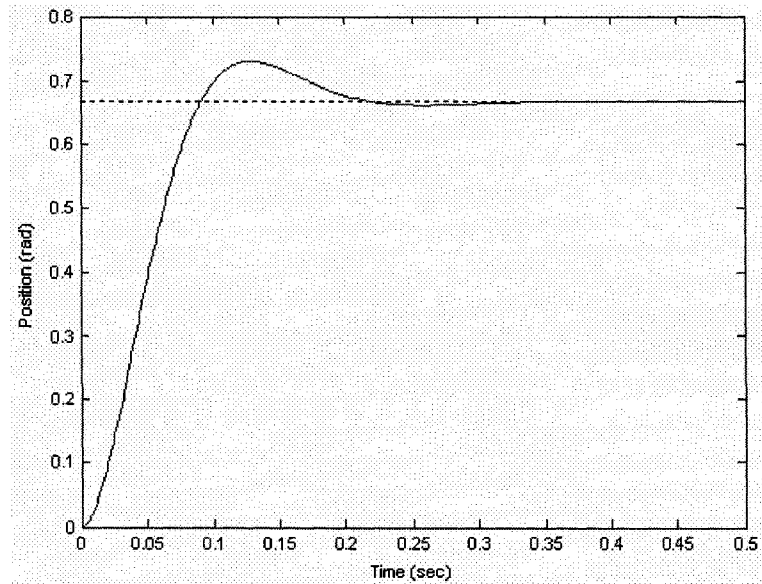


Figure 43: Motor response to a step disturbance of  $K_p = 1.5$  for a closed-loop system.

A proportional controller reduced the rise time and somewhat decreased the steady-state error but did not shorten the settling time and decreased the overshoot of the system. Therefore, to decrease the steady-state error of the system, an integral controller is needed. Fig. 44 and 45 show the Proportional-Integral (PI) controller added to the system and its effects.

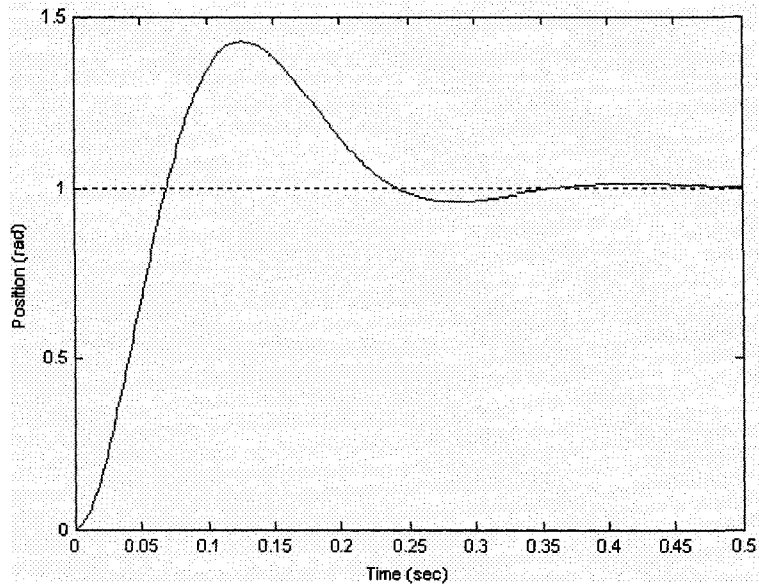


Figure 44: Motor response to a step input of  $K_p = 1.5$  and  $K_i = 13$  for closed-loop system.

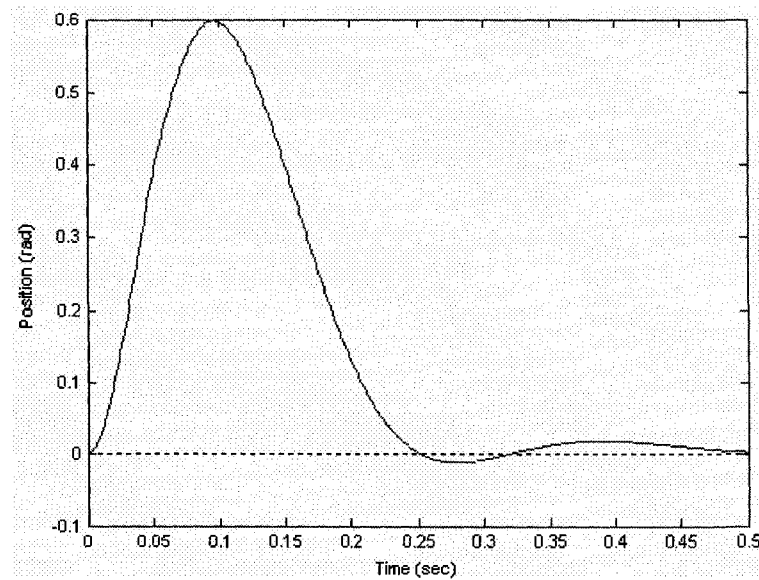


Figure 45: Motor response to a step disturbance of  $K_p = 1.5$  and  $K_i = 13$  for closed-loop system.

As can be seen from Fig. 45, the integral controller reduces the steady-state error significantly in a step disturbance compared to Fig. 43 where the steady-state error is present. To speed up the response of the system, both proportional and integral gains were multiplied 10 times its original values to check how this would affect the

system. These results are illustrated in Figs. 46 and 47.

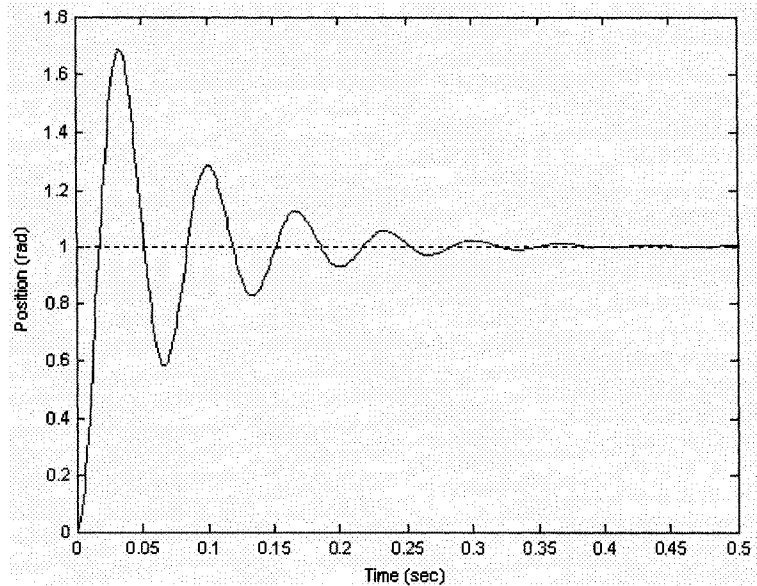


Figure 46: Closed-loop response of step input with  $K_p = 15$  and  $K_i = 130$ .

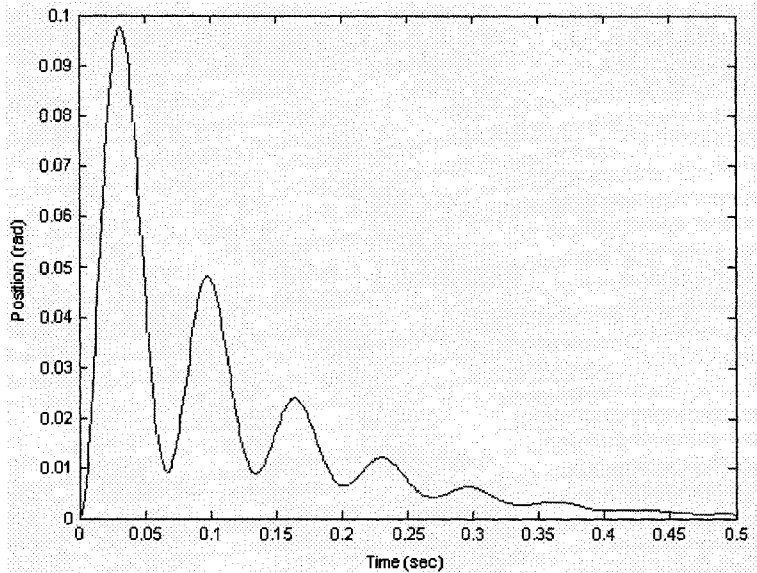


Figure 47: Closed-loop response of step disturbance with  $K_p = 15$  and  $K_i = 130$ .

As one can see, by increasing both PI controller gain magnitudes by one order of magnitude, the response of the system is now faster but the transient response region got worse as the overshoot became too high (about 1.7, which is equivalent to

70% overshoot). Therefore, a derivative controller, which has the effect of increasing the damping of the system, is added to reduce the overshoot, and to improve the transient response (Figs. 48 and 49).

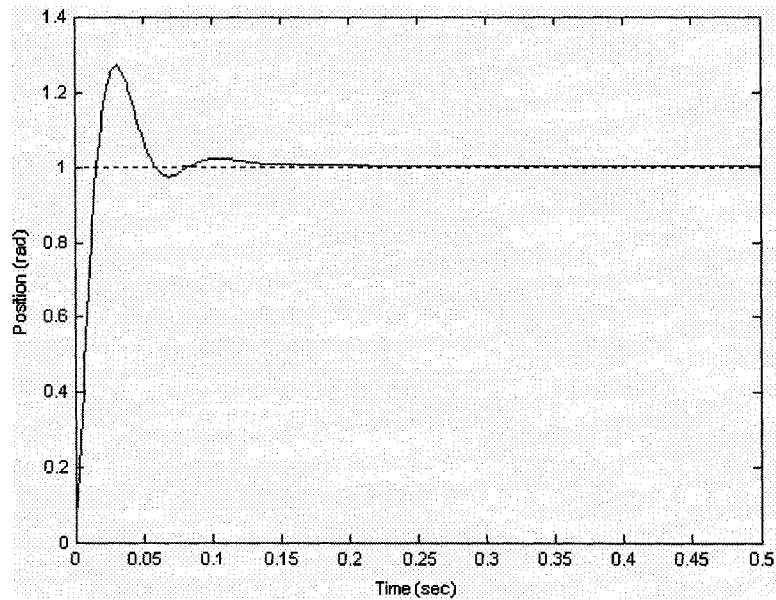


Figure 48: Closed-loop response of step input with  $K_p = 15$ ,  $K_I = 130$  and  $K_d = 0.1$ .

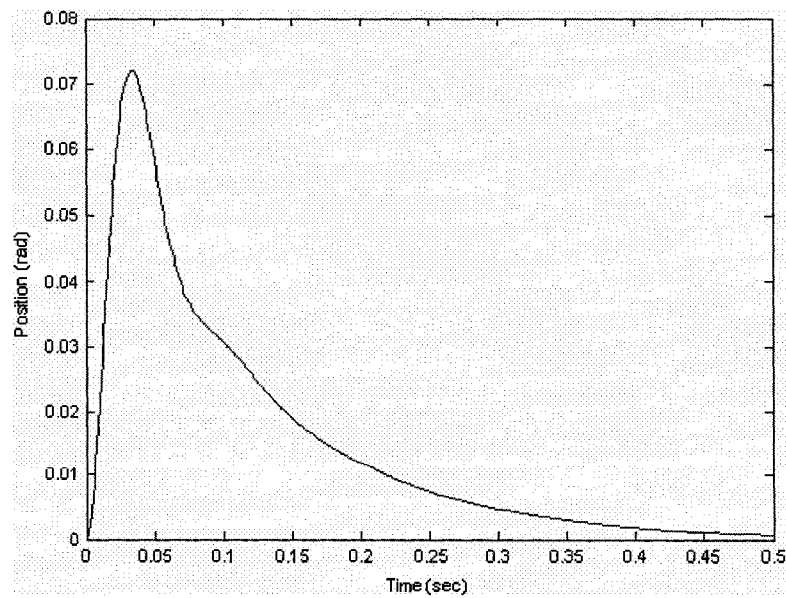


Figure 49: Closed-loop response of step disturbance with  $K_p = 15$ ,  $K_I = 130$  and  $K_d = 0.1$ .

The step input response using all three controllers looks very good, having less than about 10% overshoot, settling time of 0.2 seconds, and almost zero steady-state error. But the step disturbance response is still slow. By increasing the integral gain, the disturbance response speeds up. Trial-and-error approach on other parameters of the control system gives an optimum response. This is illustrated in Figs. 50 and 51.

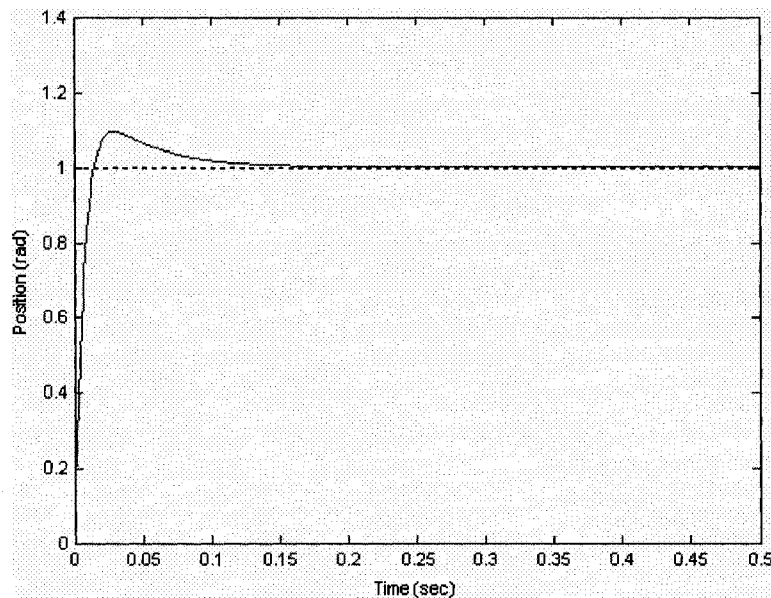


Figure 50: Closed-loop response of step input with  $K_p = 15$ ,  $K_I = 200$  and  $K_d = 0.25$ .

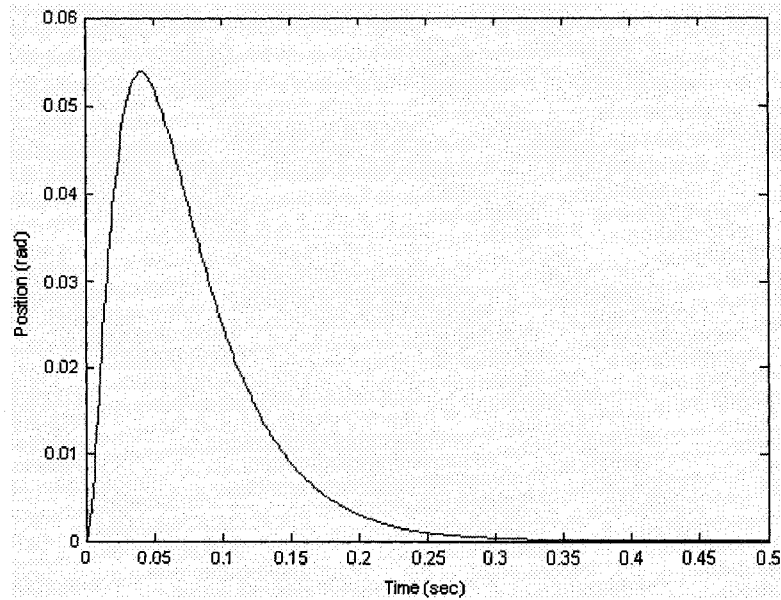


Figure 51: Closed-loop response of step disturbance with  $K_p = 15$ ,  $K_I = 200$  and  $K_d = 0.25$ .

By increasing the integral gain, the step input and the step disturbance response is stable. Therefore, the proportional-integral-derivative (PID) controller with  $K_p = 15$ ,  $K_I = 200$  and  $K_d = 0.25$  satisfies the design requirements.

### 3.2 System Equations of Gearhead Mechanism

Considering the system equations of the gearhead is important since the electric motor is connected with the gearhead to deflect the blade tip. Therefore, simulating only the dynamics of the electric motor will not help to fully understand the ACT actuator system. The gears are used to reduce the speed and to magnify the torque. For simplicity, the stiffness of the shafts of the gearhead is assumed to be rigid. The GP 32C gearhead was assumed to be as simple as possible (like in Fig. 52) since

the gearhead was not opened to check the number of gear teeth, number of gears, and the gear layout. Fig. 52 shows a simple schematic diagram of the gearheads in series combination.

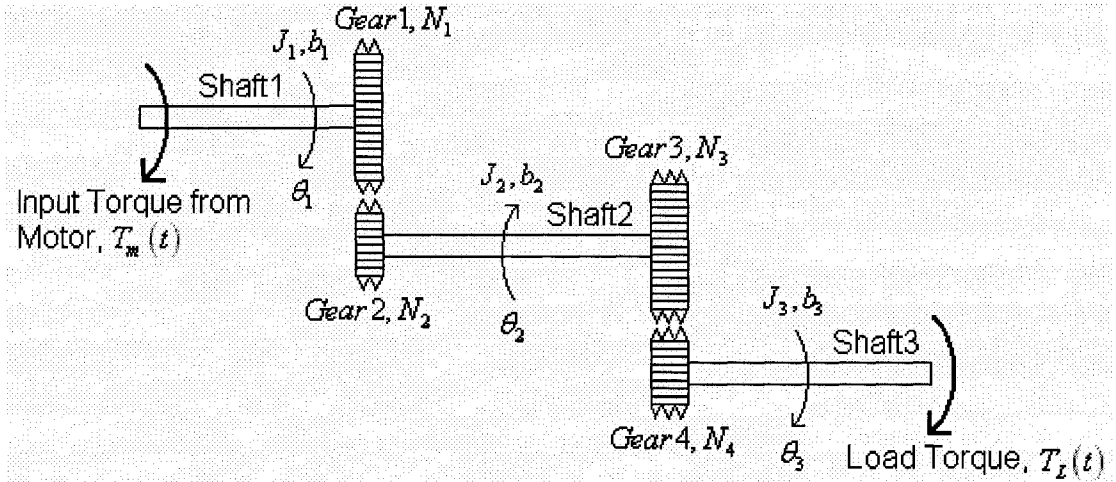


Figure 52: Schematic diagram of the gearhead.

The number of teeth on gear 1, 2, 3, 4 were denoted as  $N_1, N_2, N_3, N_4$ , respectively, and the angular displacements of shaft 1, 2, 3 as  $\theta_1, \theta_2, \theta_3$ . To reduce the complexity of the unknown variables and minimize the errors, the gearhead was represented as one single “black box” as shown in Fig. 52.

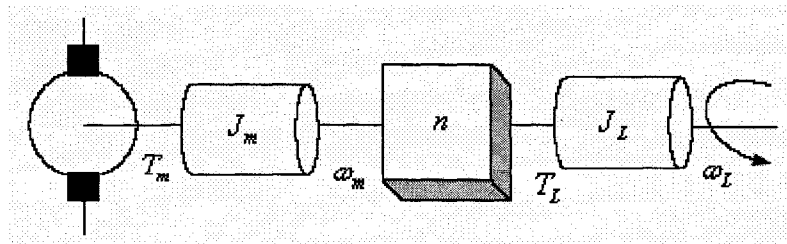


Figure 53: Schematic diagram of motor with a gearhead (Becerra, 2003).

Here,  $T_m$  is the torque developed by the electric motor,  $J_m$  is the moment

of inertia of the motor,  $\omega_m$  is the angular velocity produced by the motor,  $n$  is the gear reduction ratio,  $T_L$  is the output torque of the load due to the gearhead,  $J_L$  is the moment inertia of the load, and  $\omega_L$  is the angular velocity of the load. The torque output of the gearhead is given as:

$$T_L = nT_m = nK_t i \quad (56)$$

Also, due to the gearhead reduction ratio, the relationship between the angular velocity of the motorshaft and the angular velocity of the gearshaft is given by:

$$\omega_L = \frac{\omega_m}{n} \quad (57)$$

As the gearhead data were given by the Maxon Motor Company (Tab. 10), a new transfer function, including a system equation of the gearhead mechanism can be derived.

### 3.3 System Equations of ACT

Using Kirchoff's Law and Newton's Law, the new system equations for the entire ACT, electric motor and gearhead system, could be found. The angular velocity of the motorshaft was substituted with the angular velocity of the gearshaft relationship equation and thus Eqs. (47) and (48) will re-written:

$$J_m \frac{d^2\theta_m}{dt^2} + b_m \frac{d\theta_m}{dt} + \frac{J_L}{n} \frac{d^2\theta_L}{dt^2} = K_t i \quad (58)$$

$$L \frac{di}{dt} + Ri = V - K_e n \frac{d\theta_L}{dt} \quad (59)$$

Substituting Eq. 58 into 56 gives:

$$T_L = n \left[ nJ_m \frac{d^2\theta_L}{dt^2} + nb_m \frac{d\theta_L}{dt} + \frac{J_L}{n} \frac{d^2\theta_L}{dt^2} \right] \quad (60)$$

Taking a Laplace Transform of Eqs. (59) and (60) leads to:

$$(Ls + R)I(s)i = V(s) - K_e n s \theta(s) \quad (61)$$

$$T_L = (n^2 J_m s^2 + n^2 b_m s + J_L s^2) \theta_L(s) \quad (62)$$

Thus, substituting Eqs. (61) and (62) into (56) gives:

$$(n^2 J_m s^2 + n^2 b_m s + J_L s^2) \theta_L(s) = nK_t \left( \frac{V(s) - K_e n s \theta(s)}{Ls + R} \right) \quad (63)$$

Rearranging Eq. (63) in terms of the angular velocity of the load per input voltage gives:

$$\frac{\dot{\theta}_L(s)}{V(s)} = \frac{\omega_L(s)}{V(s)} = \frac{nK_t}{s \left\{ s(n^2 J_m + J_L) + n^2 b_m \right\} (Ls + R) + n^2 K_t K_e} \quad (69)$$

And finally, the transfer function of input voltage to resulting angular position change output of the load can be obtained as:

$$\frac{\theta_L(s)}{V(s)} = \frac{nK_t}{s \left[ \left\{ s(n^2 J_m + J_L) + n^2 b_m \right\} (Ls + R) + n^2 K_t K_e \right]} \quad (70)$$

### 3.4 MatLAB Simulation of the Position Control

With the numerical values given from the Maxon Motor Company, Eq. (70)

can be re-written as the following:

$$\frac{\dot{\theta}(s)}{V(s)} = \frac{5.541}{1.878 \times 10^{-4} s^2 + 0.9286s + 33.95} \quad (71)$$

Similarly to the motor simulations alone, the design criteria for the combined motor and gearhead system were defined as:

- 1 rad/s with step reference.
- Settling time less than 0.2 seconds
- Overshoot less than 10%
- No steady-state error
- No steady-state error due to disturbance

Fig. 54 shows the electric motor and the gearhead's open-loop system response for a step input.

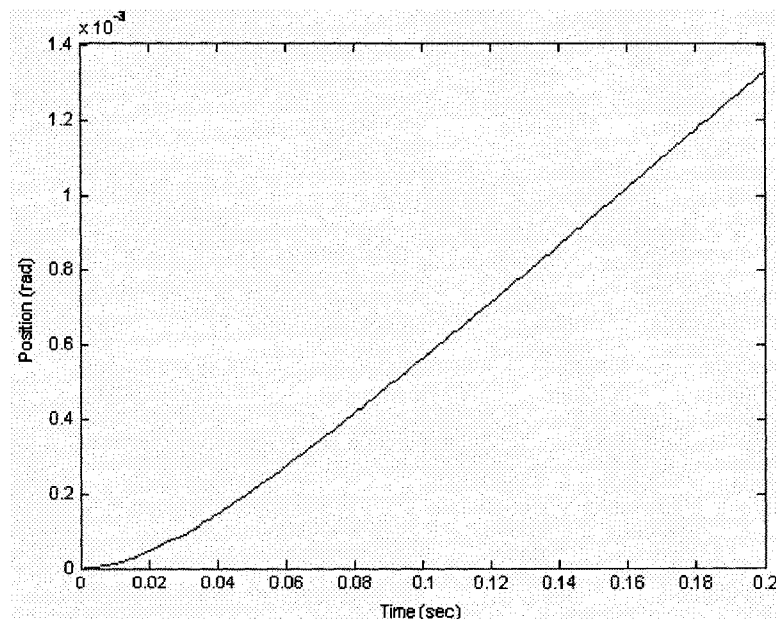


Figure 54: Step response of electric motor and gearhead for the open-loop system.

As can be seen, the input voltage of one gives about  $1.3 \times 10^{-3}$  rad, which means 1

Volt makes the gearhead shaft to turn  $1.3 \times 10^{-3}$  rad. Since this output does not satisfy

the design criteria, which is one radian per second, a controller is required. With a proportional controller, the rise time can be decreased as well as the steady-state error.

Figs. 55 and 56 show the motor response to a step input and a step disturbance of  $K_p = 2,000$  for a closed-loop system, respectively.

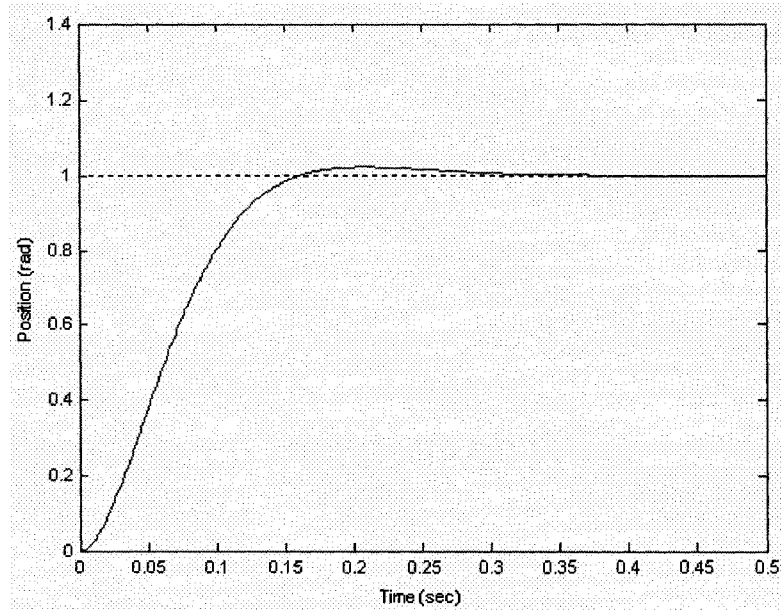


Figure 55: Closed-loop response of step input with  $K_p = 2,000$ .

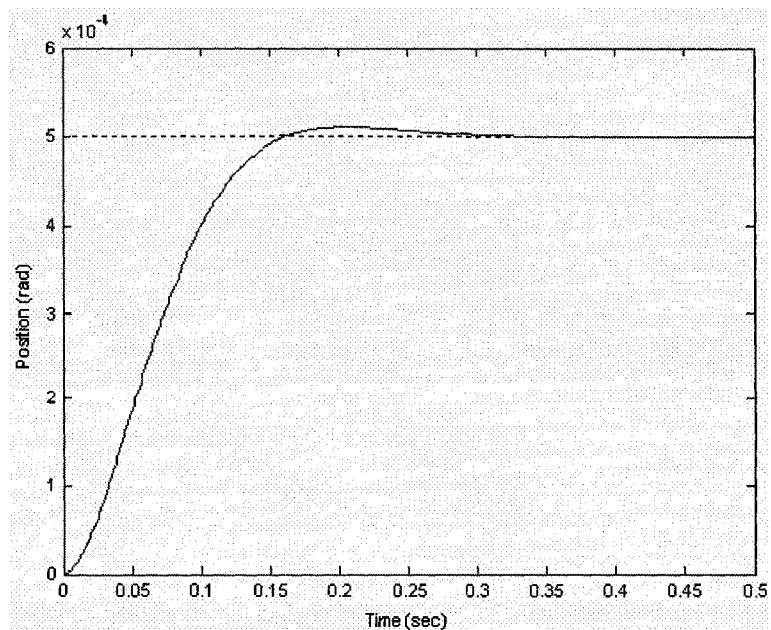


Figure 56: Closed-loop response of step disturbance with  $K_p = 2,000$ .

A proportional controller did reduce the rise time but the settling time is still too long. However, the proportional controller did not affect the steady-state error as expected. Thus, although the steady-state error to a step disturbance is small, in the order of  $10^{-4}$ , it is still not satisfactory. The steady-state error can be driven to zero by adding the integral controller. Fig. 57 and 58 show the PI controller added to the system and its effects.

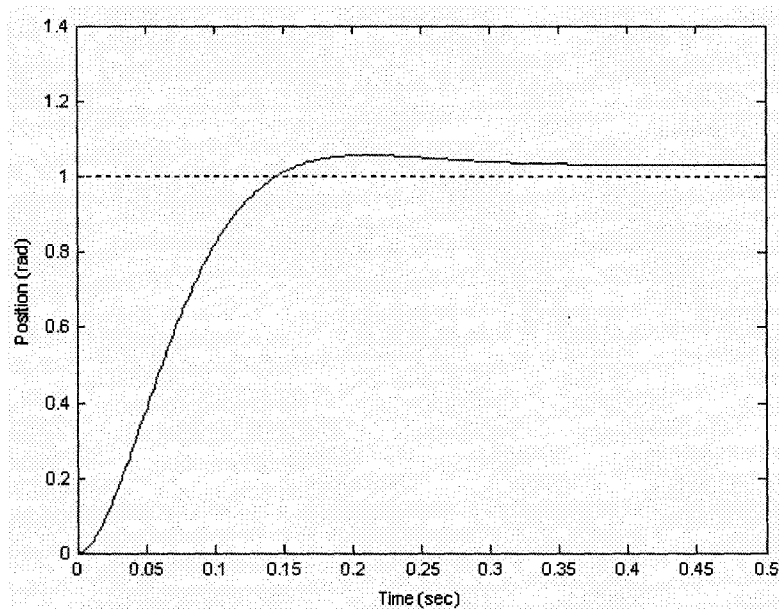


Figure 57: Closed-loop response of step input with  $K_p = 2,000$  and  $K_i = 1,000$ .

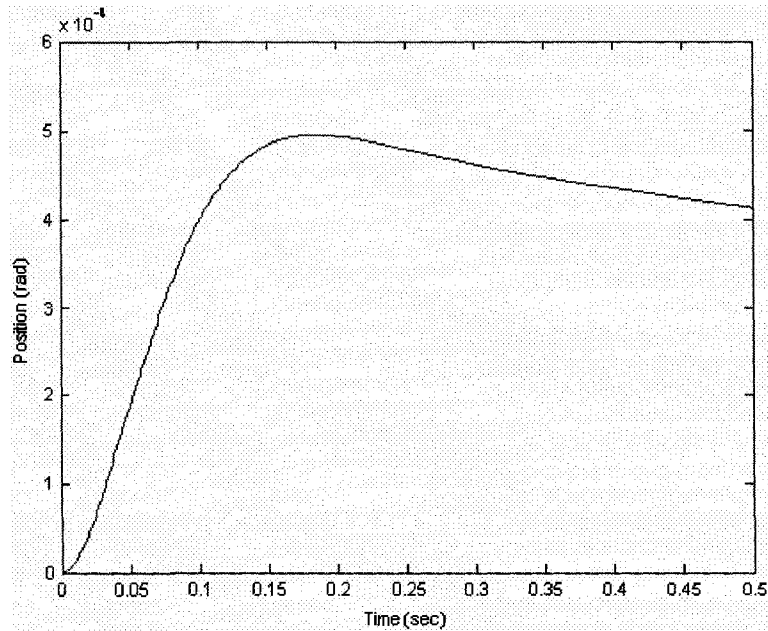


Figure 58: Closed-loop response of step disturbance with  $K_p = 2,000$  and  $K_i = 1,000$ .

Adding an integral controller, the steady-state error to a disturbance response was not reduced. The integral gain was tuned using different gain values but the system did not present any changes. Thus, a proportional gain was increased by another order of ten to speed up the response, in Figs. 59 and 60.

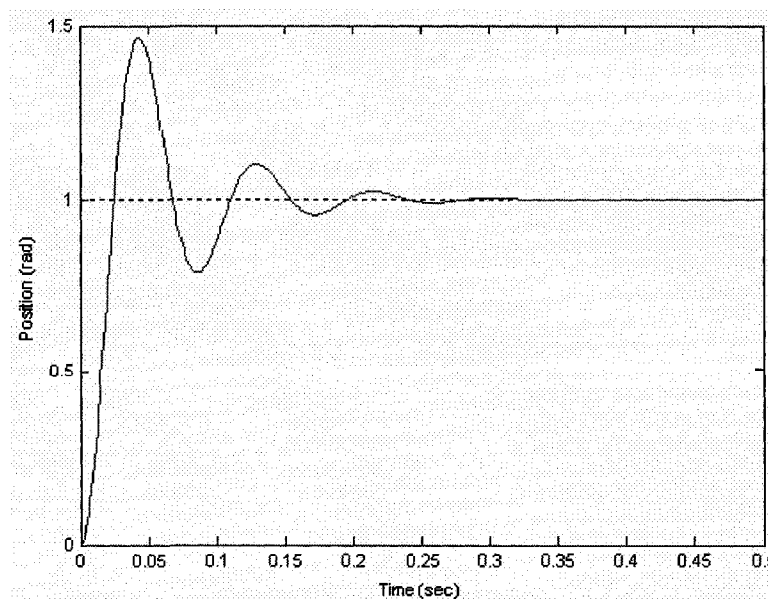


Figure 59: Closed-loop response of step input with  $K_p = 20,000$  and  $K_i = 1,000$ .

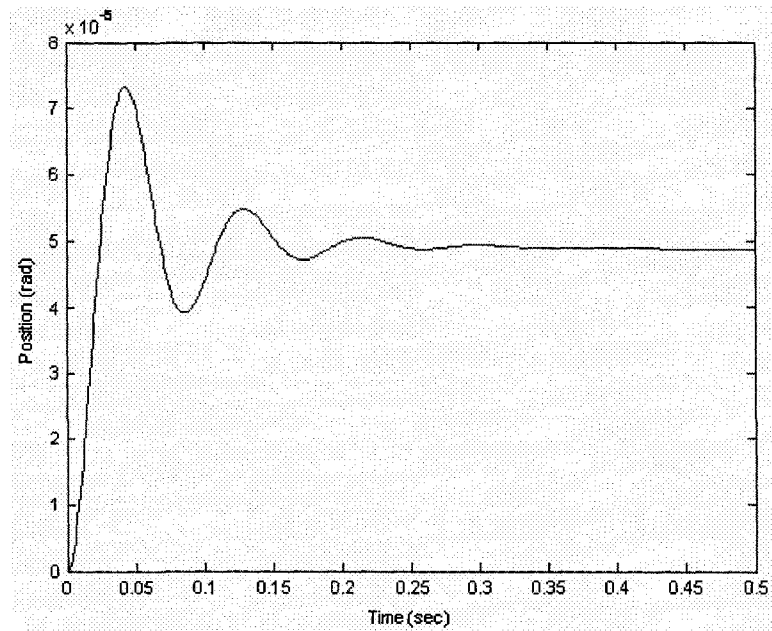


Figure 60: Closed-loop response of step disturbance with  $K_p = 20,000$  and  $K_I = 1,000$ .

Now, the response to the system is faster but the transient response worsened.

So, a derivative controller was added to reduce the overshoot, as it is illustrated in

Figs. 61 and 62.

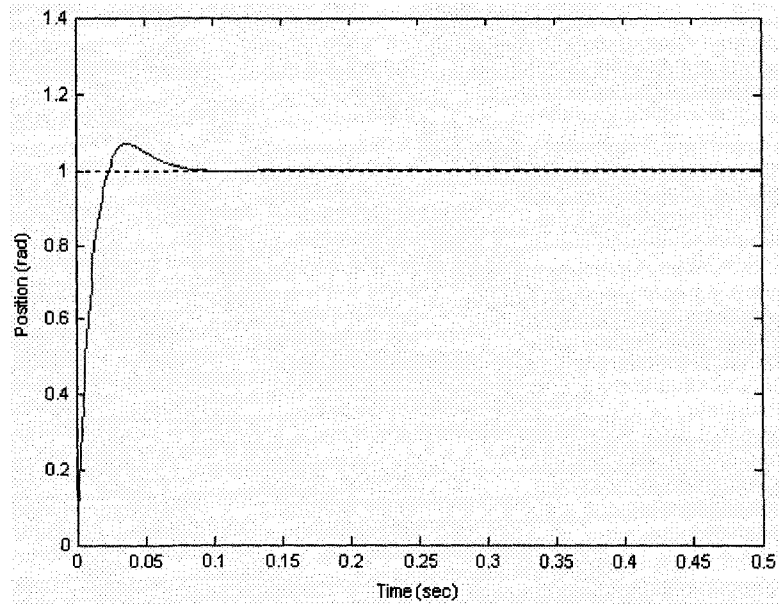


Figure 61: Closed-loop response of step input with  $K_p = 20,000$ ,  $K_I = 1,000$  and  $K_d = 300$ .

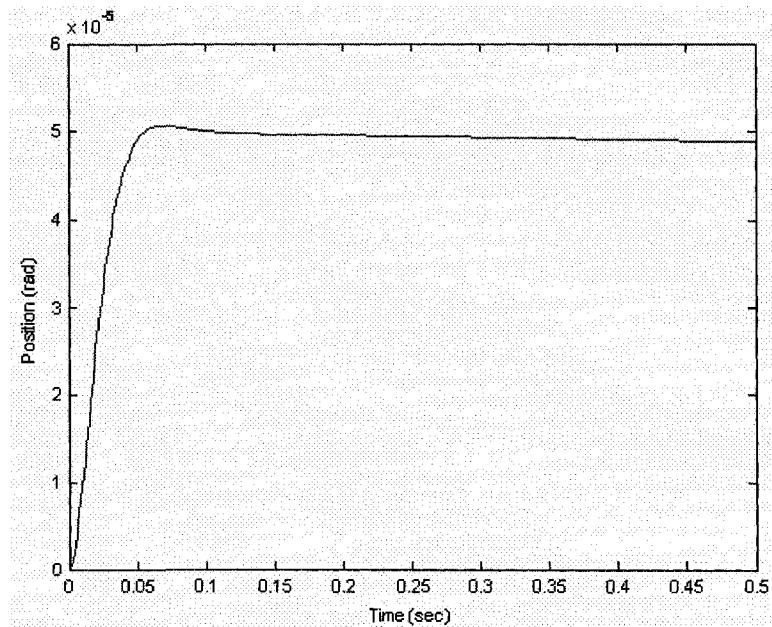


Figure 62: Closed-loop response of step disturbance with  $K_p = 20,000$ ,  $K_I = 1,000$  and  $K_d = 300$ .

Even though the step input response with PID controller looks satisfactory, i.e. less than 10% overshoot, settling time of 0.2 seconds, and no steady-state error, the step disturbance response is still not zero. So the integral gain was increased to speed

up the disturbance response. Other controllers were tried to optimize the response characteristics. This is illustrated in Figs. 63 and 64.

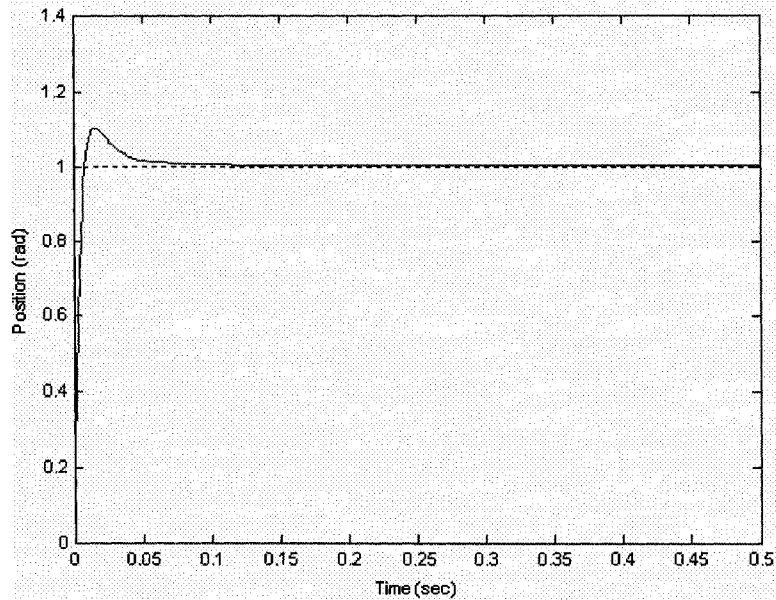


Figure 63: Closed-loop response of step input with  $K_p = 80,000$ ,  $K_I = 900,000$  and  $K_d = 900$ .

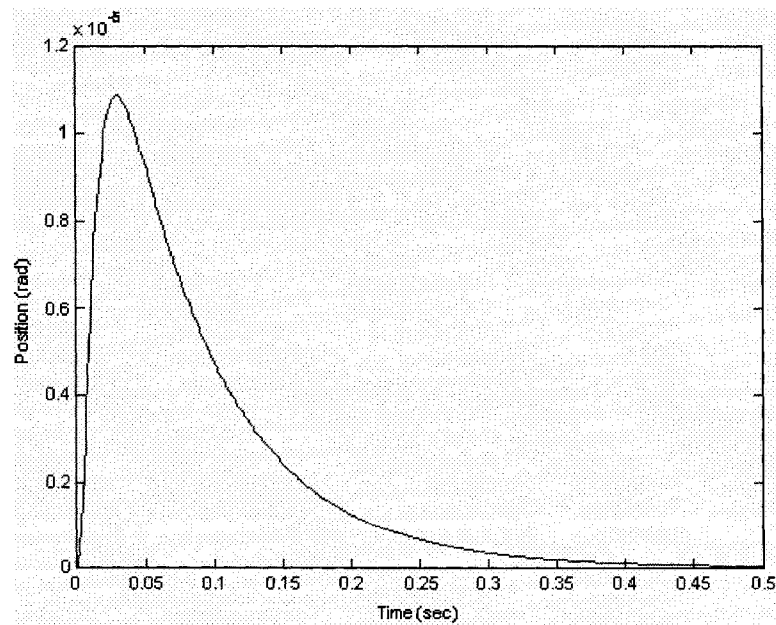


Figure 64: Closed-loop response of step disturbance with  $K_p = 80,000$ ,  $K_I = 900,000$  and  $K_d = 900$ .

As a result, the PID controller with gains,  $K_p = 80,000$ ,  $K_I = 900,000$  and

$K_d = 900$ , satisfy the system design criteria including the step disturbance steady-state error.

### 3.5 Torque Rod Angle of Twist

Since the torque rod is about 730 mm long and 6 mm in diameter, there will be a twist deformation. The torque rod is a hollow composite tube with the outside diameter,  $r_o$ , of 6 mm and 1 mm wall thickness. The fundamental relationship between shear stress, torque and geometry equation is given as the following (Benham, 1987):

$$\frac{T}{J} = \frac{\tau}{r} = \frac{G\theta}{L} \quad (72)$$

Here,  $T$  is the torque in [Nm],  $J$  is the polar second moment of area in [ $m^4$ ],  $\tau$  is the shear stress in [ $N/m^2$ ] at the radius  $r$  in [m],  $G$  is the shear modulus in [ $N/m^2$ ], and  $\theta$  is the angle of twist in radians over the length,  $L$  in [m]. The polar second moment of area for the cross-section is given as:

$$J = \frac{\pi}{2}(r_o^4 - r_i^4) \quad (73)$$

Therefore, re-arranging Eq. (73) to find the angle of twist of the torque rod:

$$\theta = \frac{TL}{JG} \quad (74)$$

where the shear modulus of the composite material is about 42.8 GPa. Thus, the angle of twist is found to be:

$$\theta = \frac{(7.88)(0.730)}{(3.77 \times 10^{-10})(42.8 \times 10^9)} = 0.35 \text{ rad} \quad (75)$$

The torque acting on the rod can be read off from Fig. 29 as 2.7 Nm. From Eq. (75), the resulting angle of twist is 0.35 rad, which is equivalent to about 20 degrees (5.6% of the circumference, 360°). Since the yield strength of the composite material is high, the torque rod can withstand these loads. The diameter of the counter-weight screw is 5 mm and the pitch is 0.75 mm, one full turn will move the counter-weight screw 0.75 mm. Therefore, referring back to Tab. 4 in section 2.4 (comparing R3), the displacement of counter-weight is about 1.8 mm in the direction of the blade tip when the blade tip is deflecting from zero to 20 degrees downward. So, it would take 2.4 revolutions for the counter-weight screw to deflect the blade tip to full 20 degrees, which is equivalent to 37.7 mm (2.4 multiplied by the circumference of the counter-weight screw). Due to the torsional twist of 0.35 rad, another 0.873 mm (torsional twist multiplied by the circumference of the counter-weight screw) needs to be added. Thus, the motor with a gearhead will have to turn 2.456 revolutions (37.7 mm plus 0.873 mm divided by circumference of the counter-weight screw) in order to deflect the blade tip to 20 degrees down.

The nominal speed for RE 30 motor is 7750 RPM and the GP 32C gearhead speed reduction ratio is 2189:1. This gives an output speed of the motor with a gearhead of about 3.54 RPM. As a result, 2.456 revolutions takes about 41.6 sec to

deflect the blade tip fully as compared to 40.7 sec to complete 2.4 revolutions. The difference (delay) is about 0.93 sec, which is considered not critical for the open-loop system.

## **4. WHIRL TOWER TESTING**

The ultimate goal of the first phase of the SHARCS project is to conduct a proof-of-concept wind tunnel campaign in AgustaWestland 4 m x 4 m wind tunnel in Italy. However, before any wind tunnel testing of rotor components, a whirl tower test has to be conducted to prove that the scaled rotor is able to withstand the nominal centrifugal loads and that all systems are operational in the rotating environment. For the whirl tower test, the orientation of the actuator was different from the previous (Chapter 2), because in order to test the ACT demonstrator on DLR's whirl tower test rig, every part had to be aligned in the axis of rotation. This would make sure that the whirl tower test rig will not run off balanced. Furthermore, the maximum force the whirl tower test rig could take was up to 30,000 N. So the number of ACT demonstrator parts had to be minimized to reduce the weight of the total system. Also, allowed to incorporate many of the lessons learnt into the design presented earlier. The whirl tower test was on-going while finalizing the SHARCS ACT subsystem. This chapter describes some aspects of whirl tower testing for the first design iteration of the ACT subsystem of the SHARCS model later.

### **4.1 Rationale**

The purpose of the whirl tower test is to test the safety and the functionality

of the ACT subsystem without considering any aerodynamic effects. A simplified prototype of the ACT was tested at DLR (German Aerospace Centre) whirl tower facility in Braunschweig. Fig. 65 shows the schematic diagram of DLR's whirl tower test rig.

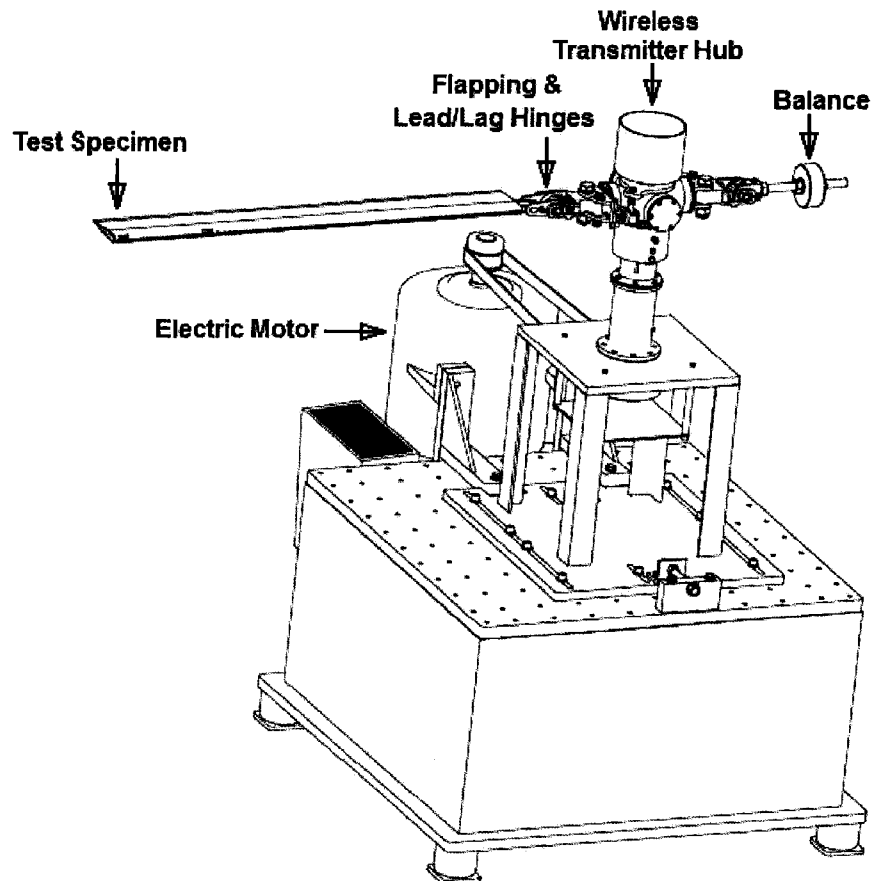


Figure 65: Schematic diagram of DLR's whirl tower test rig.

The main purpose of the whirl tower tests was to prove elements of the ACT design, especially the counter weight concept and controlling the phase delay of the system. Additional task was to check the effect of electric motor orientation to gain experience with the instrumentation of the ACT system.

## **4.2 Test Model**

The ACT was designed using PRO ENGINEER Wildfire 2.0 and 3.0, and fabricated in Science and Technology Centre at Carleton University. The fabricated ACT components were installed onto a U-profile aluminum spar representative of the actual rotor blade. The length of the spar was chosen in a way so that the ACT mechanism lies at the same radial location as on the SHARCS blade. The spar itself was shorter than the blade since the root cut-out was much larger for the DLR hub than it will be for the SHARCS hub (245 mm instead of 126 mm). The same nominal RPM was kept though, 1555 RPM.

### **4.2.1 The Counter-Weight Sizing**

The counter-weight sizing is again similar to the procedures outlined in section 2.3. The only difference is that for the whirl tower test, the mass of the blade tip was designed to be 16 grams. This is because a smaller motor than the RE 30 was only available at the time of the testing. This motor could only overcome the hinge moment of a 16 gram blade tip instead of a 30 gram one. Tab. 23 shows the geometry parameters and Tab. 24 and 25 shows the reaction forces and moments occurring within the system. Note that, since the whirl tower test was only to test the counter-

weight actuation, the aerodynamic loads were not considered. Therefore, the aerodynamic loads are not included in the following results.

Table 23: Variation of the whirl tower test components' CG with blade tip deflection

$\delta(\text{deg})$	$R1[m]$	$R2[m]$	$R3[m]$	$R4[m]$	$R5[m]$	$R6[m]$
0	0.9864	1.0402	0.9678	0.9751	0.9825	0.9835
2	0.9864	1.0403	0.9672	0.9749	0.9827	0.9837
4	0.9864	1.0404	0.9673	0.9751	0.9829	0.9838
6	0.9864	1.0404	0.9675	0.9753	0.9831	0.9840
8	0.9864	1.0403	0.9678	0.9755	0.9833	0.9841
10	0.9864	1.0402	0.9680	0.9757	0.9835	0.9843
12	0.9864	1.0400	0.9682	0.9760	0.9837	0.9845
14	0.9864	1.0397	0.9684	0.9762	0.9840	0.9846
16	0.9864	1.0394	0.9687	0.9764	0.9842	0.9848
18	0.9864	1.0390	0.9689	0.9767	0.9844	0.9850
20	0.9864	1.0385	0.9691	0.9769	0.9847	0.9851

Using Eqs. 25 to 33 gives the centrifugal and reaction forces in order to deflect the blade tip for the whirl tower test components were obtained.

Table 24: Centrifugal and reaction forces on whirl tower testing component on anhedral and tip

$\delta(\text{deg})$	$F_{ANH,CG}[N]$	$M_{ANH,CG}[Nm]$	$F_{TIP,CG}[N]$	$M_{TIP,CG}[Nm]$	$F_{TIP,red}[N]$
0	441.39	1.62	207.23	0.64	335.62
2	441.44	0.64	207.26	0.65	202.92
4	441.46	-0.33	207.29	0.67	51.68
6	441.46	-1.31	207.33	0.68	-96.51
8	441.43	-2.28	207.36	0.69	-241.30
10	441.37	-3.25	207.39	0.70	-383.12
12	441.28	-4.22	207.43	0.71	-522.35
14	441.16	-5.18	207.46	0.72	-659.38
16	441.02	-6.13	207.50	0.73	-794.54

18	440.85	-7.08	207.53	0.74	-928.19
20	440.65	-8.01	207.57	0.75	-1060.63

Table 25: Centrifugal and reaction forces on whirl tower testing component on link and counter-weight

$\delta(\text{deg})$	$F_{LINK,CG}[N]$	$F_{LINK,rea}[N]$	$F_{CW,CG}[N]$	$F_{CW,rea}[N]$	$F_{RESULT}[N]$
0	108.10	218.92	461.11	680.03	680.03
2	108.07	89.64	460.79	550.43	550.43
4	108.09	-57.74	460.87	403.14	403.14
6	108.12	-202.15	460.97	258.82	258.82
8	108.14	-343.26	461.07	117.81	117.81
10	108.17	-481.46	461.18	-20.28	-20.28
12	108.19	-617.15	461.28	-155.87	-155.87
14	108.22	-750.69	461.39	-289.30	-289.30
16	108.24	-882.42	461.50	-420.92	-420.92
18	108.27	-1012.67	461.61	-551.06	-551.06
20	108.29	-1141.74	461.72	-680.02	-680.02

Also, the resultant torque required to deflect the blade tip from zero to 20 degrees are shown in Tab. 26 with a safety factor of 1.5.

Table 26: Torque required for ACT to overcome centrifugal acceleration

$\delta(\text{deg})$	$T[Nm]$	$T_C[Nm]$	$T_{RESULT}[Nm]$	$T_{SF}[Nm]$
0	0.70	0.44	1.14	1.71
2	0.56	0.36	0.92	1.38
4	0.41	0.26	0.68	1.01
6	0.27	0.17	0.43	0.65
8	0.12	0.08	0.20	0.30
10	-0.02	-0.01	-0.03	-0.05
12	-0.16	-0.10	-0.26	-0.39
14	-0.30	-0.19	-0.48	-0.73
16	-0.43	-0.27	-0.71	-1.06
18	-0.57	-0.36	-0.92	-1.38
20	-0.70	-0.44	-1.14	-1.71

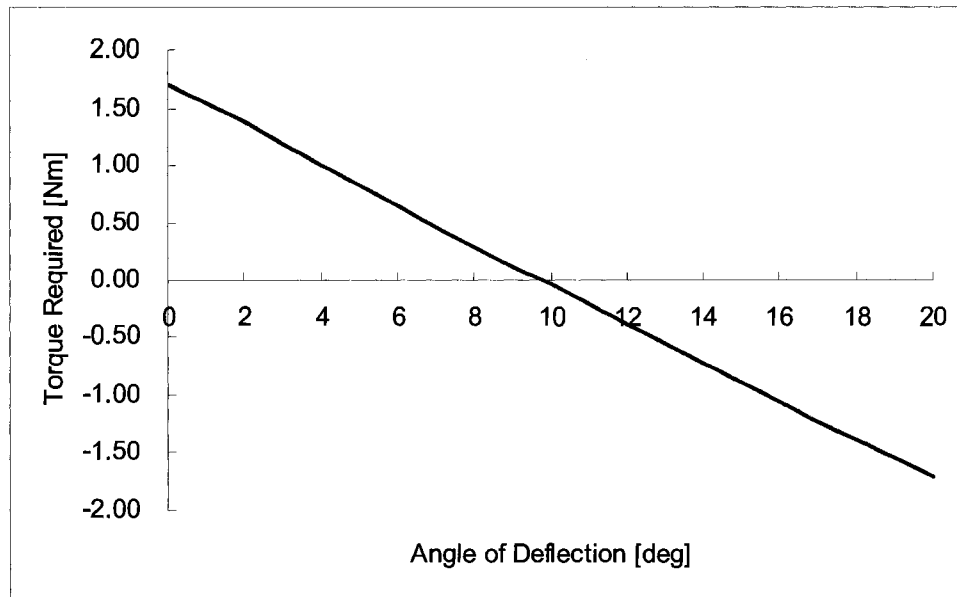


Figure 66: Resultant torque required to deflect the blade tip for whirl tower test.

#### 4.2.2 Motor Characteristics

The major requirement for selecting an electric motor was based on the torque needed to deflect the blade tip. The problem is that there is no such motor which could satisfy the torque required to deflect the blade tip in miniature size. The size of the motor is proportional to the torque that the motor can produce. Therefore, a motor with a gearbox was needed to satisfy the torque requirement. Graupner 33G 6V, a motor with a gearhead from Germany, was available and thus this was incorporated into the design (in fact, the parameters of this motor were driving the counter-weight design). Since the motor manufacturer was unable to provide the detailed characteristics on the Graupner 33G 6V motor, there were obtained experimentally.

It has to be noted that the Graupner motor company build their motors for

hobby purposes. Their motors are mostly used in model ships, tanks, trucks or airplanes. Tab. 27 shows some of the characteristics of motor that the Graupner provided.

Table 27: Characteristics of Graupner 33G 6V motor

Parameters	Values
Voltage	6 V
Current drain	0.3 A
Gear ratio	1953:1
Dimensions	65x33 mm
Shaft diameter	5 mm
Length of shaft	9 mm
Weight	125 g

Obviously, key parameters, such as motor torque are missing. To quantify this, a simple experiment was carried out. The test was accomplished by using a two inch diameter aluminum pulley fitting the Graupner's gearhead shaft (see Fig. 67).

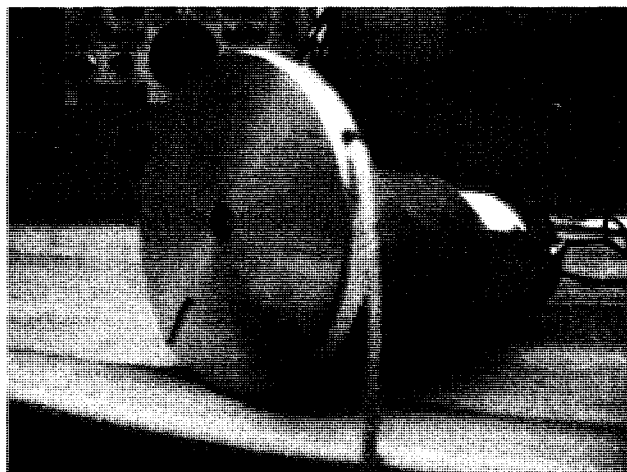


Figure 67: Motor with aluminum pulley.

Also, Fig. 68 shows the schematic test set up of finding the maximum torque

of the motor. An oscilloscope was connected between a 1 Ohm resistor to measure and monitor the current and voltage signal.

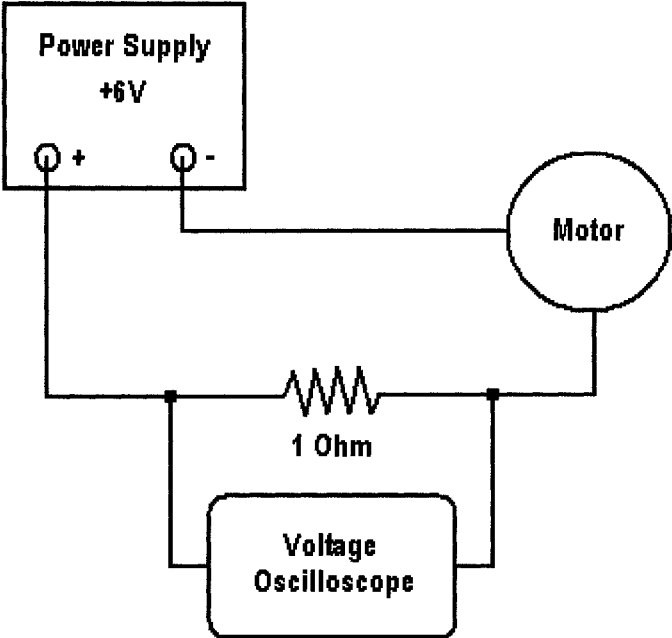


Figure 68: Experimental set up to measure the motor torque.

First, no load was hanged on the pulley and the voltage from the power supply was set to 3V. Then it was measured how many revolutions could the motor rotate in 30 seconds. Next, the voltage was increased to 5V and to 7V, respectively. The second set of experiments was done with certain weight hanged on the pulley. Gradually, more and more weight was added until the motor would not rotate at all at 7V. Tab. 28 represents the speed and voltage for different loads and Fig. 69 and 70 show a relationship of the speed and current versus voltage.

Table 28: Motor speed and current at Different Loads on the Motor

a) Load = 0 kg

<b>Voltage (V)</b>	<b>Current (A)</b>	<b>Speed (rad/s)</b>
3	0.15	0.08976
5	0.16	0.2217
7	~0.16	0.2513

b) Load = 0.2343 kg

<b>Voltage (V)</b>	<b>Current (A)</b>	<b>Speed (rad/s)</b>
3	0.15	0.07854
5	0.16	0.1904
7	~0.16	0.2417

c) Load = 1.1586 kg

<b>Voltage (V)</b>	<b>Current (A)</b>	<b>Speed (rad/s)</b>
3	0.17	0.06545
5	0.17-0.18	0.1653
7	~0.18	0.2244

d) Load = 4.563 kg

<b>Voltage (V)</b>	<b>Current (A)</b>	<b>Speed (rad/s)</b>
3	0.5	0
5	0.3	0.1428
7	0.3	0.1963

e) Load = 5.7216 kg

<b>Voltage (V)</b>	<b>Current (A)</b>	<b>Speed (rad/s)</b>
3	0.5	0
5	0.3-0.4	0.0952
7	0.35-0.42	0.1745

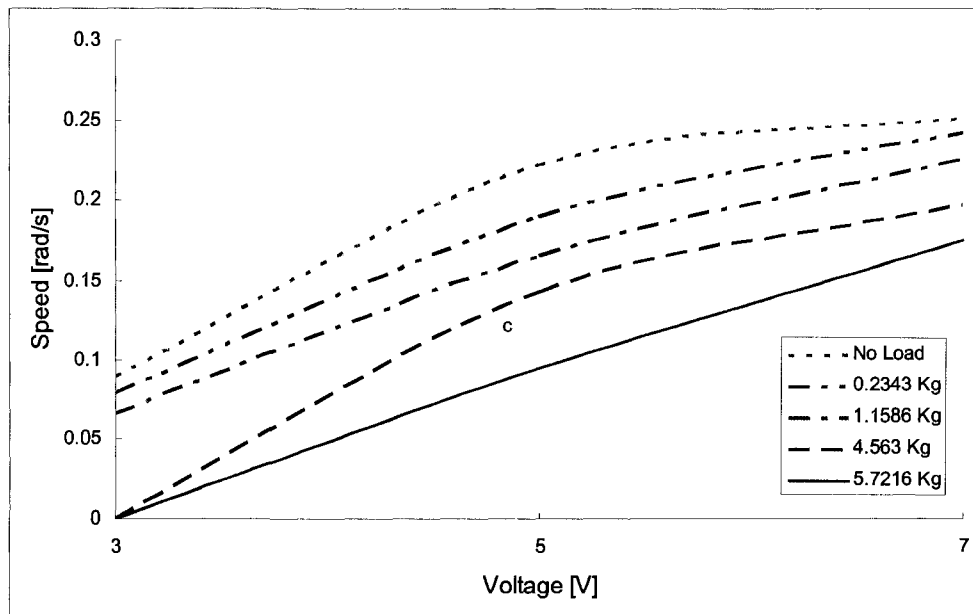


Figure 69: Relationship of motor speeds required to lift different loads at different voltages.

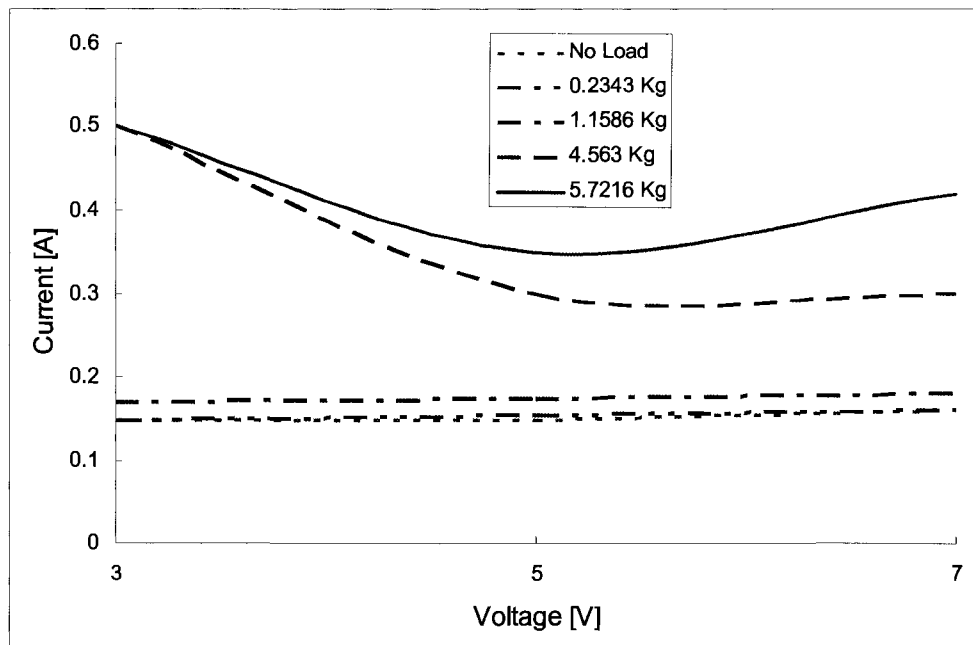


Figure 70: Relationship of current required to lift different loads at different voltages.

The motor worked both in the clock and counter clockwise directions. The maximum current that the motor could handle was 0.5 A. Therefore, for the whirl tower test, the maximum current to be supplied should be at least 0.5 A. A load of 5.7

kg produced a moment of 1.4Nm. Since the motor took 18 seconds to turn a load of 5.7 kg  $\frac{1}{2}$  rotation, this meant that the motor will approximately take one minute and 30 seconds to deflect the blade tip 20 degrees down during a whirl tower test at DLR.

In conclusion, the maximum motor torque was identified to be 1.4 Nm, which is less than the torque required to operate at 1555 RPM. However, it was concluded that this motor could work up to 1200 RPM. Also, it would take 40 seconds to deflect the blade tip by 20 degrees.

#### **4.2.3 Overall Assembly**

To measure the tip deflection and the operation of the system, two Hall Effect Transducers were installed on the ACT mechanism. The first one was glued on the blade tip to monitor the tip deflection while the second one was glued on the torque rod at the gearhead shaft to check the rotation of the gearhead shaft. The Hall Effect Transducer is a sensor which measures the magnetic field and converts the magnetic field to a voltage signal (Tahar, 1999). Fig. 71 shows the Hall Effect Transducer sensor on the blade tip while Fig. 72 shows the Hall Effect Transducer sensor on the gearhead shaft.

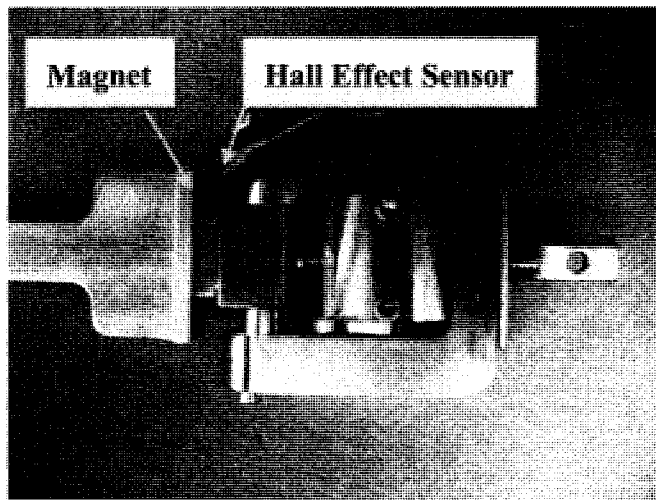


Figure 71: Hall effect transducer sensor locations on the blade tip.

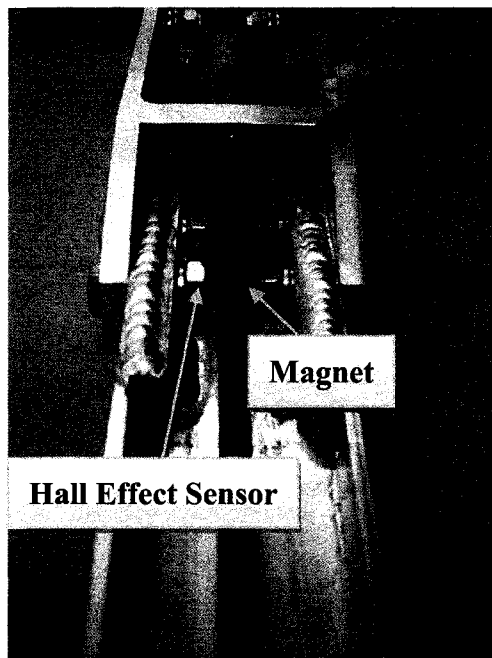


Figure 72: Hall effect transducer sensor locations on the gearhead shaft.

For the whirl tower test, all the parts including bolts, nuts and screws holding the ACT on the aluminum spar, were closely examined and calculated for their shear and yield strengths. This was important in designing the whirl tower test demonstrator since safety was of the most important factors. Note that the centrifugal acceleration at the blade tip is about 2,600 g's, i.e. any loose parts would fly off with extremely

high kinetic energy. Also, the whirl tower rig would become suddenly unbalanced and endanger the structural integrity of the rig. Fig. 73 is a prototype of the Actively Controlled Tip to be tested at DLR Braunschweig.

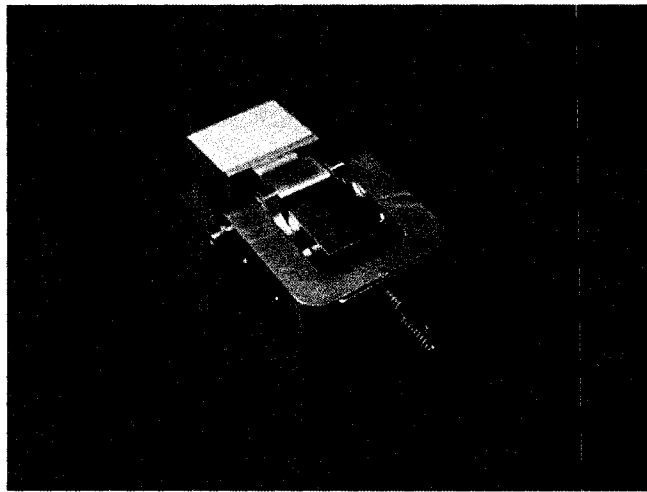


Figure 73: Prototype Active Controlled Tip design.

To ensure that the limit bearing stresses are not exceeded, extra aluminum blocks had to be welded on the aluminum spar to increase the effective thickness. The aluminum welding was done at Science and Technology Centre in Carleton University. As Fig. 74 illustrates the aluminum welds were smoothly placed on the spar. Extra aluminum blocks were added at the blade tip, the demonstrator hinge, and the motor attachment.

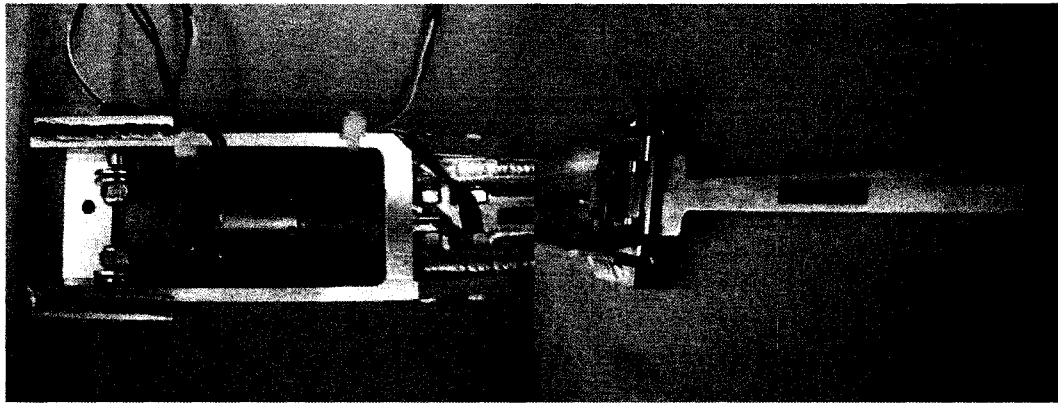


Figure 74: Aluminum welds on ACT whirl tower prototype.

For further information on the ACT demonstrator components, test specimens, and motor attachment, refer to Appendix B, C, D, E, F and G. (Appendix G is the centrifugal load calculation on Actively Controlled Flap)

As it was mentioned before, the whirl tower test ACT demonstrator was designed and fabricated before finalizing the SHARCS ACT design; therefore there are few design differences. One is the use of a ball screw to minimize the friction between the threads. However, the disadvantage of this solution is that the ball screw is not self locking. Therefore, for the SHARCS ACT design (with friction threads) has been used. Other difference regards the orientation of the actuator which was explained at the beginning of this chapter.

### **4.3 Results**

The ACT demonstrator was first balanced on the whirl tower test rig. The

blade tip was painted red to enable visual detection of the deflection too. A digital camera was set up to record the blade tip deflection as the whirl tower rig rotates.

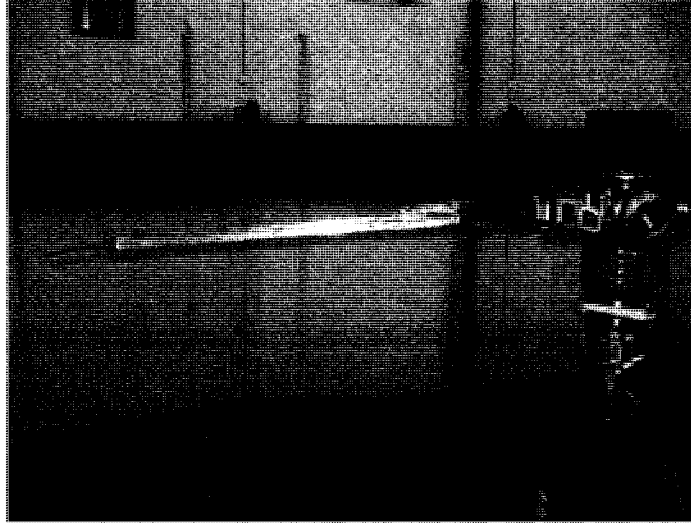


Figure 75: ACT on DLR's whirl tower test rig.

The power supply for the hall effect sensors and the electric motor of the ACT was facilitated via a series of slip rings available on the whirl tower. Data were transmitted using wireless transmitter located on the test rig hub to the control room (Fig. 76).

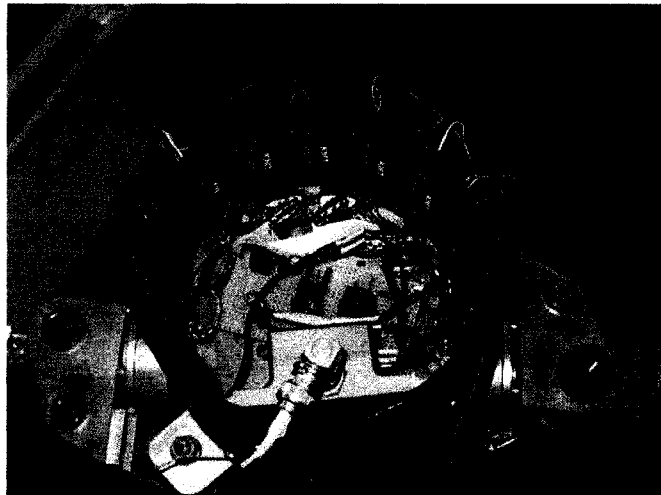


Figure 76: Wireless transmitter for the whirl tower test rig.

The ACT system was first tested at 400 RPM. The blade tip deflected successfully down to 20 degrees. It took about one minute for the blade tip to deflect down to 20 degrees and another minute to come back to zero degrees. The movie clip was recorded during the testing.

The next test was to rotate the ACT system at 700 RPM. The blade tip did not deflect down at 700 RPM. Examination of the system showed the failure of the motor as the cause of the problem. This was identified by removing the ACT mechanisms at the end of the blade tip from the demonstrator. This left only the ACT motor with the gearhead on the whirl tower rig. It was observed that even without any load (ACT removed from the tip), the gearhead shaft did not rotate. This observation was monitored from the whirl tower control room via the hall sensor located on the torque rod. During this process, test engineers at DLR did not notice the overload on the motor, which meant that the motorshaft was rotating. Otherwise, the current signal should have indicated overload and should have burned the motor. Thus, this problem ended the ACT whirl tower test at DLR and the investigation on the failure of the motor and the gearhead was performed back at Carleton to improve the design of the ACT system.

## 4.4 Failure Analysis

After the whirl tower test at DLR, investigating the cause of the failure of gearhead was necessary to improve the design or to re-select the actuator for the ACT system. Visual inspection of the aluminum spar's exterior showed that even at 700 RPM, which was about half of the nominal rotation of speed, the CW of the assembled ACT components was off-positioned from its original position. Fig. 77 shows the CW holding the ball screw nut, which sled off from its original position about 5 mm in the radial.

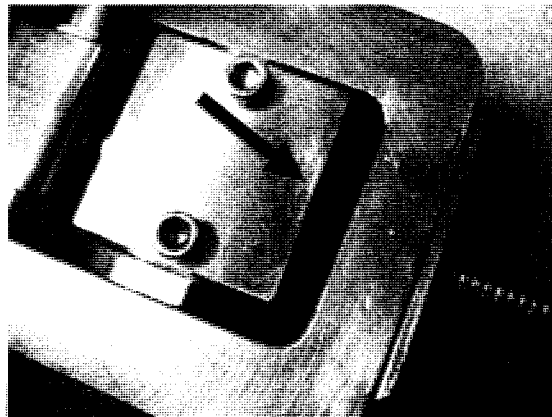


Figure 77: Off-position of counter-weight on ball screw.

The electrical tapes holding the wires and cables for ACT system and Hall Effect Transducer sensors at the side of the aluminum spar were also off-positioned radially. This verified that large centrifugal loads were acting on the test specimen.

The Graupner's electric motor was connected to the power supply to check if the motor was still working properly at static condition. The motor was in good health

and did not show any defect at static condition. For an accurate investigation on the motor, the gearhead was opened and examined for small particles that may have stuck between the gears to cause abnormal rotation of the gearshaft. An examination of the gearhead revealed no rotation limiting objects but instead, the gearhead was full of lubrication grease (Fig. 78).

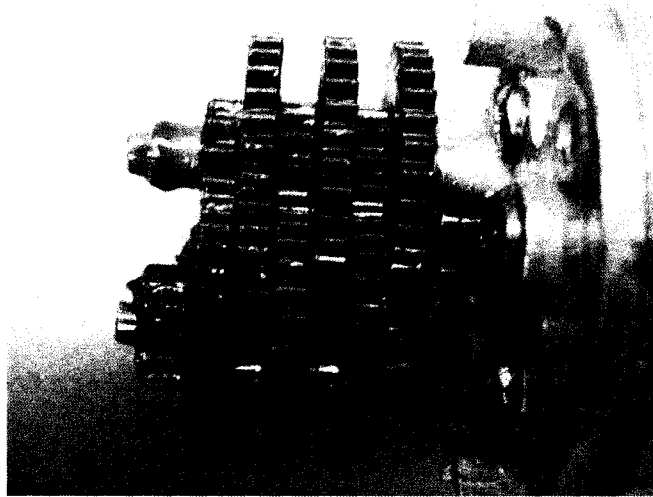


Figure 78: Graupner's gearhead.

Two hypotheses were made from the investigation of the gearhead. The first hypothesis was that when a motor started to rotate at 700 RPM, the gears inside the gearhead got shifted due to the centrifugal acceleration and there was no contact between the motorshaft to the first gear. To verify that the gears may have not been in a contact with each other, careful analysis of measuring the inside of the gearhead was carried out using a micro-caliper. However, this analysis showed that there was no possible way for gears to lose contact with the connecting gears.

The second hypothesis was that the friction between the gears was too large to rotate the gears. The equipments in the whirl tower control room at DLR indicated that the motor was rotating. As it was stated earlier, if the motor takes power but does not rotate, the motor burns. However, since the motor did not show any defects, it was concluded that the gears may have been slipping inside the gearhead between the motorshaft and the first gear during the whirl tower testing at 700 RPM. When Graupner motor was first bought and tested for its maximum torque ability by hanging a weight of 10 kg, the gearshaft did not rotate but the motorshaft did rotate. So a follow up experiment was performed to reproduce the slipping motion of the motorshaft but the same result could not be reproduced.

Therefore, from the investigation of the failure, few conclusions were made in order to prevent another failure in the next test. A tight fit is needed between the gear and the motorshaft and inside the gearhead. Also the gears may have to be made thicker to increase its contacting surfaces to not loose its contacts. Lastly, thrust bearings may be needed to reduce the friction between the gears due to the centrifugal loads, or the motor should be oriented perpendicular to the centrifugal acceleration, since it is more likely to be able to withstand larger radial than axial loads.

#### **4.5 Static Test of ACT**

Since the ACT actuator system was not tested at its maximum RPM whirl tower rotation speed, a static test was performed to check whether the system was capable to produce the nominal torque/hinge moment. A static test was set by hanging weight was hanged near the blade tip to generate the moment caused by the centrifugal load at 20 degree deflection. Fig. 79 shows the static test set up for the ACT at Carleton University.



Figure 79: Static test set up.

The weights were carefully added one by one in order to avoid damage of the ACT actuator system. The reason for the static test was to check if the ball screw was able to self lock the blade tip at the designated deflection angle.

From section 2.3.3, the maximum moment was found to be 7.33 Nm using a counter-weight concept. Thus, the weight needed to be hanged at the end of the blade tip to produce the same effect as the whirl tower test rig was calculated as following.

Since the blade tip is fabricated out of aluminum, putting a hole and hanging weights on a thin dummy blade tip will result a crack and the breakage. Therefore, as illustrated in Fig. 80, the mass was hanged close to the hinge, at the indicated area.

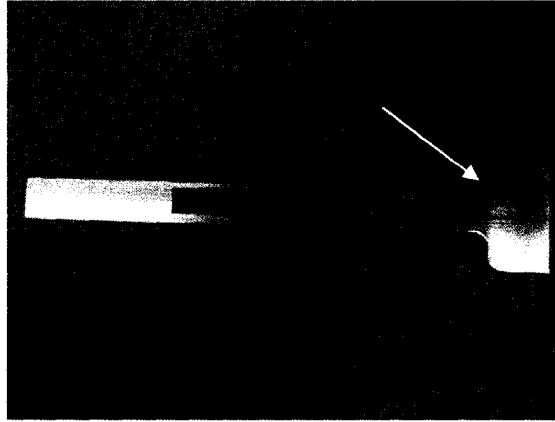


Figure 80: Location of moment arm for ACT prototype.

The required mass to be hanged could be calculated from:

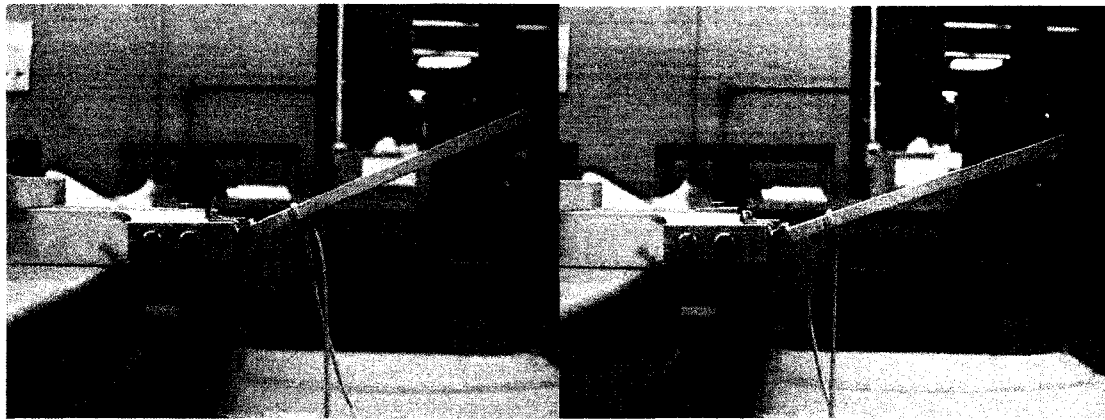
$$7.33 = mgL \quad (76)$$

Here  $m$  is the mass of hanged weight at the blade tip,  $g$  is the gravity constant,  $L$  is the length of the moment arm.

$$7.33 = m(9.81)(0.026035)\cos 20^\circ \quad (77)$$

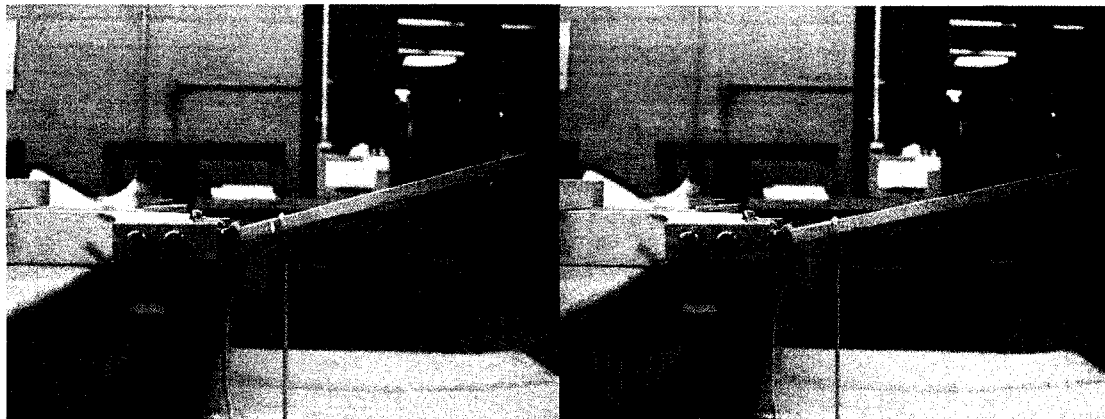
$$m = \frac{7.33}{(9.81)(0.026035)\cos 20^\circ} = 30.54Kg \quad (78)$$

From this calculation, the mass needed to simulate the same effect for the whirl tower test environment was found to be 30.54 kg. Fig. 81 shows the static test at 20 degree deflection. The static test at 20 degree deflection was carried out upside down to hang the mass at its best position.



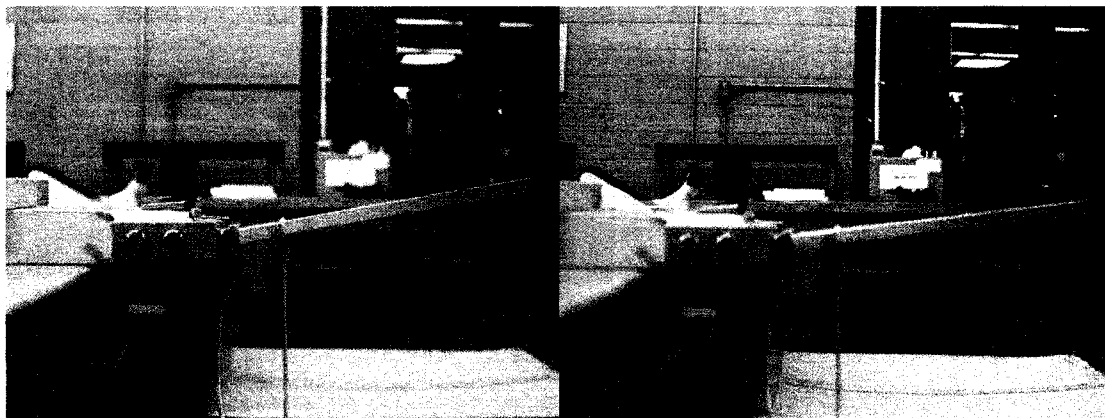
a) No Load

b) 0.635 kg



c) 5.198 kg

d) 9.759 kg



e) 14.179 kg

f) 18.745 kg

Figure 81: Static test at 20 degree deflection as hanging mass increases.

Fig. 81 clearly illustrates that the ACT system did not self lock at 20 degree deflection. The ACT system could not handle the load beyond 18.745 kg. Every time

when weights were hanged, the blade tip could not hold its original start position. The weights added for the static test was about half of the weight required to generate the whirl tower test environment.

After all the weights were removed, the ACT system was carefully examined.

Fig. 82 shows the brass bushing inside the horseshoe and its steel plate cover. The function of the brass bushing was to guide the CW to rotate in a still position.

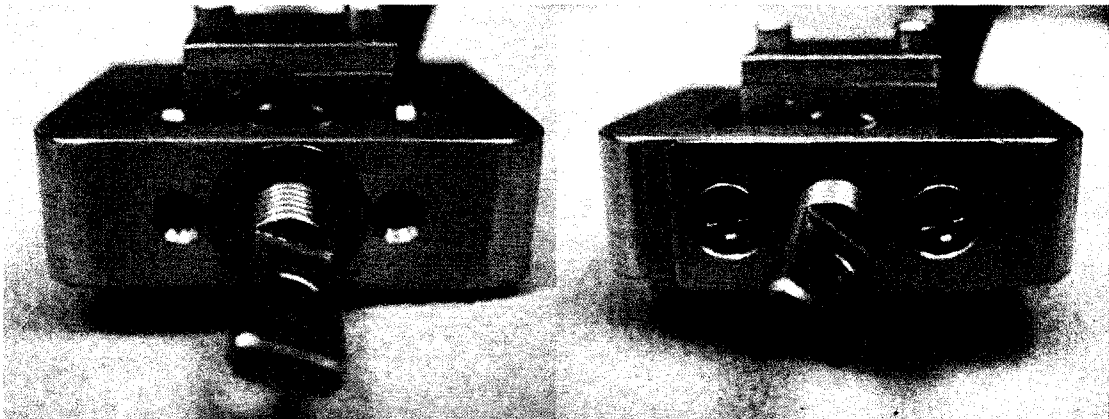


Figure 82: Brass bushing inside the horseshoe.

However, this brass bushing was too weak to hold the weight on the blade tip. The brass bushing, which guides the ball screw was heavily bent when the weights were removed from the static test. Also the steel plate, which covers the brass bushing attached on the horseshoe was not strong enough. Refer to Figs. 83 and 84 for the flaws on the ACT system after the static test.

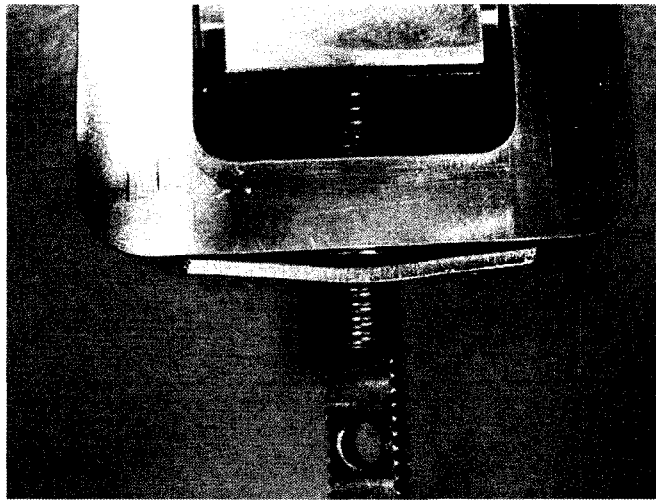


Figure 83: Bent steel plate cover.

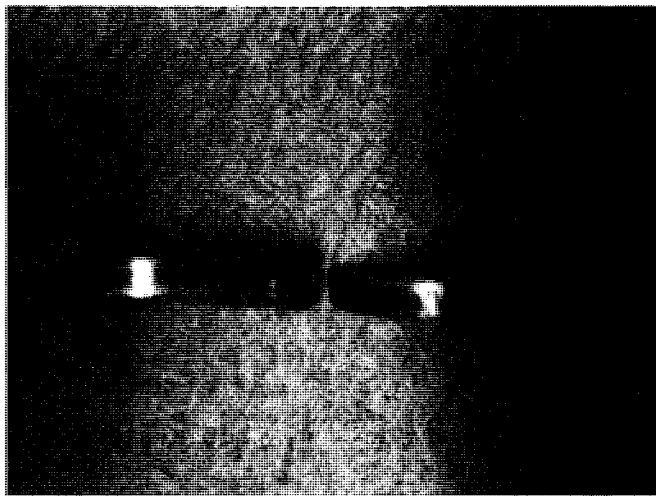


Figure 84: Bent brass bushing.

This concluded that the weakness of the brass bushing would also have been a failure factor if the whirl tower test was carried out to its maximum rotating speed. The dummy blade tip (made of aluminum) was not bent after the static test. A few design changes were needed to fix this problem.

#### **4.6 Recommendations**

The Graupner motor had failed during the whirl tower test at DLR and a new actuation system was proposed for the ACT system. The radial location of the electric motor's CG during the whirl tower test was at 311 mm from the centre of rotation. Even though the CG of the Graupner motor was located close to the centre of the rotation, the ACT system failed at 700 RPM. Tab. 29 shows the acceleration and gravity forces at different RPM to compare what 1 gram of mass would feel at 311 mm from the centre of rotation.

Table 29: Acceleration and gravity forces at different RPM for a mass of 1 gram

<b>RPM</b>	<b>400</b>	<b>700</b>	<b>1555</b>
<b>Category</b>			
<b>Speed (rad/sec)</b>	41.89	73.30	162.84
<b>Centrifugal Acceleration (m/s<sup>2</sup>)</b>	545.68	1,671.14	8,246.67
<b>Gravity Force (G)</b>	55.62	170.35	840.64
<b>Centrifugal Load (N)</b>	0.546	1.671	8.246

At 400 RPM, the centrifugal acceleration at the location of the motor, was found to be 545.68 m/s<sup>2</sup>, which was equivalent to 55.62 g's. So one gram of mass would feel like 546 grams at 400 RPM. Thus, at 1555 RPM, every gram inside the gearhead and the motor would feel like 8.2 kg is pulling towards the centrifugal acceleration direction.

Previously, the motor was oriented radially along the blade. After the investigating of the motor and gearhead failure, the alternative solution was to re-

orient the motor and the gearhead position. A new arrangement of the motor and the gearhead was to turn the actuation system perpendicular to the span-wise direction along the airfoil so that centrifugal loads can be minimized on the gears. Fig. 85 illustrates the new motor and gearhead arrangement, which actually has already been included in the design presented in section 2.4.

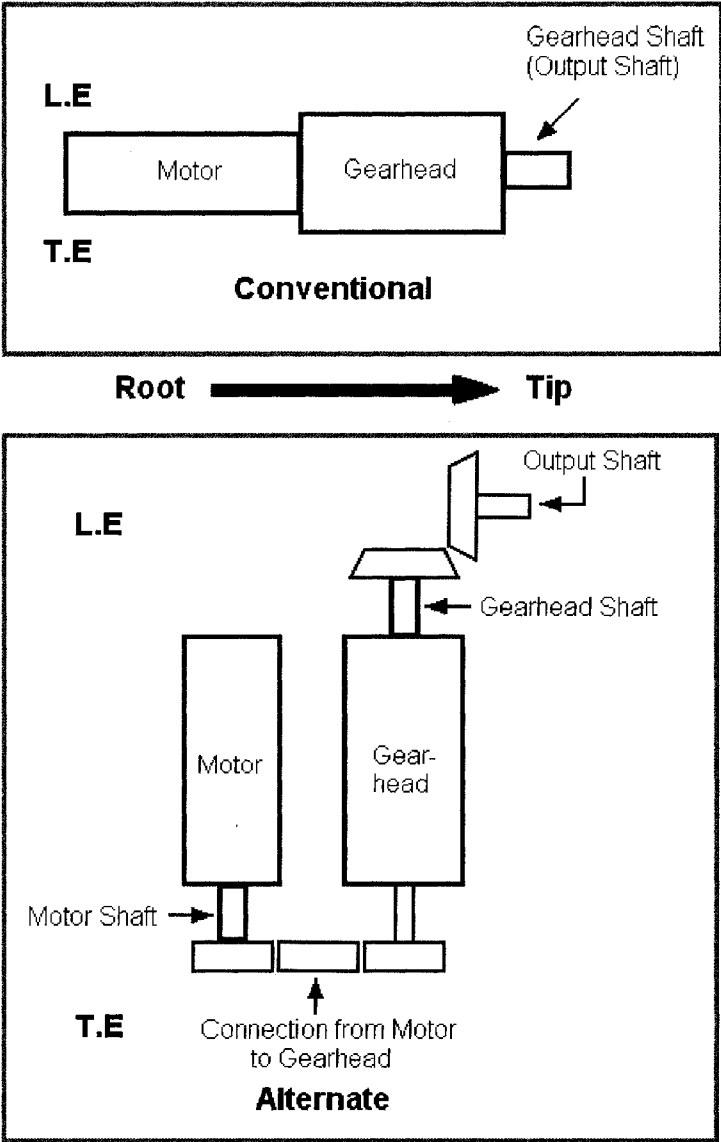


Figure 85: New motor and gearhead arrangement.

This new arrangement will surely minimize the friction between the gears.

But the problem is still to find a motor and a gearhead which is small enough to fit inside the blade. Since SHARCS is a small-scaled blade, the available size of the motor and the gearhead is very much limited. The diameter of both the motor and the gearhead was needed to be a maximum of 10 mm, while the length should be not more than 35 mm. An intensive research was made to find a compact and powerful motor with a gearhead which could produce the required torque; however, it appears to be not possible with the diameter of 10 mm limitation for the motor and the gearhead.

## 5. CONCLUSIONS AND RECOMMENDATIONS

The Actively Controlled Tip is a mechanism which is used to reduce the noise produced by rotor blade tip. The ACT will be activated by the pilot during certain flight regimes, such as forward flight and descent/landing. The purpose of the ACT is to displace the blade tip vortex and by this, to reduce rotor BVI (blade slap) noise. In order to achieve this process, the ACT has to be able to deflect the blade tip from 0 degrees to 20 degrees downward.

The major challenge of the ACT system is the excessive resultant hinge moment to be overcome at the blade tip. The summations of the centrifugal loads and the aerodynamic loads have proved the resultant load being too high for any actuator to overcome. Also, the sizing of the ACT was difficult to compromise since the ACT mechanism have to fit inside a 12 mm thick blade.

Therefore, a counter-weight concept was proposed in order to halve the required hinge moment and to balance the torque at 10 degree deflection. The key idea of the counter-weight concept is to allow the blade tip to rotate freely without any load from 0 degree to 10 degrees, beyond which point, the actuator power will help to complete the blade tip motion down to 20 degrees (see Fig. 19). This is the original novelty of this concept.

The screw-jack mechanism generates translational motion from rotational

motion via an electric motor located at the blade root via a torque rod running over the blade from the root to the tip. The reason for why locating the electric motor at the blade root is that there is less centrifugal load at the blade root compared to the blade tip. Also an electric motor itself is too heavy and large to be located at the blade tip.

A whirl tower test was conducted at DLR Braunschweig (German Aerospace Centre) to prove the concept of the ACT. The result of the whirl tower test has shown that the ACT mechanism can deflect from zero degree to 20 degrees at 400 RPM only. At higher RPM, the ACT mechanism was not able to deflect the blade tip due to the motor failure. The investigations on failure have been determined that the centrifugal loads on each gear inside the gearhead were too high and, thus, friction between each gear arose which was too high to overcome.

For future work, the ACT mechanism has to be fabricated according to latest design version presented in Chapter 2. After the ACT has been assembled inside the airfoil, it needs to be tested at AgustaWestland in Italy with the Actively Controlled Flap and Active Pitch Link in the 4 m x 4 m wind tunnel. Also the self-locking mechanism has to be tested in wind tunnel to check whether or not deflecting the blade tip actually reduces the noise.

Even though the proof of prototype concept did not work the concept of the ACT is still valid. Moreover, the counter-weight concept is a novelty in this work.

Also, there are no smart materials or any kind of actuators which could satisfy the ACT actuator design criterion. Thus, later on when there is an available technology to overcome the resultant load, the ACT system will be a convincing, fascinating and extra-ordinary design.

## REFERENCES

- American Eurocopter LLC, "EC155",  
<http://www.eurocopterusa.com/Product/ec155/EC155.asp>, 2004.
- Anderson, J., "A History of Aerodynamics and its Impact on Flying Machines",  
Cambridge University Press, Cambridge, England, 1997.
- Aoyama, T., Kondo, N., Aoki, M., Nakamura, H., Saito, S., "Calculation of rotor  
blade-vortex interaction noise using parallel super computer", 22nd European  
Rotorcraft Forum, The Royal Aeronautical Society, Vol. 2, 1996.
- Atassi, H., Subramaniam, S., Scott, J., "Acoustic Radiation from Lifting Airfoils in  
Compressible Subsonic Flow", 13th Aeroacoustics Conference, American Institute of  
Aeronautics and Astronautics, Ta!lahassee, Florida, October 22-24, 1990.
- Arnaud, G., Niesl, G., "Low noise design of the EC 135 helicopter", American  
Helicopter Soceity 52<sup>nd</sup> Annual Forum, Washington D.C., June 4-6, 1996.
- Becerra, V., Garces, F., Kambhampati, C., Warwick, K., "Strategies for Feedback  
Linearization: A Dynamic Neural Network Approach", Springer-Verlag, London,  
2003.
- Benham, P., Crawford, R., Armstrong, C., "Mechanics of Engineering Materials",  
Pearson Education Limited, 1996.
- Booth, E., Brooks, T., "Rotor Blade-Vortex Interaction Noise Reduction and  
Vibration using Higher Harmonic Control", 16<sup>th</sup> European Rotorcraft Forum,  
Glasgow, UK, September, 1990.
- Brentner, K., Farassat, F., "Modeling aerodynamically generated sound of  
helicopter rotors", Progress in Aerospace Sciences, Vol. 39, pp. 83-120, 2003.
- Carnegie Mellon University Libraries, "Control Tutorial for MatLAB and Simulink",  
<http://www.library.cmu.edu/ctms/>, July 14, 2007.

Chopra, I., Shen, J., Yang, M., “Swashplateless Helicopter Rotor with Trailing Edge Flaps for Flight and Vibration Control”, *Journal of Aircraft*, Vol. 43, March-April, 2006

Clark, B., “Noise and vibration worldwide”, Vol. 27, pp. 16, 1996.

Clark, B., “Helicopter manufacturer tests blade performance by attaching self-contained data collection system to rotor during flight”, *Aircraft Engineering and Aerospace Technology*, Vol. 70, pp. 206-208, 1998.

Concilio, A., Gianvito, A., Koopmann, G., Tiseo, B., “Smart Tunable Dynamic Vibration Absorbers”, 12<sup>th</sup> and 27<sup>th</sup> American Institute of Aeronautics and Astronautics Aeroacoustics Conference, Cambridge, Massachusetts, May 8-10, 2006.

Coton, F., Marshall, J., Galbraith, R., Green, R., “Helicopter Tail Rotor Orthogonal Blade Vortex Interaction”, Department of Aerospace Engineering, University of Glasgow, 2004.

Domke, B., “Helicopter Rotorhead Gallery”, <http://www.b-domke.de/AviationImages/Rotorhead.html>, 2004.

Edwards, B., Cox, C., “Revolutionary concepts for helicopter noise reduction-S.I.L.L.E.N.T. program”, NASA/CR-2002-211650, 2002.

Feszty, D., Nitzsche, F., Cha, M., Khomostov, K., Lynch, B., Mander, A., Oxley, G., Poirier, F., Ulker, D., “SHARCS: Smart Hybrid Active Rotor Control System Design Report”, Rotorcraft Research Group, Department of Mechanical and Aerospace Engineering, Carleton University, 2007.

Ford, T., “Advances in Rotorcraft”, *Aircraft Engineering and Aerospace Technology*, Vol. 69, pp. 447-452, 1997

Friedmann, P., Depailler, G., “Reduction of Vibration due to Dynamic Stall in Helicopters using an Actively Controlled Flap”, 43<sup>rd</sup> AIAA/ASME/ASCE/AHS/ASC Structures, Structural Dynamics, and Materials Conference, Denver, Colorado, April 22-25, 2002.

Gandhi, F., Anusonti-Inthra, P., "Helicopter Vibration Reduction through Cyclic Variations in Rotor Blade Root Stiffness", *Journal of Intelligent Material Systems and Structures*, Vol. 11, February, 2000.

Ghorashi, M., Mikjaniec, T., Lynch, B., Ulker, D., Cha, M., Mander, A., Brassard, P., Feszty, D., Nitzsche, F., "Preliminary Design of a Scaled Rotor Blade with Vibration and Noise Control Devices", Rotorcraft Research Group, Department of Mechanical and Aerospace Engineering, Carleton University, 2005.

Hawkyard, M., Powell, B., Stephenson, J., McElhone, M., "Fatigue Crack Growth from Simulated Flight Cycles Involving Superimposed Vibrations", *21<sup>st</sup> International Journal of Fatigue*, 1999

Hofinger, M., Leconte, P., "Development of an Active Flap Rotor Model", 2004

Jacklin, S., Blaas, A., Teves, D., Kube, R., "Reduction of Helicopter BVI Noise, Vibration, and Power consumption through Individual Blade Control", *American Helicopter Society 51<sup>st</sup> Annual Forum*, Fort Worth, Texas, May 9-11, 1995.

Jackson, D., "Helicopter Yaw Control Methods",  
<http://www.aerospaceweb.org/question/helicopters/q0034.shtml> July 8, 2001

Johansson, S., Winberg, M., Lago, T., Claesson, I., "A new Active Headset for a Helicopter Application", *5<sup>th</sup> International Congress on Sound and Vibration*, pp. 327-334, Adelaide, South Australia, 1997.

Johnson, W., "Helicopter Theory", Dover Publications Inc., 1980

Kloepfel, V., Kube, R., "On the role of prediction tools for Adaptive Rotor System Developments", *Smart Materials and Structures*, Vol.10, pp. 137-144, September 20, 2000.

Leishman, G., "Principles of Helicopter Aerodynamics", Cambridge University Press, 2000

Leverton, J., "Helicopter Noise – Blade Slap", NASA Contractor Report 1221, NATIONAL AERONAUTICS AND SPACE ADMINISTRATION, WASHINGTON, D.C., OCTOBER 1968.

Leverton, J., "Twenty five years of rotorcraft aeroacoustics: Historical prospective and important issues", *Journal of Sound and Vibration*, Vol. 133, pp. 261-287, 1989.

Lighthill, M., "The Bakerian Lecture, 1961. Sound generated aerodynamically", *Proceedings of the Royal Society of London. Series A, Mathematical and Physical Sciences*, Vol. 267, pp. 147-182, May 8, 1961.

Liguore, S., Followell, D., "Vibration Fatigue of Surface Mount Technology (SMT) Solder Joints", *Proceedings Annual Reliability and Maintainability Symposium*, IEEE, 1995.

Lynch, B., Ghorashi, M., Nitzsche, F., "On the use of Shape Memory Alloy Wires for Anhedral Angle Control in Helicopter Rotor Blades", *CASI AERO 2007*, Toronto, Canada, April 24 - 26, 2007.

Malovrh, B., Gandhi, F., Tauszig, L., "Sensitivity of helicopter BVI-induced and vibration to variations in individual interaction-parameter", *American Helicopter Society 57th Annual Forum*, Washington, DC, May 9-11, 2001.

McDonal Douglas Helicopter Company, "MD600 Features and Benefits", The Boeing Company, 2006.

Miu, D., "Mechatronics: Electromechanics and Contromechanics", Springer-Verlag, 1992

Munsky, B., Gandhi, F., Tauszig, L., "An Analysis of Helicopter Blade-Vortex Interaction Noise with Flight Path or Attitude Modification", *American Helicopter Society 58th Annual Forum*, Montreal, Canada, June 11-13, 2002.

Olsen, W., Wagner, J., "Effect of Thickness on Airfoil Surface Noise", *American Institute of Aeronautics and Astronautics*, Vol. 20, pp. 437-439, 1982.

Ritchie, E., "Dynamic Modeling of the Mechanical System", Course E5-2, Institute of Energy Technology, Aalborg University, 2003

Shigley, J., "Machine Design", McGraw-Hill, 1956.

Shin, S., Cesnik, C., “Helicopter Vibration Reduction in Forward Flight using Blade Integral Twist Control”, 43rd AIAA/ASME/ASCE/AHS/ASC Structures, Structural Dynamics, and Materials Conference, Denver, Colorado, April 22-25, 2002.

Silver, G., “National Helicopter Noise Coalition”,  
<http://www.vannoise.org/hilolim.htm>, December 16, 1996.

Singleton, J., Yeager Jr., W., “Important Scaling Parameters for Testing Model-Scale Helicopter Rotors”, JOURNAL OF AIRCRAFT, Vol. 37, No. 3, May–June 2000.

Straub, F., Kennedy, D., Domzalski, D., Hassan, A., Ngo, H., Anand, V., Birchette, T., “Smart Material-Actuated Rotor Technology – SMART”, Journal of Intelligent Material Systems and Structures 2004.

Tahar, M., “How do Hall effect transducers work?”,  
[http://www.sciam.com/askexpert\\_question.cfm?articleID=00028188-3BF4-1C71-84A9809EC588EF21](http://www.sciam.com/askexpert_question.cfm?articleID=00028188-3BF4-1C71-84A9809EC588EF21), March 15, 1999.

Takayuki, Y., Yazaki, T., Fukugawa, S., Matsuda, T., Sato, T., “Development of SH-60K Patrol Helicopter”, Mitsubishi Heavy Industries Ltd., Technical Review, Vol. 42, December 2005.

Testa, C., Leone, S., Serafini, J., Gennaretti, M., “Aeroelastic Investigation of Hingeless Helicopter Blades With Integrated Smart Morphing Actuator”, 32<sup>nd</sup> European Rotorcraft Forum, Maastricht, the Netherlands, 12-14 September, 2006.

Weller, W., "Experimental Investigation of Effects of Blade Tip Geometry on Loads and Performance for an Articulated Rotor System", NASA Technical Report 78-53, NATIONAL AERONAUTICS AND SPACE ADMINISTRATION, Hampton, Virginia, 1979.

Wiki Books, “Rotorcraft Fundamentals: Chapter 1”,  
[http://en.wikibooks.org/wiki/Rotorcraft\\_Fundamentals/Chapter\\_1](http://en.wikibooks.org/wiki/Rotorcraft_Fundamentals/Chapter_1), October 17, 2006.

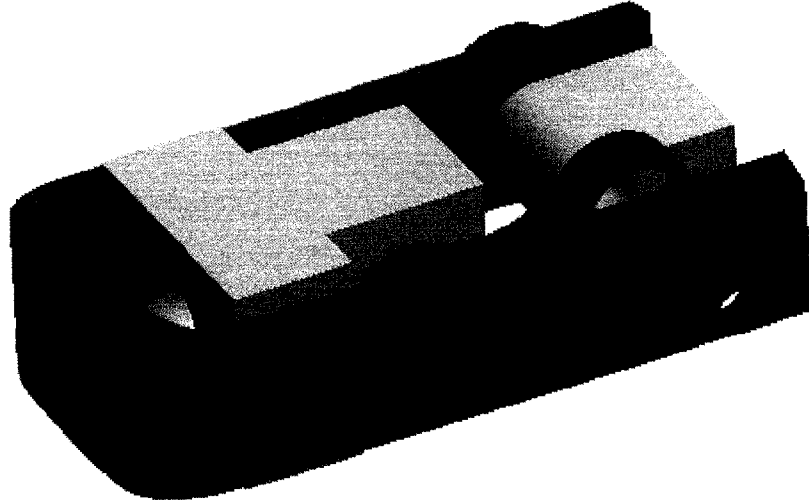
Yin, J., Ahmed, S., “Aerodynamics and Aeroacoustics of Helicopter Main-Rotor/Tail-Rotor Interaction”, American Institute of Aeronautics & Astronautics, 1999.

Yu, Y., Tung, C., Wall, B., Pausder, H., Burley, C., Brooks, T., Beaumier, P., Delrieux, Y., Mercker, E., Pengel, K., “The HART-II Test: Rotor Wakes and Aeroacoustics with Higher-Harmonic Pitch Control (HHC) Inputs - The Joint German/French/Dutch/US Project”, American helicopter Society 58th Annual Forum, American Helicopter Society International, Inc. , Montreal, Canada, June 11-13, 2002.

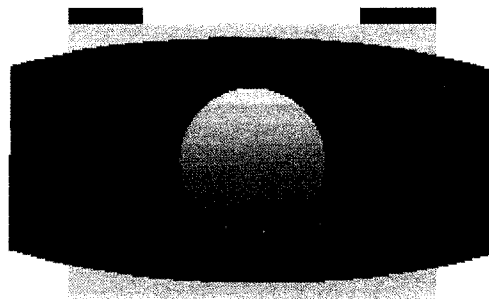
## APPENDIX A

Solid model of the ACT actuator for the SHARCS scaled blade

### 1. Assembly 3D view



### 2. Assembly front view

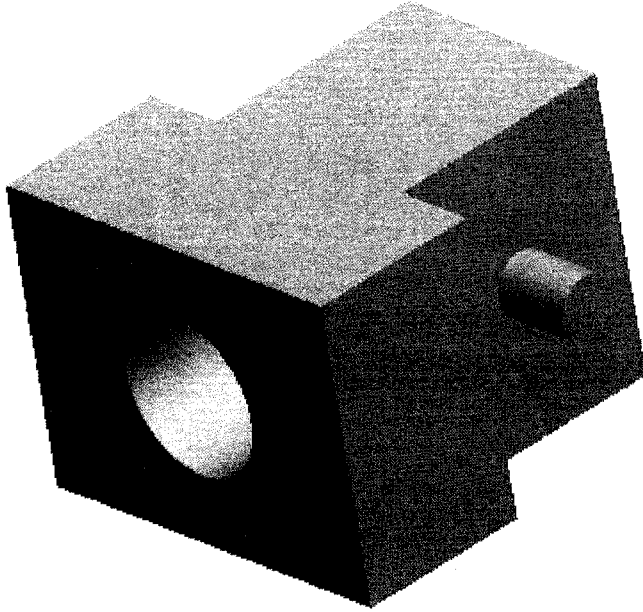


### 3. Counter-weight holder (CW HOLDER)

Density: Lead, 0.41 lb/in<sup>3</sup>

Volume: 0.16 in<sup>3</sup>

Mass: 0.066 lb → 30.015 g

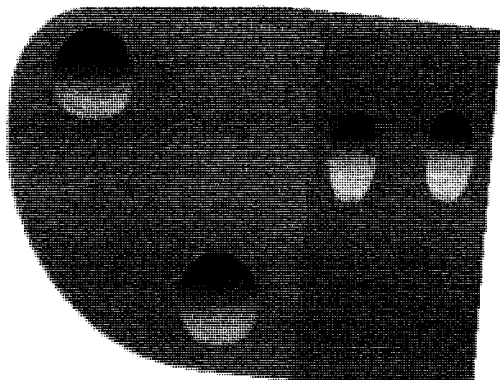


### 4. Counter-weight tip (CW TIP)

Density: Titanium, 0.16 lb/in<sup>3</sup>

Volume: 0.23 in<sup>3</sup>

Mass: 0.037 lb → 16.803 g



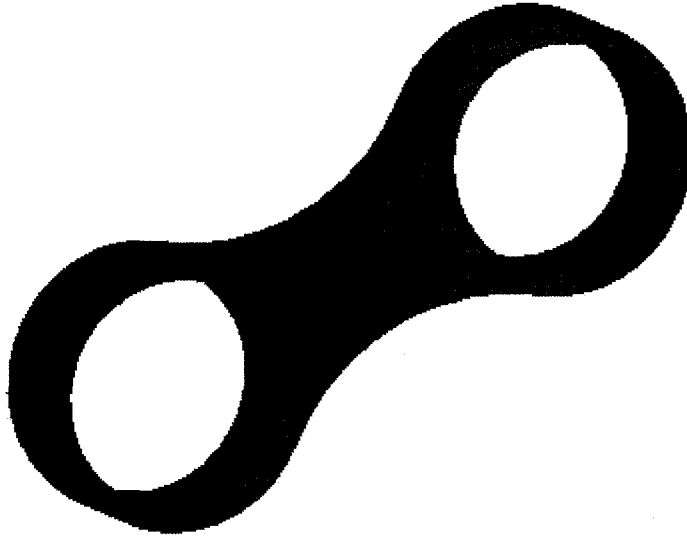
**5. Counter-weight link (CW\_LINK)**

Density: Titanium, 0.16 lb/in<sup>3</sup>

Volume: 0.0047 in<sup>3</sup>

Mass: 0.00077 lb → 0.35 g

(Need to multiply by 2 since there are 2 links)

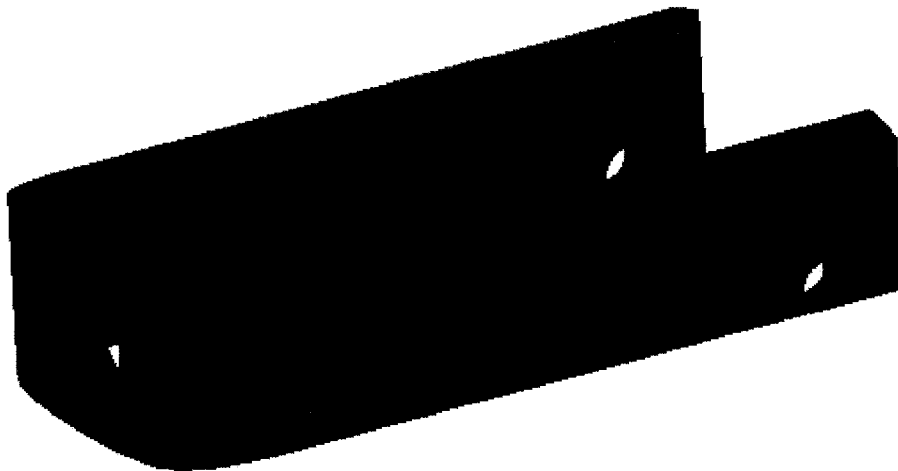


**6. Horseshoe (HORSESHOE)**

Density: Titanium, 0.16 lb/in<sup>3</sup>

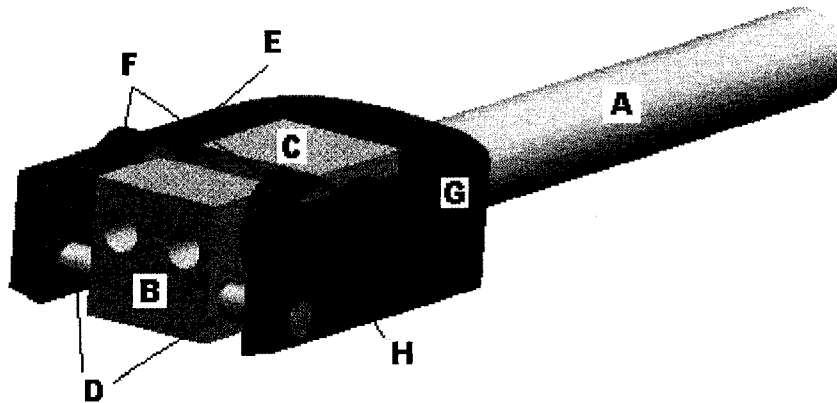
Volume: 0.11 in<sup>3</sup>

Mass: 0.018 lb → 8.14 g



## APPENDIX B

Whirl tower test ACT demonstrator

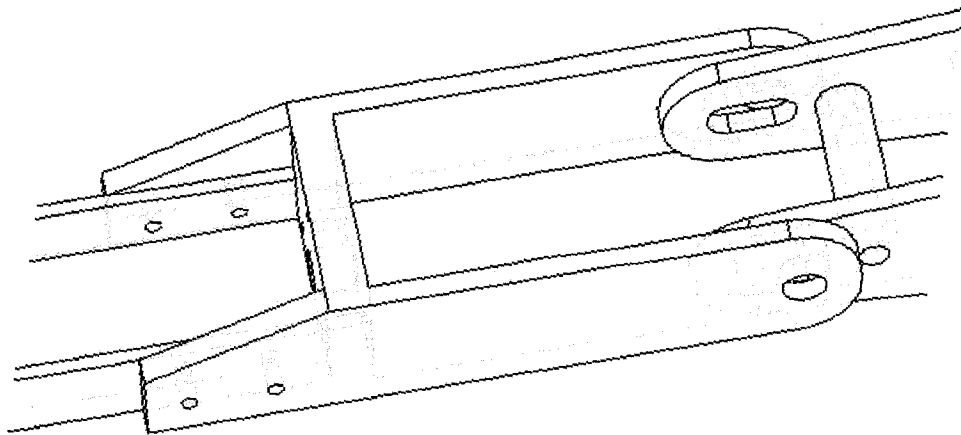
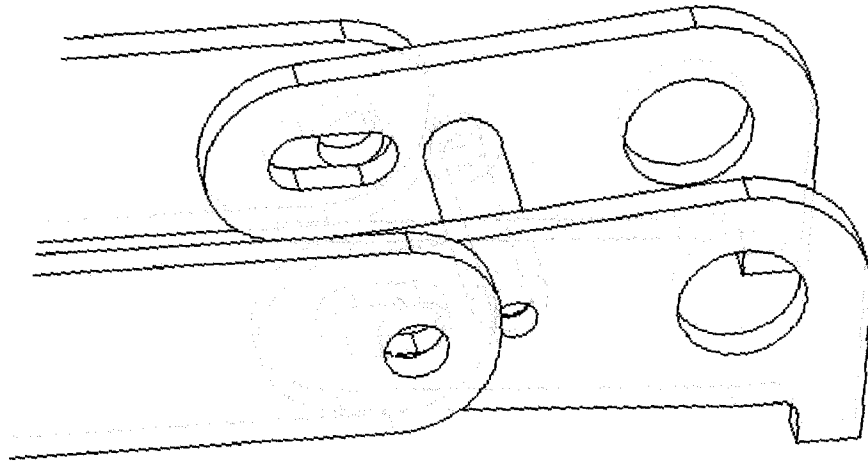
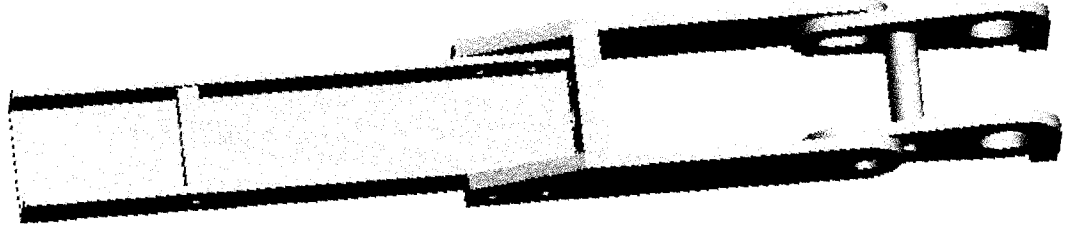


- A Screw
- B CW\_TIP
- C CW HOLDER
- D PIN\_HORSESHOE
- E BEARING
- F CW\_LINK
- G HORSESHOW
- H PIN\_TIP

Part	Material	Mass (grams)
Screw	Stainless Steel	7.98
CW_TIP	Stainless Steel	2.37
CW HOLDER	Stainless Steel	2.26
HORSESHOW	Stainless Steel	5.73
PIN_HORSESHOE	Stainless Steel	0.42
PIN_TIP	Stainless Steel	0.32
CW_LINK	Stainless Steel	0.56 (Multiply by 2)
BEARING	Bronze	0.36 (Multiply by 4)
<b>Total Mass: 21.63 grams</b>		

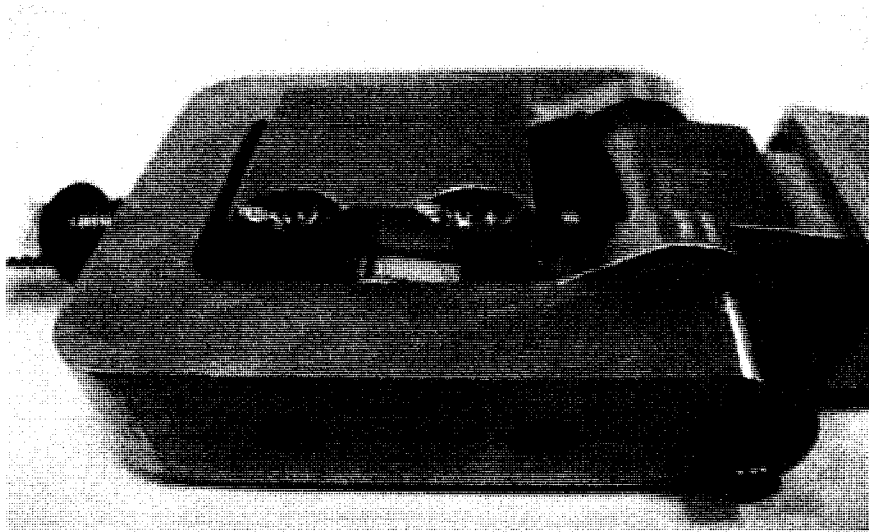
**APPENDIX C**

**WHIRL TOWER MOTOR ATTACHMENTS**

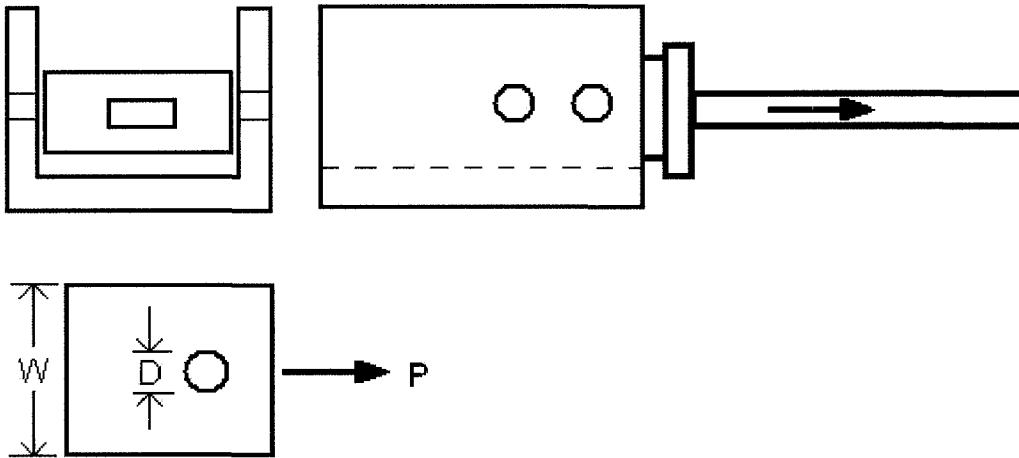


## APPENDIX D

### APPENDIX D-1: Actuator mechanisms stress analysis



#### Part A: Failure in Tension



$$P_{U(Tension)} = \sigma_U (W - D)t$$

Where  $P_{U(Tension)}$  is the ultimate tensile load,  $\sigma_U$  is the ultimate tensile strength,  $W$  is the width of the structure,  $D$  is the diameter of the hole, and  $t$  is the thickness of the structure.

$$\sigma_U = \frac{P_{U(Tension)}}{(W - D)t}$$

$$P_{U(Tension)} = mr\omega^2 = 0.146(0.9864)162.35^2 = 3800 \text{ N}$$

Where  $m$  is the mass of the system,  $r$  is the location of the system from the centre of rotation, and  $\omega$  is the angular velocity of the system.

Where  $W = 1.905 \times 10^{-2}$  m

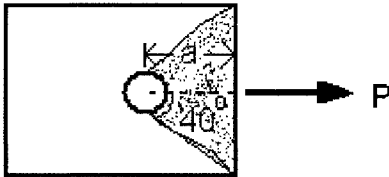
$D = 3.5052 \times 10^{-3}$  m

$t = 3.175 \times 10^{-3}$  m

$$\sigma_U = \frac{3800/2}{(1.905 \times 10^{-2} - 3.5052 \times 10^{-3})3.175 \times 10^{-3}} = 38.5 \text{ MPa}$$

$P_{U(Tension)}$  is divided by half since there are another hole in opposite side of the rectangular aluminum spar beam. For the system within 25% of the safety factor gives 48.2 MPa

#### Part B: Failure by Shear Tear Out



Where  $a$  is the distance from the end of the rectangular spar beam to the centre of the hole. The area of the half the triangle of the shear tears out is the calculated as the following.

$$A_S = 2 \frac{a}{\cos 40} t$$

$$P_{U(Shear)} = \sigma_{SU} A_S$$

Where  $P_{U(Shear)}$  is the ultimate shear load,  $\sigma_{SU}$  is the ultimate shear stress, and  $A_S$

is the shear out area.

$$\sigma_{SU} = \frac{3800/2}{2 \frac{a}{\cos 40} t}$$

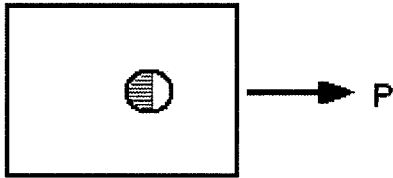
Where  $t = 3.175 \times 10^{-3}$  m

$a = 1 \times 10^{-2}$  m

$$\sigma_{SU} = \frac{3800/2}{2 \left( \frac{1 \times 10^{-2}}{\cos 40} \right) 3.175 \times 10^{-3}} = 22.92 \text{ c}$$

For the system within 25% of the safety factor gives 29 MPa

#### Part C: Failure by Bearing or Bushing on Plate



Bolt can press against the bushing wall if the pressure is high enough. The plate material adjacent to the hole will start to crush allowing the bolt and bushing to move freely in elongated hole.

$$P_{U(Bearing)} = \sigma_{BR} Dt$$

Where  $P_{U(Bearing)}$  is the ultimate bearing load,  $\sigma_{BR}$  is the allowable bearing stress,

$D$  is the diameter of the hole, and  $t$  is the thickness of the structure.

$$\sigma_{BR} = \frac{P_{U(Bearing)}}{Dt}$$

Where  $D = 3.5052 \times 10^{-3} \text{ m}$

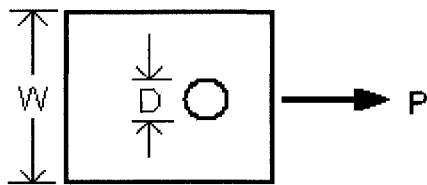
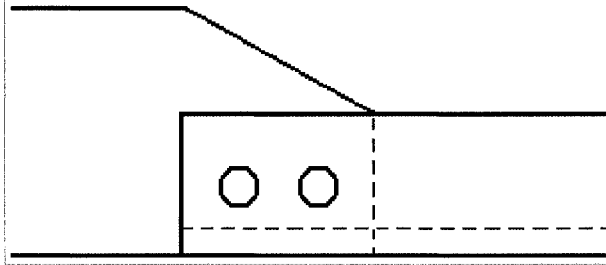
$$t = 3.175 \times 10^{-3} \text{ m}$$

$$\sigma_{BR} = \frac{3800/2}{3.5052 \times 10^{-3} (3.175 \times 10^{-3})} = 170.75 \text{ MPa}$$

For the system within 50% of the safety factor gives 256 MPa

## APPENDIX D-2: Motor Attachment

### Part A: Failure in Tension



The same theory from Appendix A-1 from previous section applies here.

$$P_{U(Tension)} = \sigma_U (W - D)t$$

$$P_{U(Tension)} = mr\omega^2 = 0.69(0.62)162.35^2 = 11300 \text{ N}$$

$$\sigma_U = \frac{P_{U(Tension)}}{(W - D)t}$$

$$\text{Where } W = 1.905 \times 10^{-2} \text{ m}$$

$$D = 6.35 \times 10^{-3} \text{ m}$$

$$t = 3.175 \times 10^{-3} \text{ m}$$

$$\sigma_U = \frac{11300/2}{(1.905 \times 10^{-2} - 6.35 \times 10^{-3})3.175 \times 10^{-3}} = 140.2 \text{ MPa}$$

For the system within 25% of the safety factor gives 175.2 MPa

Part B: Failure by Shear Tear Out

$$\sigma_{SU} = \frac{11300/2}{2 \frac{a}{\cos 40} t}$$

Where  $a = 1.27 \times 10^{-2}$  m

$$t = 3.175 \times 10^{-3} \text{ m}$$

$$\sigma_{SU} = \frac{11300/2}{2 \left( \frac{1.27 \times 10^{-2}}{\cos 40} \right) 3.175 \times 10^{-3}} = 53.7 \text{ MPa}$$

For the system within 25% of the safety factor gives 67.1 MPa

Part C: Failure by Bearing or Bushing on Plate

$$\sigma_{BR} = \frac{P_{U(Bearing)}}{Dt}$$

Where  $D = 6.35 \times 10^{-3}$  m

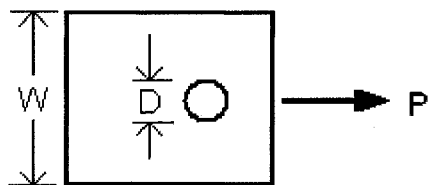
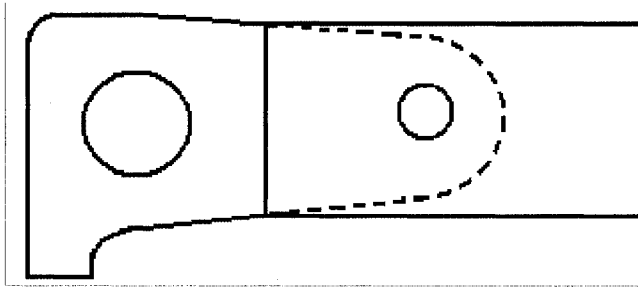
$$t = 3.175 \times 10^{-3} \text{ m}$$

$$\sigma_{BR} = \frac{11300/2}{6.35 \times 10^{-3} (3.175 \times 10^{-3})} = 280.3 \text{ MPa}$$

For the system within 50% of the safety factor gives 420.4 MPa

## APPENDIX D-3: Hub Attachment

### Part A: Failure in Tension



The same theory from Appendix A-1 from previous section applies here.

$$P_{U(Tension)} = \sigma_U (W - D)t$$

$$P_{U(Tension)} = mr\omega^2 = 1(0.62)162.35^2 = 16500 \text{ N}$$

$$\sigma_U = \frac{P_{U(Tension)}}{(W - D)t}$$

$$\text{Where } W = 3.383 \times 10^{-2} \text{ m}$$

$$D = 1 \times 10^{-2} \text{ m}$$

$$t = 5 \times 10^{-3} \text{ m}$$

$$\sigma_U = \frac{16500/2}{(3.383 \times 10^{-2} - 1 \times 10^{-2})5 \times 10^{-3}} = 69.3 \text{ MPa}$$

For the system within 25% of the safety factor gives 86.6 MPa

### Part B: Failure by Shear Tear Out

$$\sigma_{SU} = \frac{16500/2}{2 \frac{a}{\cos 40} t}$$

Where  $a = 1.5 \times 10^{-2}$  m

$t = 5 \times 10^{-3}$  m

$$\sigma_{SU} = \frac{16500/2}{2 \left( \frac{1.5 \times 10^{-2}}{\cos 40} \right) 5 \times 10^{-3}} = 42.2 \text{ MPa}$$

For the system within 25% of the safety factor gives 52.7 MPa

### Part C: Failure by Bearing or Bushing on Plate

$$\sigma_{BR} = \frac{P_{U(Bearing)}}{Dt}$$

Where  $D = 1 \times 10^{-2}$  m

$t = 5 \times 10^{-3}$  m

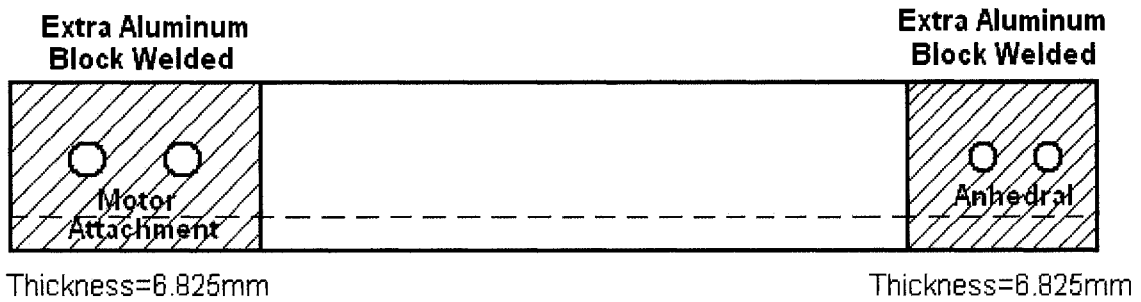
$$\sigma_{BR} = \frac{16500/2}{1 \times 10^{-2} (5 \times 10^{-3})} = 165 \text{ MPa}$$

For the system within 50% of the safety factor gives 247.5 MPa

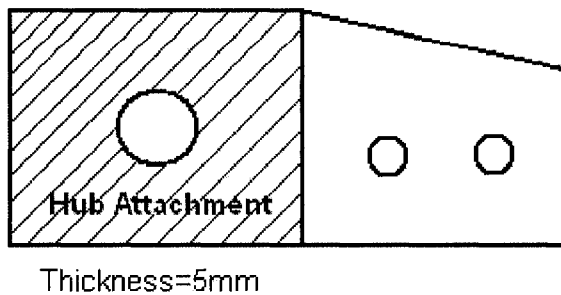
Since the aluminum yield strength is about 275 MPa, some of the load and shear calculations are needed to be fixed by welding extra aluminum blocks to increase the plate thickness. This will prevent the failure by decreasing the load and shear stresses on the aluminum rectangular blocks and holes. Appendix B proves the stress calculations.

## APPENDIX E

### APPENDIX E-1: Anhedral



### Extra Aluminum Block Welded



#### Part A: Failure by Bearing or Bushing on Plate

Mass of aluminum block added to Anhedral is 17.6 grams.

$$P_{U(Tension)} = (m + m_{add})r\omega^2 = (0.146 + 0.0176)0.9864(162.35^2) = 4253.45 \text{ N}$$

$$\sigma_{BR} = \frac{P_{U(Bearing)}}{Dt_{NEW}}$$

Where  $D = 3.5052 \times 10^{-3} \text{ m}$

$$t_{NEW} = 9.975 \times 10^{-3} \text{ m}$$

$$\sigma_{BR} = \frac{4253.45/2}{3.5052 \times 10^{-3} (9.975 \times 10^{-3})} = 60.83 \text{ MPa}$$

For the system within 50% of the safety factor gives 91.245 MPa

### Part B: Failure in Tension

$$\sigma_U = \frac{P_{U(Tension)}}{(W - D)t_{NEW}}$$

$$\text{Where } W = 1.905 \times 10^{-2} \text{ m}$$

$$D = 3.5052 \times 10^{-3} \text{ m}$$

$$t_{NEW} = 9.975 \times 10^{-3} \text{ m}$$

$$\sigma_U = \frac{4253.45 / 2}{(1.905 \times 10^{-2} - 3.5052 \times 10^{-3})9.975 \times 10^{-3}} = 13.72 \text{ MPa}$$

For the system within 50% of the safety factor gives 20.57 MPa

### Part C: Failure by Shear Tear Out

$$\sigma_{SU} = \frac{4253.45 / 2}{2 \frac{a}{\cos 40} t_{NEW}}$$

$$\text{Where } t_{NEW} = 9.975 \times 10^{-3} \text{ m}$$

$$a = 1 \times 10^{-2} \text{ m}$$

$$\sigma_{SU} = \frac{4253.45 / 2}{2 \left( \frac{1 \times 10^{-2}}{\cos 40} \right) 9.975 \times 10^{-3}} = 8.17 \text{ MPa}$$

For the system within 50% of the safety factor gives 12.25 MPa

## APPENDIX E-2: Motor Attachment

### Part A: Failure by Bearing or Bushing on Plate

Mass of aluminum block added to Motor Attachment is 31.6 grams.

$$P_{U(Tension)} = (m + m_{add})r\omega^2 = (0.69 + 0.0176 + 0.0316)0.62(162.35^2) = 12079.76 \text{ N}$$

$$\sigma_{BR} = \frac{P_{U(Bearing)}}{Dt_{NEW}}$$

Where  $D = 6.35 \times 10^{-3} \text{ m}$

$$t_{NEW} = 9.975 \times 10^{-3} \text{ m}$$

$$\sigma_{BR} = \frac{12079.76/2}{6.35 \times 10^{-3} (9.975 \times 10^{-3})} = 95.35 \text{ MPa}$$

For the system within 50% of the safety factor gives 143.03 MPa

### Part B: Failure in Tension

$$\sigma_U = \frac{P_{U(Tension)}}{(W - D)t_{NEW}}$$

Where  $W = 1.905 \times 10^{-2} \text{ m}$

$$D = 6.35 \times 10^{-3} \text{ m}$$

$$t_{NEW} = 9.975 \times 10^{-3} \text{ m}$$

$$\sigma_U = \frac{12079.76/2}{(1.905 \times 10^{-2} - 6.35 \times 10^{-3})9.975 \times 10^{-3}} = 47.68 \text{ MPa}$$

For the system within 50% of the safety factor gives 71.52 MPa

Part C: Failure by Shear Tear Out

$$\sigma_{SU} = \frac{12079.76/2}{2 \frac{a}{\cos 40} t_{NEW}}$$

Where  $t_{NEW} = 9.975 \times 10^{-3} \text{ m}$

$$a = 1.27 \times 10^{-2} \text{ m}$$

$$\sigma_{SU} = \frac{12079.76/2}{2 \left( \frac{1.27 \times 10^{-2}}{\cos 40} \right) 9.975 \times 10^{-3}} = 18.26 \text{ MPa}$$

For the system within 50% of the safety factor gives 27.4 MPa

### APPENDIX E-3: Hub Attachment

#### Part A: Failure by Bearing or Bushing on Plate

Mass of aluminum block added to Hub Attachment is 38 grams.

$$P_{U(Tension)} = (m + m_{add})r\omega^2 = (1 + 0.0176 + 0.0316 + 0.038)0.61(162.35^2) = 17503.73 \text{ N}$$

$$\sigma_{BR} = \frac{P_{U(Bearing)}}{Dt_{NEW}}$$

Where  $D = 1 \times 10^{-2} \text{ m}$

$$t_{NEW} = 1 \times 10^{-2} \text{ m}$$

$$\sigma_{BR} = \frac{17503.73/2}{1 \times 10^{-2}(1 \times 10^{-2})} = 87.51 \text{ MPa}$$

For the system within 50% of the safety factor gives 131.28 MPa

#### Part B: Failure in Tension

$$\sigma_U = \frac{P_{U(Tension)}}{(W - D)t_{NEW}}$$

Where  $W = 3.383 \times 10^{-2} \text{ m}$

$$D = 1 \times 10^{-2} \text{ m}$$

$$t_{NEW} = 1 \times 10^{-2} \text{ m}$$

$$\sigma_U = \frac{17503.73/2}{(3.383 \times 10^{-2} - 1 \times 10^{-2})1 \times 10^{-2}} = 36.73 \text{ MPa}$$

For the system within 50% of the safety factor gives 55.09 MPa

### Part C: Failure by Shear Tear Out

$$\sigma_{SU} = \frac{17503.73/2}{2 \frac{a}{\cos 40} t_{NEW}}$$

Where  $t_{NEW} = 1 \times 10^{-2}$  m

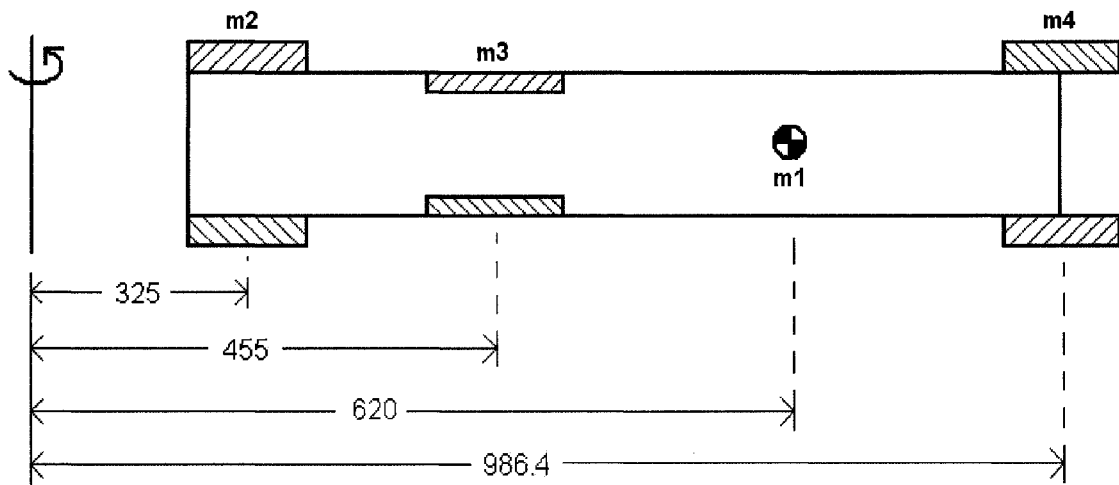
$$\sigma_{SU} = \frac{17503.73/2}{2 \left( \frac{1.5 \times 10^{-2}}{\cos 40} \right) 1 \times 10^{-2}} = 22.35 \text{ MPa}$$

For the system within 50% of the safety factor gives 33.52 MPa

Now the extra aluminum blocks are added to the system, failures in tension, shear tear out and bearing or bushing on plate are prevented.

## APPENDIX F

### Actively Controlled Tip Centrifugal Force for Whirl Tower Test at DLR



Units are in millimeters

$$m_1 = 1000 \text{ grams}$$

$$m_2 = 38 \text{ grams}$$

$$m_3 = 31.6 \text{ grams}$$

$$m_4 = 17.6 \text{ grams}$$

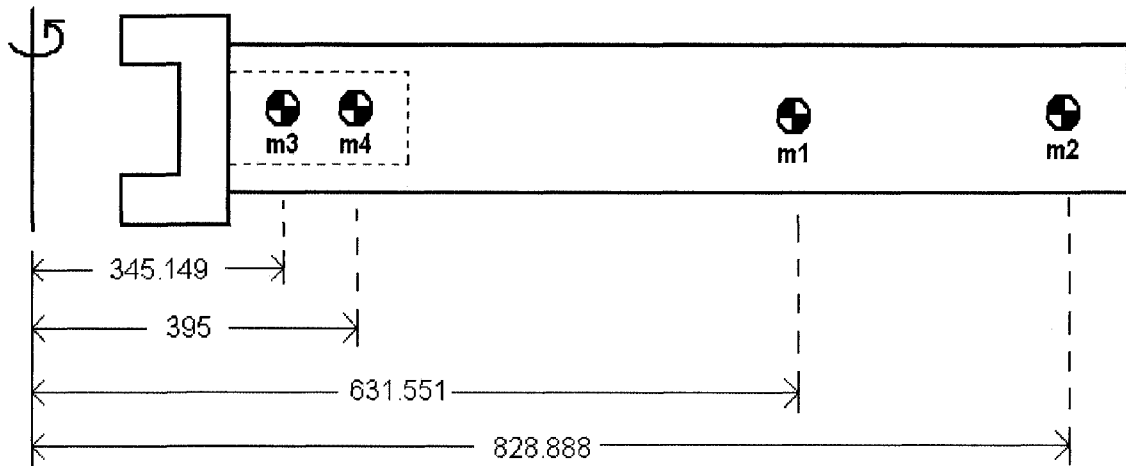
$$mass_{Total} R_{CG} = 1(0.62) + 0.038(0.325) + 0.0316(0.455) + 0.0176(0.9864)$$

$$R_{CG} = \frac{0.66408864}{1.0872} = 0.610824$$

$$F_{CG} = 1.0872(0.610824)162.35^2 = 17.504 \text{ kN}$$

## APPENDIX G

### Actively Controlled Flap Centrifugal Force for Whirl Tower Test at DLR



Units are in millimeters

$$m_1 = 688.13 \text{ grams}$$

$$m_2 = 105.454 \text{ grams}$$

$$m_3 = 522.64 \text{ grams}$$

$$m_4 = 111.923 \text{ grams}$$

$$mass_{Total} R_{CG} = 0.68813(0.631551) + 0.105454(0.828888) + 0.52264(0.345149) + 0.111923(0.395)$$

$$R_{CG} = \frac{0.746597}{1.428147} = 0.5227732$$

$$F_{CG} = 1.428147(0.5227732)162.35^2 = 19.678 \text{ kN}$$